MARINE PROPELLER BLADE TIP FLOWS

by

David Scott Greeley

B.S., Webb Institute of Naval Architecture
(1976)

SUBMITTED IN PARTIAL FULFILLMENT
OF THE REQUIREMENTS FOR THE
DEGREE OF

DOCTOR OF PHILOSOPHY

at the

MASSACHUSETTS INSTITUTE OF TECHNOLOGY

January 1982

© Massachusetts Institute of Technology, 1982

Signature of Author _____
Department of Ocean Engineering
January, 1982

Certified by _____
Thesis Supervisor

Accepted by _____
Chairman, Departmental Committee on Graduate Students

ARCHIVES
MASSACHUSETTS INSTITUTE
OF TECHNOLOGY
MAR 18 1982
LIBRARIES

MARINE PROPELLER BLADE TIP FLOWS

by

David Scott Greeley

Submitted to the Department of Ocean Engineering,
January, 1982, in partial fulfillment of the requirements
for the Degree of Doctor of Philosophy

ABSTRACT

A numerical lifting surface method is developed for the prediction of the steady, non-cavitating flow around the tips of marine propeller blades. An inviscid flow model is employed together with a local viscous analysis of the leading edge flow behavior, and the major effects of vorticity shed from swept leading edges are included.

The usual propeller analysis problem is solved using a vortex lattice approach, which includes an efficient method for calculating the correct geometry of the trailing vortex wake. The attached flow analysis is broken down into "global" and "local" problems to yield high resolution in the tip region without an undue penalty in computation time. A semi-empirical viscous analysis, based on airfoil and swept wing data, is used to determine the amount of vorticity shed into the fluid due to flow separation at the blade leading edge. A first-order representation of the leading edge vortex sheet is employed to solve the resulting boundary value problem.

Comparisons between computed results and available experimental data are generally quite good. The theory qualitatively explains the influence of skew on leading edge sheet cavitation inception, and also predicts a substantial Reynolds number effect. Data at higher Reynolds numbers are required to confirm the scale effects predicted by the current theory.

Thesis Supervisor: Justin E. Kerwin
Title: Professor of Naval Architecture

ACKNOWLEDGEMENTS

I would like to thank my thesis supervisor Professor Justin E. Kerwin for his constant encouragement during the course of this thesis. His physical insight and thorough knowledge of computational techniques were invaluable. The other members of the thesis committee - Professor Robert Van Houten, Professor Eugene Covert, Professor David Burke, and Dr. Neal Brown - also contributed their time and talent unselfishly. Special thanks to Professor Van Houten for always finding time for our numerous discussions.

Many thanks are extended to Dr. Sukeyuki Kobayashi and Mr. James Uhlman for their useful suggestions and willingness to discuss experimental results and theoretical procedures with the author.

The superb typing of the thesis manuscript was done by Miss Joanne M. Sullivan. Her cheerful support during periods of discouragement is greatly appreciated.

This work was begun while the author was a National Science Foundation Graduate Fellow. Subsequent support was provided by the David W. Taylor Naval Ship Research and Development Center and the Office of Naval Research.

TABLE OF CONTENTS

LIST OF FIGURES

NOMENCLATURE

A_{ij}	influence coefficient matrix, defined in Eq. 3.6.1
AR	planar wing aspect ratio, AR = $b/\bar{c}$
b	span of planar wing
c	blade section chord length
$\bar{c}$	mean chord of planar wing
$\underline{c}$	unit vector in chordwise direction
c_d	two dimensional drag coefficient, $c_d = \text{drag}/\frac{1}{2}\rho c U_\infty^2$
c_l	two dimensional lift coefficient, $c_l = \text{lift}/\frac{1}{2}\rho c U_\infty^2$
c_t	two dimensional leading edge thrust coefficient, defined in Eq. A.3.3
C	leading edge singularity parameter, defined in Eq. A.3.1
C_p	pressure coefficient, $C_p = (p-p_\infty)/\frac{1}{2}\rho U_\infty^2$
C_s	leading edge suction force coefficient, defined in Eq. 4.3.1
D	propeller diameter
f	blade camber function
f_0	maximum blade section camber at a given radius
$\underline{F}$	vector force on blade surface
F_s	suction force per unit length of leading edge, defined in Eq. A.1.5
J	advance coefficient. In this thesis, $J = J_A = J_s$
J_A	advance coefficient based on speed of advance, $J_A = V_A/nD$

J_s	advance coefficient based on ship speed, $J_s = V_s/nD$
K	number of propeller blades
$K_{\underline{F}}$	force coefficient for one blade, $K_{\underline{F}} = \underline{F}/\rho n^2 D^4$
$K_{\underline{M}}$	moment coefficient for one blade, $K_{\underline{M}} = \underline{M}/\rho n^2 D^5$
K_Q	torque coefficient, $K_Q = Q/\rho n^2 D^5$
K_r	relaminarisation parameter, defined in Eq. 4.2.3
K_T	thrust coefficient, $K_T = T/\rho n^2 D^4$
L	lift force
$\underline{m}$	unit vector along spanwise vortices
M	number of chordwise panels over radius
$\underline{M}$	vector moment on blade surface
n	propeller rotational speed, revolutions per unit time
$\underline{n}$	unit vector normal to blade camber surface
N	number of spanwise vortices within a chordwise strip
N_{uw}	number of discrete vortex segments in ultimate tip vortex
p	pressure
p_∞	ambient pressure
P	pressure gradient parameter, defined in Eq. C.2
P	propeller pitch
Q	strength of concentrated line source per unit length
Q	propeller torque
r	radial coordinate

r	leading edge radius
r_{cut}	inner radius of local tip solution, Fig. 3.9.1
r_H	hub radius
r_m	control point radii in tip solution, Eq. 3.9.2
r_n	leading edge radius of section in plane normal to leading edge
r_w	radius of ultimate tip vortices
r_{wH}	radius of hub vortex at end of transition wake
R	propeller radius
R_{le}	Reynolds number for leading edge flow, defined in Eq. 4.3.2
$R_{\theta_{al}}$	Reynolds number based on attachment line boundary layer momentum thickness, defined in Eq. 4.2.2
R_{θ_s}	Reynolds number based on boundary layer momentum thickness at separation, defined in Eq. C.4.1
s	fraction of chord from leading edge
s	distance along surface
$\underline{s}$	unit spanwise vector on blade
$\tilde{s}$	transformed chordwise coordinate, see Eq. 3.2.2
t	blade thickness function
t_0	maximum blade section thickness at a given radius
T	propeller thrust
u,v,w	perturbation velocities in x,y,z coordinate system
u_a, u_t	axial and tangential velocities induced by helical tip vortices

$u_a(x',r)$, $u_t(x',r)$ } axial and tangential induced velocities due to propeller and wake singularity system

$u_{a1}(r)$, $u_{t1}(r)$ } axial and tangential induced velocities just behind blade trailing edge

$u_{a2}(r)$, $u_{t2}(r)$ } axial and tangential induced velocities at end of transition wake

u_{tH} tangential velocity induced by ultimate hub vortex

U_n component of inflow velocity normal to leading edge; see Fig. 4.2.2 or 4.3.1

U_s component of inflow velocity parallel to leading edge; see Fig. 4.2.2 or 4.3.1

U_∞ free stream velocity

$\underline{V}$ total velocity vector

V_A volumetric mean inflow velocity,

$$V_A = \frac{2}{[1-(r_{H/R})^2]} \int_{r_{H/R}}^{1} V_A(r)\, r\, dr$$

V_C chordwise velocity at free vortex sheet node

V_R radial component of inflow velocity

V_S spanwise velocity at free vortex sheet node

V_S ship speed

V_T tangential component of inflow velocity

x	distance along chord for two dimensional foils
x'	axial distance downstream of blade trailing edge along a given streamline
x_{final}	distance downstream of blade trailing edge at which wake pitch stops changing
x_m	rake, x-coordinate of midchord line, positive in direction of positive x (see Fig. 3.1.2)
x_{tw}	axial extent of transition wake, measured from blade trailing edge
x,y,z	cartesian coordinate system fixed on propeller: x-positive downstream, y positive radially outward, and z being determined to complete the right handed system
x,y,z	cartesian coordinate system fixed on planar wing: x-positive downstream, y to starboard, and z up.
α	angle of attack
β	undisturbed flow angle
β_T	pitch angle of transition wake leaving blade tip
β_w	pitch angle of ultimate wake tip vortex helix
$\overline{\beta}$	pitch angle of tip vortex separated from leading edge in global solution; see Eq. 3.4.1
$\beta(x',r)$	pitch angle in transition wake
γ	strength of vortex sheet
γ_b	strength of bound vortex sheet
γ_s	strength of leading edge shed vortex sheet
Γ	strength of discrete vortex segment or horseshoe vortex
Γ_b	circulation around blade section (bound circulation)
Γ_c	strength of chordwise vortex in discretized free vortex sheet

Γ_s strength of spanwise vortex in discretized free vortex sheet

Γ_t strength of ultimate tip vortex

δ_c contraction angle of tip vortex; see Fig. 3.3.2

δ_k angular coordinate of k'th blade

$\delta\theta_{tw}$ angular extent of discrete vortex segment in transition wake

Δ maximum displacement of separated tip vortex in global solution

η open water propeller efficiency, $\eta = (J \cdot K_T)/(2\pi K_Q)$

θ angular coordinate in propeller fixed coordinates, $\theta = \tan^{-1}(z/y)$

θ transformed chordwise coordinate; see Eq. A.2.1

θ_{al} attachment line boundary layer momentum thickness, defined in Eq. 4.2.1

θ_m skew angle: angular coordinate of mid-chord line as measured from y-axis, positive clockwise when looking toward positive x-axis (See Fig. 3.1.1)

θ_s momemtum thickness of boundary layer at separation; see Eq. C.4.1

Λ leading edge sweep angle; see Fig. 4.3.1

ν kinematic viscosity of fluid

ξ,η,ζ coordinate system for sheared wing: see Fig. 4.3.1 and Fig. E.1

ξ x'/x_{final}

ρ mass density of fluid

ρ_m radial coordinate of chordwise vortices, defined in Eq. 3.2.1 and Eq. 3.9.1

σ_n chordwise position of concentrated vortex, defined in Eq. 3.2.2

ϕ nose-tail pitch angle of propeller blade section

ω propeller rotational speed, radians per unit time

$\underline{\omega}$ vorticity vector

SUPERSCRIPTS

I inflow velocity, see Eq. 3.6.2

q source

SUBSCRIPTS

c camber surface

l,t leading and trailing edges

m midchord

m spanwise index

n normal section

n chordwise index

w ultimate wake

I. Introduction

The hydrodynamic analysis of marine propellers has progressed greatly since the introduction of the digital computer approximately twenty years ago. It is now possible to predict the steady performance characteristics of most propellers with engineering accuracy, and to calculate unsteady loads acting on propeller blades when the propeller is operating in a spatially non-uniform inflow. It is also possible to predict the behavior of unsteady sheet cavitation on propellers operating in a wakefield, as shown by Lee (1979).

Yet despite the tremendous amount of progress made in the prediction of the unsteady performance of marine propellers, both cavitating and non-cavitating, the steady flow analysis problem is still far from being completely solved. Designs incorporating significant amounts of skew, rake, and radial pitch variation not infrequently fail to meet the desired thrust, power, and RPM relationships in both model- and full-scale. And as more ships, both civilian and military, come to rely on underwater acoustic sensors to fulfill their mission, the accurate prediction of cavitation inception on their propellers becomes very important since a cavitating propeller is invariably the loudest underwater noise source on a ship. Model tests are no panacea because of the large Reynolds number ("scale") effects on propeller cavitation, even in steady flow. Many techniques for delaying cavitation inception may lead to a reduction in propeller efficiency, so that a real need exists for the

analytical and computational tools to allow the propeller designer to make a rational choice of propeller characteristics based on both efficiency and cavitation criteria.

The ultimate objectives of the research described herein are two-fold: the accurate prediction of both steady and unsteady loadings on arbitrary propeller blades operating in a specified inflow; and the prediction of cavitation inception in both steady and unsteady flow, over a range of Reynolds numbers encompassing both model- and full-scale propellers.

The goals of the current thesis are more modest, but form a necessary first step toward the ultimate objectives described above. They are:

i) Correctly model the main features of the flow near the tip of a propeller blade over a range of advance coefficients in steady, non-cavitating flow. In particular, the form and location of the tip vortex will be of major concern.

ii) Improve the prediction of blade loading in the tip region.

iii) Explain both qualitatively and quantitatively the observed effects of skew and Reynolds number on the inception of leading edge sheet cavitation.

No attempt is made here to predict the occurrence of tip vortex cavitation, since recent data (Arndt, 1981) suggest that boundary layer characteristics on both sides of the blade may influence tip vortex cavitation, and theoretical solutions for propeller blade boundary layers are not yet routinely available.

The basic approach utilized in this thesis is to decompose the tip flow prediction problem into a series of simpler problems, and solve these new, simpler problems successively. The primary reason for doing this is economic: the numerical calculations are far less expensive when done this way. In addition, it is easier to think about the flow prediction problem when it is broken down into its component parts.

There are four major sections in the tip flow analysis scheme described in this thesis:

a) A "global" solution, which consists of solving for the flow around the propeller as a whole, assuming attached flow on the blades. The results of this solution yield the overall forces and moments acting on the propeller blades.

b) A "local" tip flow solution, which gives a very detailed prediction of the loads on the tip of the key blade under the assumption of normal attached flow (trailing vorticity leaving blade trailing edge and tip edge only).

c) A local viscous analysis of the flow near the leading edge of the blade tip.

d) A local tip flow solution which allows for the possibility of a leading edge or part-span vortex separating from the leading edge and passing over the blade tip, profoundly altering the load distribution in the tip region.

Although there would appear to be strong interactions between these four segments of the tip flow analysis problem that would require a tremendous amount of iteration, it is shown that useful predictions of tip flow

behavior can be obtained without iteration. This helps keep the cost of the calculations described herein within reason, so that the theory can be used regularly as a design tool.

II. Formulation of the Problem

2.1 Fundamental Assumptions

The propeller is assumed to consist of K identical blades symmetrically arranged about a common axis. The blades rotate about the axis at a constant angular velocity ω in an unbounded, incompressible fluid. The presence of the hub is ignored. The inflow velocities to the propeller may vary with radius only, so that the flow seen in a propeller-fixed coordinate system is steady in time.

The blades are assumed to be thin and operate a small angle of attack, so that they may be modelled as source and vortex sheets on the mean camber surface of the blade (the separated flow tip solution requires special treatment, discussed in Chapter V). The trailing wakes leaving the blades are also assumed to be thin, so that they may be represented by vortex sheets. The perturbation velocity due to the presence of the propeller is considered irrotational outside the blade boundary layers and the trailing vortex wake.

The presence of boundary layers on the blade surface is not explicitly taken into account in the current work. Slight empirical corrections are made to account for the loss of lift caused by boundary layers altering the "effective" shape of the blade.

2.2 Boundary Value Problem

The solution to the propeller steady flow problem must satisfy the principle of mass conservation everywhere. The following boundary

conditions are imposed to make the solution unique:

a) The flow must be tangent to the blade surface. In a blade fixed coordinate system, this is expressed as $\underline{V} \cdot \underline{n} = 0$ on the blade, where $\underline{V}$ is the total fluid velocity and $\underline{n}$ is the local normal vector

b) The flow must leave the blade trailing edge tangentially (Kutta condition)

c) Circulation is conserved (Kelvin's theorem)

d) The trailing vortex sheets must be force-free (no pressure jump across wake).

e) The perturbation velocity due to the propeller must vanish sufficiently far upstream of the propeller.

2.3 Singularity Distributions

The steady flow problem is solved by distributing sources and vortices on the blade camber surface and vortices on the trailing wake and finding the correct strengths of the singularities by imposing the above boundary conditions, which leads to a surface integral equation. This technique is ideally suited to numerical computation since integral equations can be readily approximated by a system of linear algebraic equations.

The source distribution is used to represent the jump in normal velocity at the camber surface due to the blade thickness. The strength of these sources are computed from the stripwise application of thin wing theory at each radius.

The vortex distribution is employed to represent the jump in tangential velocity across the camber surface and across the trailing vortex sheets. Since the vortex strength is a vector lying in the blade camber surface, it is convenient to resolve it into a spanwise and a chordwise component at each point. The determination of the vortex strength everywhere so that the boundary conditions are met requires the solution of an integral equation on the blade camber surface. In the present work the vortex sheets are discretized and the integral equation is solved at a limited number of control points on the blade camber surface.

III. Formulation of Numerical Lifting Surface Theory

3.1 Blade Geometry

The propeller geometry problem consists of finding the cartesian coordinates of points on the camber surface of the blade, given the usual propeller geometric descriptions.

The geometry is specified with respect to a right-handed, blade-fixed coordinate system, with the x-axis pointing downstream and the y-axis at some arbitrary angular orientation relative to the key blade. Cylindrical coordinates (x, r, θ) are defined as usual, with

$$r = \sqrt{y^2 + z^2} \tag{3.1.1}$$

and θ being measured clockwise from the y-axis when viewed looking downstream.

The skew angle $\theta_m(r)$ is defined as the angular position of the section midchord at radius r. $\theta_m(r)$ may contain an arbitrary additive constant, due to a non-unique specification of the position of the y-axis. A projected view of a blade looking downstream is shown in Fig. 3.1.1.

The x coordinate of the section midchord (Fig. 3.1.2) is defined by the rake, $x_m(r)$, which may also contain an arbitrary additive constant.

The leading and trailing edges of the blade are found by passing a helix of pitch angle $\phi(r)$ through the midchord point at each radius r. The length of the blade chord along this helix is c(r), and we get from simple geometry:

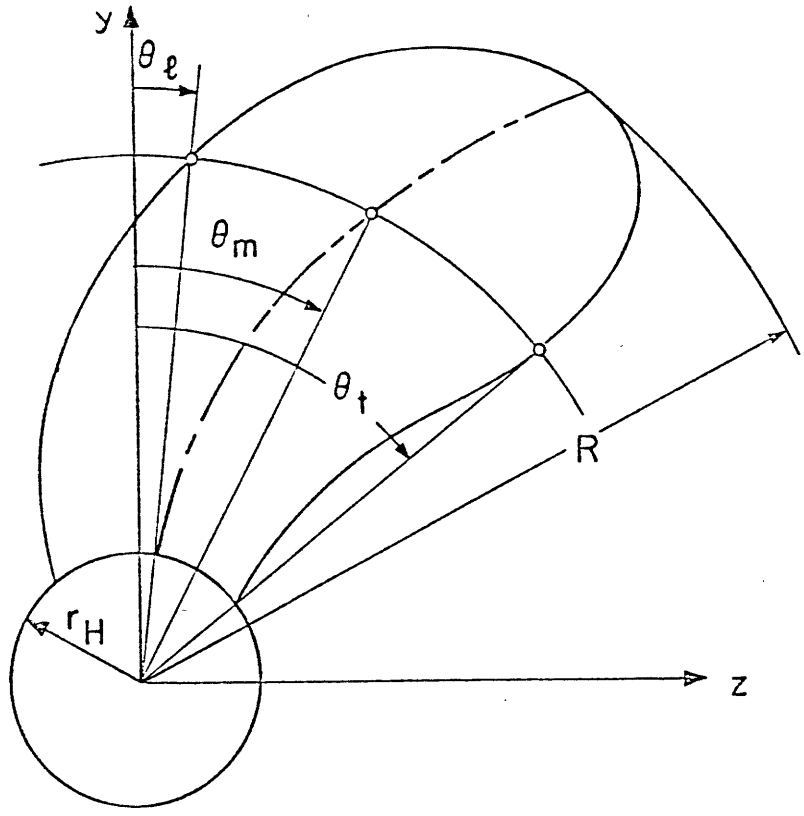

Figure 3.1.1 - Projected view of blade looking downstream

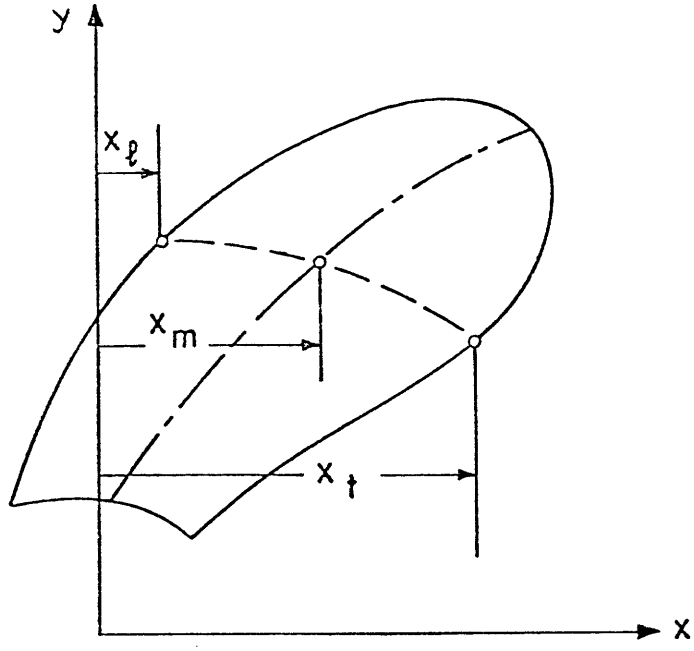

Figure 3.1.2 - Longitudinal elevation of propeller blade looking to starboard

$$x_{\ell,t} = x_m \mp \frac{c}{2} \sin \phi$$

$$\theta_{\ell,t} = \theta_m \mp \frac{c}{2r} \cos \phi$$

$$y_{\ell,t} = r \cos \theta_{\ell,t}$$

$$z_{\ell,t} = r \sin \theta_{\ell,t} \qquad (3.1.2)$$

where the subscripts ℓ, t refer to the blade leading and trailing edges.

A non-dimensional chordwise variable s is defined such that s=0 at the blade leading edge and s=1 at the trailing edge, s being measured along the pitch helix. The cylindrical blade section camber and thickness are specified as a function of s; f(s) and t(s) respectively. (see Fig. 3.1.3).

To identify blades other than the key blade, a blade indexing angle is defined,

$$\delta_k = \frac{2\pi(k-1)}{K} \quad , \quad k = 1, 2, \ldots K) \qquad (3.1.3)$$

where k is the identifying index and K is the number of propeller blades.

The coordinates of a point on the camber surface of the k'th blade may now be specified in terms of the usual propeller geometric quantities (skew, rake, pitch, chord, and camber):

$$x_c = x_m + c(s - \tfrac{1}{2}) \sin \phi - f \cos \phi$$

$$\theta_c = \theta_m + c(s - \tfrac{1}{2}) \frac{\cos \phi}{r} + f \frac{\sin \phi}{r} + \delta_k \qquad (3.1.4)$$

$$y_c = r \cos \theta_c$$

$$z_c = r \sin \theta_c$$

where the subscript c denotes blade camber surface.

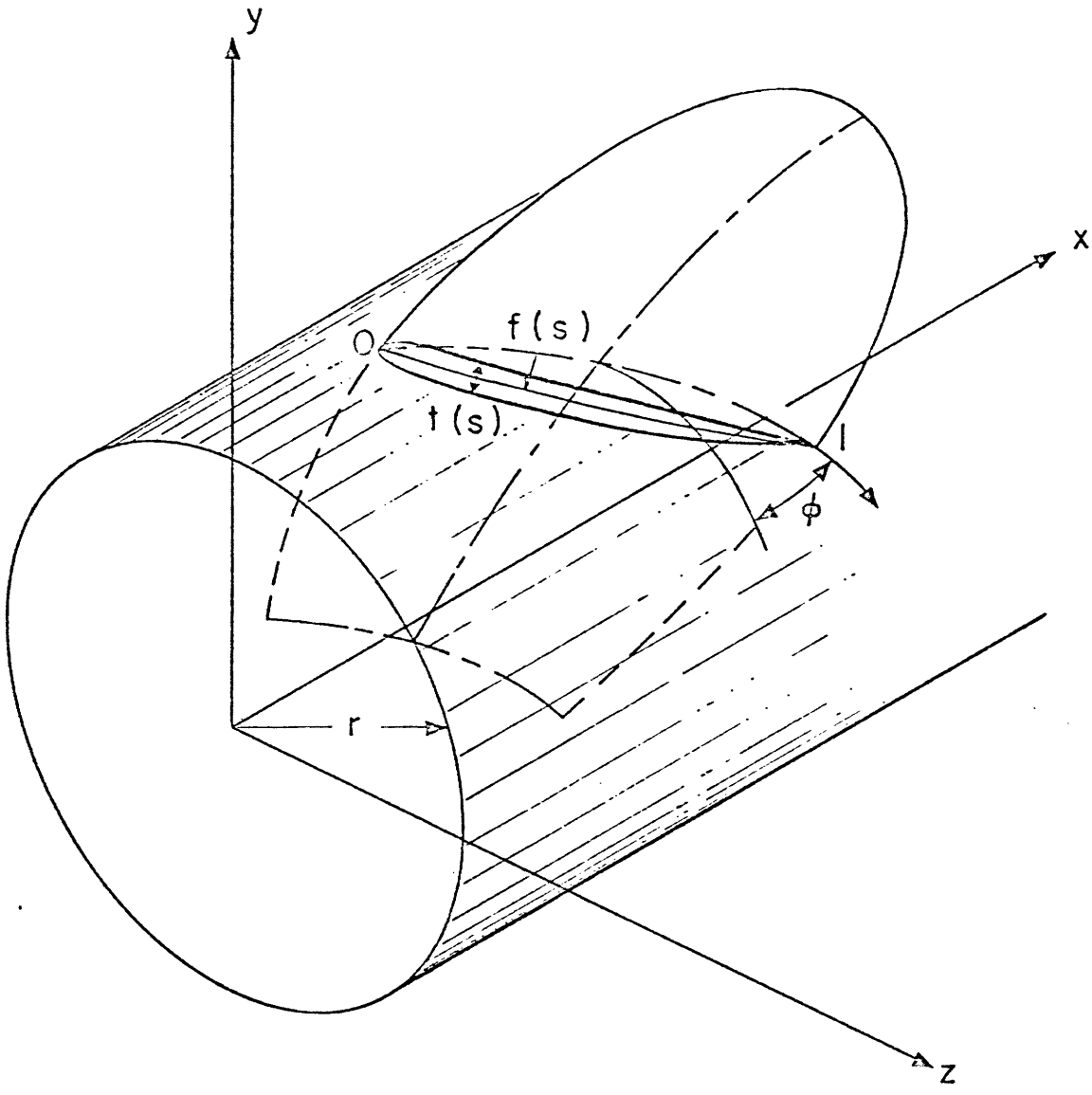

Figure 3.1.3 - Cylindrical section of blade

3.2 Discretization of Blade Singularity Distribution

The continuous distribution of sources and vortices used to represent blade thickness and loading is replaced by a lattice of concentrated straight line elements. The elements are of constant strength, and the endpoints of each elements are located on the blade camber surface. The velocities induced at any point in space by these concentrated singularities may be easily computed from formulas given by Kerwin and Lee (1978).

The element arrangement used in the present work is shown in Fig. 3.2.1. The radial interval from the hub r_H to the tip R is divided into M equal intervals, with the extremities of the lattice inset one quarter interval from the ends of the blade. The endpoints of the discrete vortices located at radii

$$\rho_m = \frac{(R - r_H)(4m-3)}{4M + 2} \quad , \quad m = 1, 2, \ldots, M + 1 \qquad (3.2.1)$$

Kerwin and Lee (1978) discussed several chordwise distributions of singularities and concluded that a uniform chordwise distribution of singularities, with an explicit Kutta condition, was the best compromise for solving both the steady and unsteady problems with the same spacing. But since this thesis deals only with steady flow, this choice was re-examined. For the current work a "cosine" chordwise spacing of singularities is chosen, in which the vortices and control points are located at equal intervals of $\tilde{s}$, where the chordwise variable s is given by

$$s = \frac{1}{2}(1 - \cos \tilde{s}) \quad , \quad (0 \leq \tilde{s} \leq \pi) \qquad (3.2.2)$$

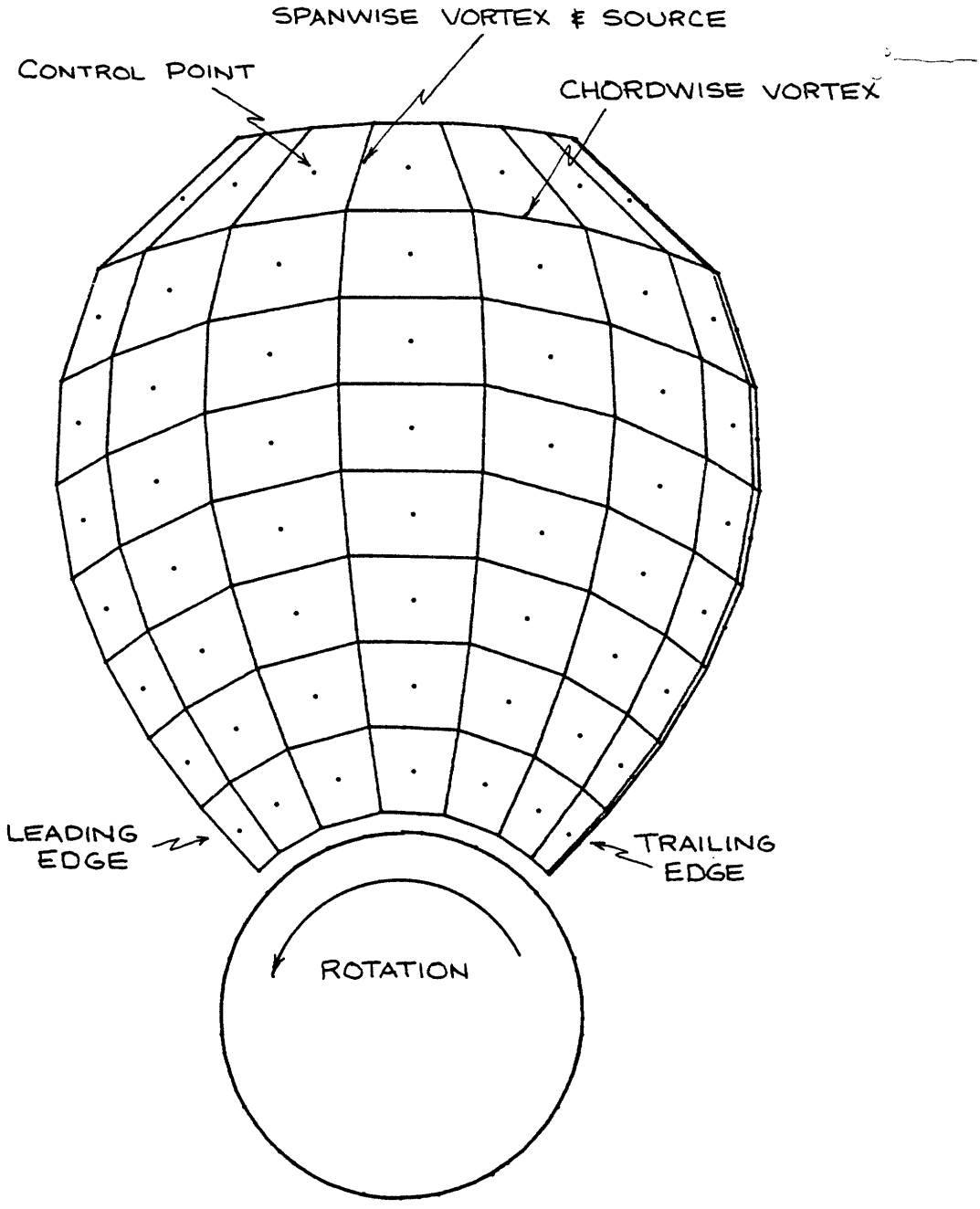

Figure 3.2.1 - Discretization of blade singularities

If there are N vortices over the chord, the positions of the vortices, σ_n, and control points, s_i, are given by

$$\sigma_n = \frac{1}{2}\left\{1 - \cos\left[\frac{(n-\frac{1}{2})\pi}{N}\right]\right\}, \quad n = 1, 2, \ldots, N.$$

$$s_i = \frac{1}{2}\left\{1 - \cos\left[\frac{i\pi}{N}\right]\right\}, \qquad i = 1, 2, \ldots, N. \tag{3.2.3}$$

Note that with this arrangement last control point is at the trailing edge, and two dimensional calculations show that this forces the distribution of vorticity over the chord to have the proper behavior near the trailing edge (implicit Kutta condition). This chordwise singularity distribution is also useful in that it enables the magnitude of the leading edge singularity (leading edge suction force) to be readily calculated (See Appendix A).

The sensitivity of the computed global solution to the parameters M and N is shown in Chapter VI.

3.3 Geometry of Trailing Vortex Wake

The geometry of the trailing vortex wake greatly influences the calculation of induced velocities on the blade, and hence the calculation of blade loading. The current wake model was originally developed by Kerwin (1981) and is extended in the present work.

The propeller wake is divided into two parts (Fig. 3.3.1):

a) A transition wake region where the contraction and deformation of the slipstream occurs, and

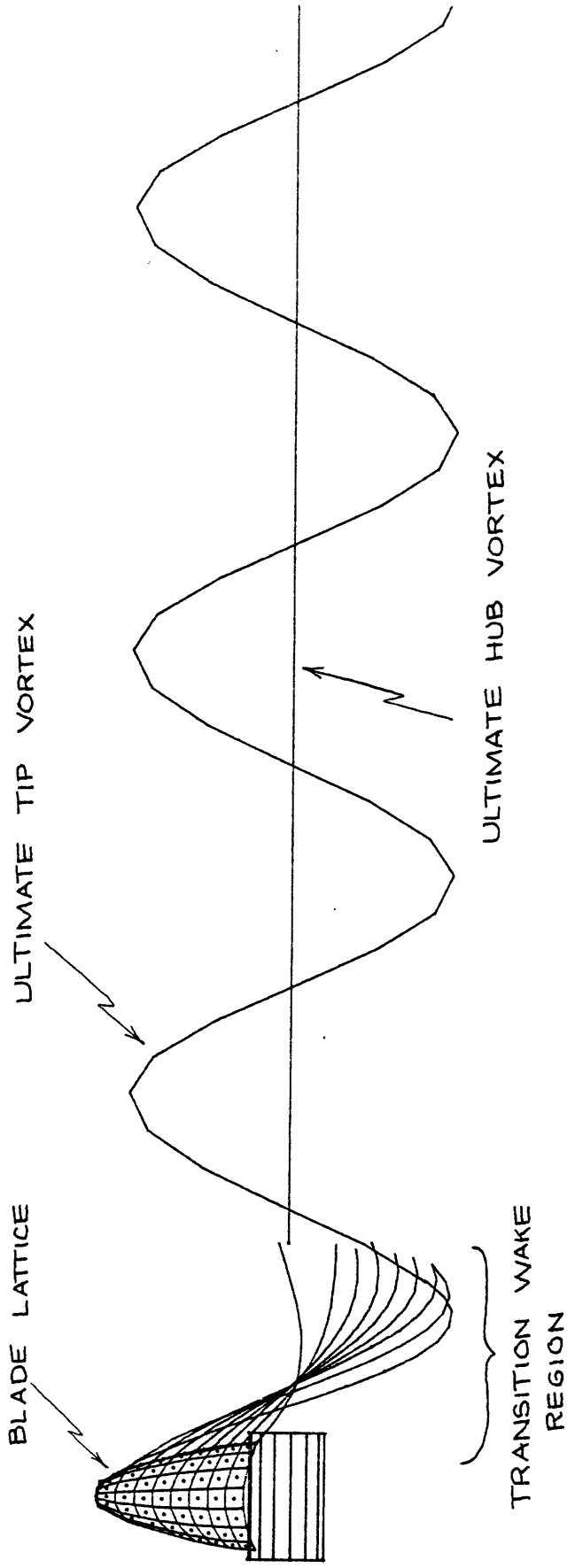

Figure 3.3.1 - Trailing vortex wake model

b) An ultimate wake region which is composed of K concentrated helical tip vortices and a single rolled up hub vortex.

Although an earlier wake model (Kerwin and Lee, 1978) included a strong rolling-up in the transition wake region, laser velocimeter measurements in the M.I.T. propeller tunnel indicate that the trailing vortex wake does not roll-up completely, so that the current transition wake model is probably more realistic.

The radii of the discrete vortices representing the trailing wake are determined by a limited set of parameters, chosen in accordance with experimental data. (Fig. 3.3.2):

a) The radius of the rolled up tip vortices, r_w

b) The radius of the hub vortex at the end of the transition wake, r_{wH}

c) The length of the transition wake region, x_{tw}

d) The contraction angle of the tip vortex as it leaves the blade tip, δ_c

The trailers comprising the transition wake region are extensions of the chordwise vortices on the blade. The radii of the innermost and outermost trailers in the transition wake region are set by smooth curves consistent with the above wake descriptors, and the radii of intermediate trailers are obtained by interpolation at any downstream location.

Since the trailing vortex wake is modeled by a series of short, straight vortex segments, it is also necessary to specify the angular extent subtended by each vortex segment. In the transition wake the

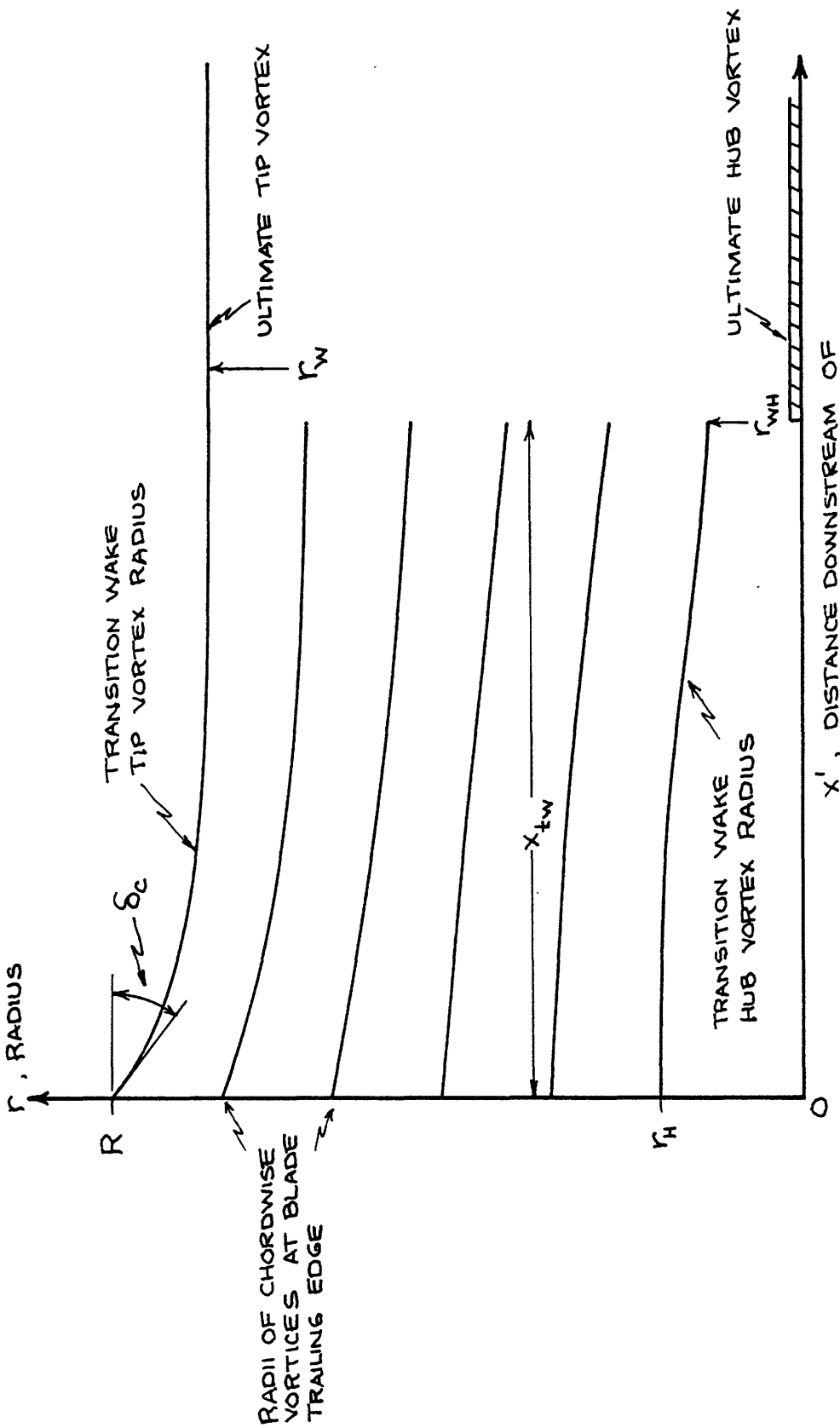

Figure 3.3.2 - Radii of trailing vortices

angular subdivision is specified by the parameter $\delta\theta_{tw}$. The ultimate wake tip vortex from each blade is composed of three complete turns of a helix, and the angular extent of each straight vortex element is determined by specifying the number of points in the ultimate tip vortex, N_{uw}. These two parameters are set by considering the trade-off between accuracy and computational cost.

Kerwin and Lee (1978) demonstrated that the wake pitch is the most critical parameter in determining the wake geometry, since this sets the distance between the key blade and the wake of the blade immediately ahead of it. Because this is such a crucial parameter, it was decided to calculate the correct wake pitch, rather than providing it as input data.

The pitch of the ultimate tip vortices is calculated first, using the theory of Loukakis (1971). Using an estimated strength of the ultimate tip vortex (obtained by solving the boundary value problem with an approximate wake geometry) and an estimated tip vortex core radius size, the pitch of the ultimate tip vortex may be calculated as shown in Appendix B. This calculation also yields the axial and tangential induced velocities at the ultimate tip vortex.

The pitch of the transition wake is allowed to vary in both the radial and downstream directions. The correct pitch is that which results in the wake being force-free, i.e., no pressure jump across the trailing vortex wake. For the steady flow case considered here, this condition is met if the total velocity vector is parallel to the local

vorticity vector everywhere on the trailing vortex sheet. Since the laser velocimeter measurements of Min (1978) indicate that the wake pitch varies smoothly in the downstream direction, it appears reasonable to calculate the correct wake pitch at a limited number of points in the transition wake and assume a smooth variation in pitch between these points. In the present work the correct pitch is calculated at a series of points just downstream of the blade trailing edge and at another series of points at $x' = 0.70\ x_{tw}$. The pitch everywhere else in the transition wake is obtained by interpolation, and a new wake geometry is generated. Since the geometry of the wake affects the calculation of the correct pitch, this wake alignment procedure requires an iterative solution: for a given wake geometry the correct pitch is calculated at several points in the wake, the wake geometry is updated to reflect the new calculated pitch distribution, and the process is repeated until the wake geometry stops changing.

All of the calculations described above require knowing the vorticity distribution on the blade and in the wake, which are the unknowns to be determined. It is therefore necessary to iterate not only on the wake geometry, but also on the vorticity distribution used to calculate the correct wake geometry. The following approach is used:

a) Solve the global boundary value problem and determine the vorticity distribution using an assumed trailing vortex wake geometry.

b) Using the vorticity distribution from a), calculate the correct (force-free) wake geometry.

c) Re-solve the boundary value problem using the updated wake geometry and determine a new vorticity distribution. Continue iterating on steps a) and b) until the vorticity distribution stops changing.

The above process converges quite rapidly. The details of the wake alignment scheme are developed in Appendix B, and some results are presented in Chapter VI.

3.4 Vortex Sheet Separation from Blade Tip

Flow visualization experiments on low aspect ratio wings and propeller blades at high loadings show that the tip vortex does not leave the trailing edge, but rather separates along the tip chord or even from the leading edge. The "tip" vortex then passes above the wing or propeller blade, drastically changing the load distribution in the tip region and increasing the lift. A detailed discussion of this phenomenon and the approach used to model it are presented in Chapters IV and V of this thesis as part of the local tip flow analysis. Of interest here is how to go about adequately modeling this effect in the global flow analysis. Following Kerwin and Lee (1978) the chordwise vortices at the tip are allowed to separate from the blade and coalesce at a point above the trailing edge of the blade at the tip, as shown in Fig. 3.4.1. The pitch angle of the vortex leaving the leading edge of the

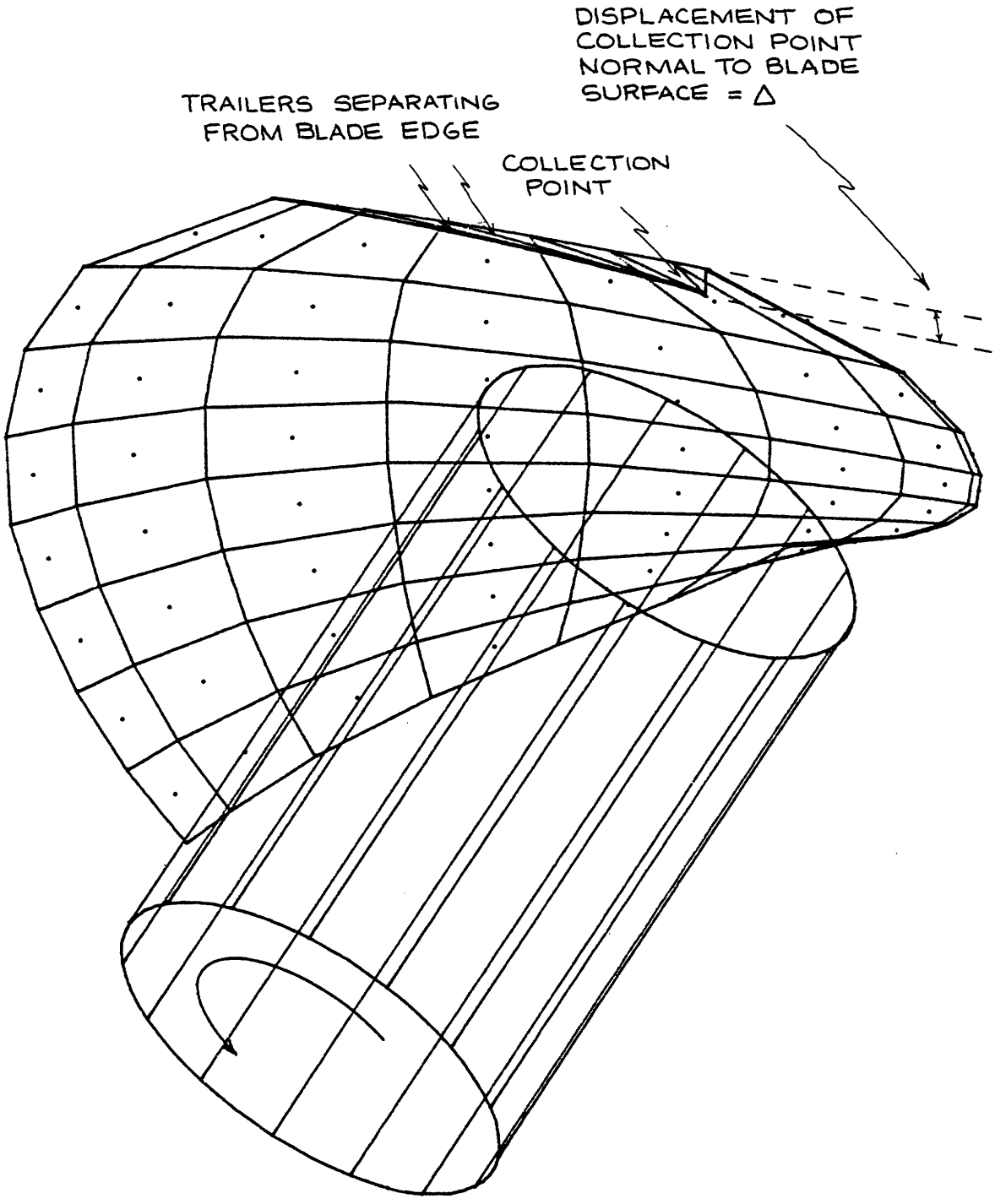

Figure 3.4.1 - Model of separation from
blade tip (global solution)

tip panel is assumed to be

$$\overline{\beta} = \frac{1}{2} (\beta + \beta_T) \qquad (3.4.1)$$

where β is the undisturbed inflow angle at the tip and β_T is the pitch of the transition wake tip vortex as it leaves the blade. The displacement of the trailers above the camber surface at the trailing edge is given by

$$\Delta = c \tan (\phi - \overline{\beta})$$

where c is the chord length of the tip panel, and ϕ is the pitch of the blade at the tip.

The displacement Δ is small when a propeller is operating near its design advance coefficient, but increases as J is reduced. This representation is sufficient to enable the thrust and torque of the propeller to be accurately calculated over a wide range of advance ratios. The more refined modeling of the separated tip vortex presented in Chapter V is necessary to predict the load distribution in the tip region.

3.5 Modeling of Other Blades and Wakes

It is not necessary to model the other blades and their transition wakes as accurately as the key blade because of the large distance between the other blade singularities and the key blade control points. A much coarser vortex-source lattice may be used to represent the other blades and wakes without impairing the accuracy of the final solution to the boundary value problem. The only exception to this rule is the transition wake from the blade just ahead of the key blade, which passes very close

to the key blade at low advance coefficients. This transition wake should be modeled in as much detail as the wake leaving the key blade. The present computer program allows for a wide variety of paneling schemes, a typical example being shown in Fig. 3.5.1.

3.6 Solution of Boundary Value Problem

The solution of the boundary value problem consists of determining the strengths of the singularities representing the propeller blades and their trailing vortex wakes, subject to the boundary conditions listed in Section 2.2. The strengths of the sources representing the blade thickness are determined by a stripwise application of thin wing theory at each radius, leaving only the vortex strengths to be determined.

The strengths of all the vortices on the blades and in the trailing vortex wake may be specified in terms of the strengths of the spanwise vortices on the key blade by applying Kelvin's theorem repeatedly. Since there are (NxM) spanwise vortices on the key blade and the same number of control points, we may formulate a set of linear simultaneous algebraic equations in order to determine the strengths of the spanwise vortices on the key blade, Γ_i.

The boundary condition to be applied is that of zero normal velocity at the control points on the key blade. Define an influence function A_{ij}, which is the normal velocity at the i'th control point caused by vortex system associated with a unit strength of j'th spanwise vortex. Then

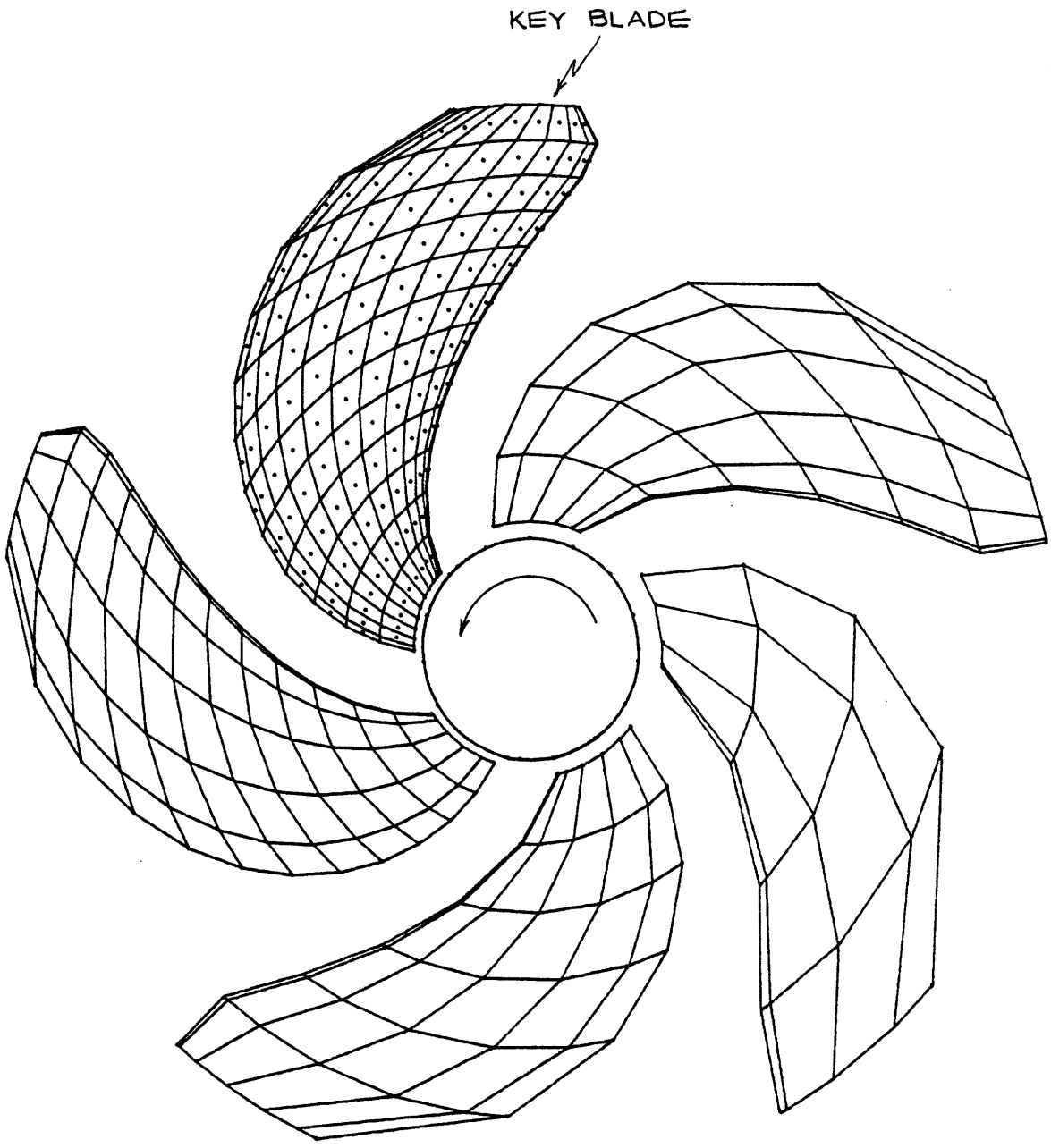

Figure 3.5.1 - Discretization of other blades

the total normal velocity at the i'th control point due to the vortex system on the blades and in the wake is given by

$$\sum_{j=1}^{(N\times M)} A_{ij}\,\Gamma_j \quad , \quad i = 1, 2, \ldots, (N\times M) \tag{3.6.1}$$

The normal component of the inflow velocity due to speed of advance and propeller rotation is given by

$$\underline{n}_i \cdot \underline{V}_i^{\,I} \tag{3.6.2}$$

where $\underline{n}_i$ is the unit normal vector.

The normal component of the velocity due to all of the sources is denoted

$$\underline{n}_i \cdot \underline{V}_i^{\,q} \tag{3.6.3}$$

Then the boundary condition can be written as

$$\sum_{j=1}^{(N\times M)} A_{ij}\,\Gamma_j + \underline{n}_i \cdot (\underline{V}_i^{\,I} + \underline{V}_i^{\,q}) = 0$$

or (3.6.4)

$$\sum_{j=1}^{(N\times M)} A_{ij}\,\Gamma_j = -\underline{n}_i \cdot (\underline{V}_i^{\,I} + \underline{V}_i^{\,q}) \quad , \; i = 1, 2, \ldots, (N\times M)$$

which is sufficient to determine the unknown Γ_j values.

3.7 Determination of Blade Forces

Following Kerwin and Lee (1978), the blade forces are computed by determining the forces acting on the line singularities representing the key blade. Assuming that the average velocity over the length of a

singularity can be approximated by the velocity at its midpoint, the force on the j'th key blade singularity can be expressed as

$$\underline{F}_j = \rho \, \Delta\ell_j [\underline{V}_j \times \underline{\Gamma}_j - \underline{V}_j \, Q_j] \tag{3.7.1}$$

where $\Delta\ell_j$ is the length of the line singularity, $\underline{V}_j$ is the total velocity at its midpoint, and Q_j is the strength per unit length of the line source. This computation is made for all of the spanwise and chordwise singularities on the key blade, except for the outermost chordwise vortices on the tip panel, which are assumed to be separated from the blade. (See Section 3.4).

The effect of viscous drag is modeled as a force increment on each of the spanwise singularities. The computed leading edge suction force is multiplied by a suction efficiency factor of 1/3 to simulate the experimentally observed loss of leading edge suction away from ideal angle of attack, as described by Kerwin and Lee (1978).

3.8 Formulation of Local Problem

The lifting surface theory just described is adequate to determine the overall forces on propeller blades with sufficient accuracy for many purposes. Determining the load distribution on the blade with high resolution requires a much finer discretization of the blade singularity system, with a large increase in computer time. Since the details of the load distribution near the tip are of primary interest in the current work, it makes sense to only use a fine source-and vortex-lattice in the tip region. The computational scheme used to do this is illustrated in

Fig. 3.8.1. There are four basic steps:

a) Solve the "global" boundary value problem for the entire propeller using a relatively coarse discretization of the blade singularity system.

b) Choose a "local" flow domain, including the tip region of the key blade and a portion of the key blade trailing vortex wake near the tip. Set the strengths of the sources and vortices in this local flow domain equal to zero.

c) At a series of points in the local flow domain, calculate the induced velocities caused by the remainder of the singularity system (i.e., the rest of the key blade, the rest of the key blade wake, and the other blades and wakes). Since there are no singularities in this region, the induced velocity is a smooth function of position, and interpolation may be used to find the induced velocity at any point in the local flow domain.

d) The local tip flow problem now consists of solving for the flow about the tip of the key blade only. The inflow velocity, $\underline{V}^I$, at each point on the blade tip now consists of the inflow velocity caused by the speed of advance and propeller rotation <u>plus</u> the induced velocities calculated in c). Note that the influence of most of the key blade trailing vortex wake is included in the induced velocity calculation, so that only the portion of the trailing

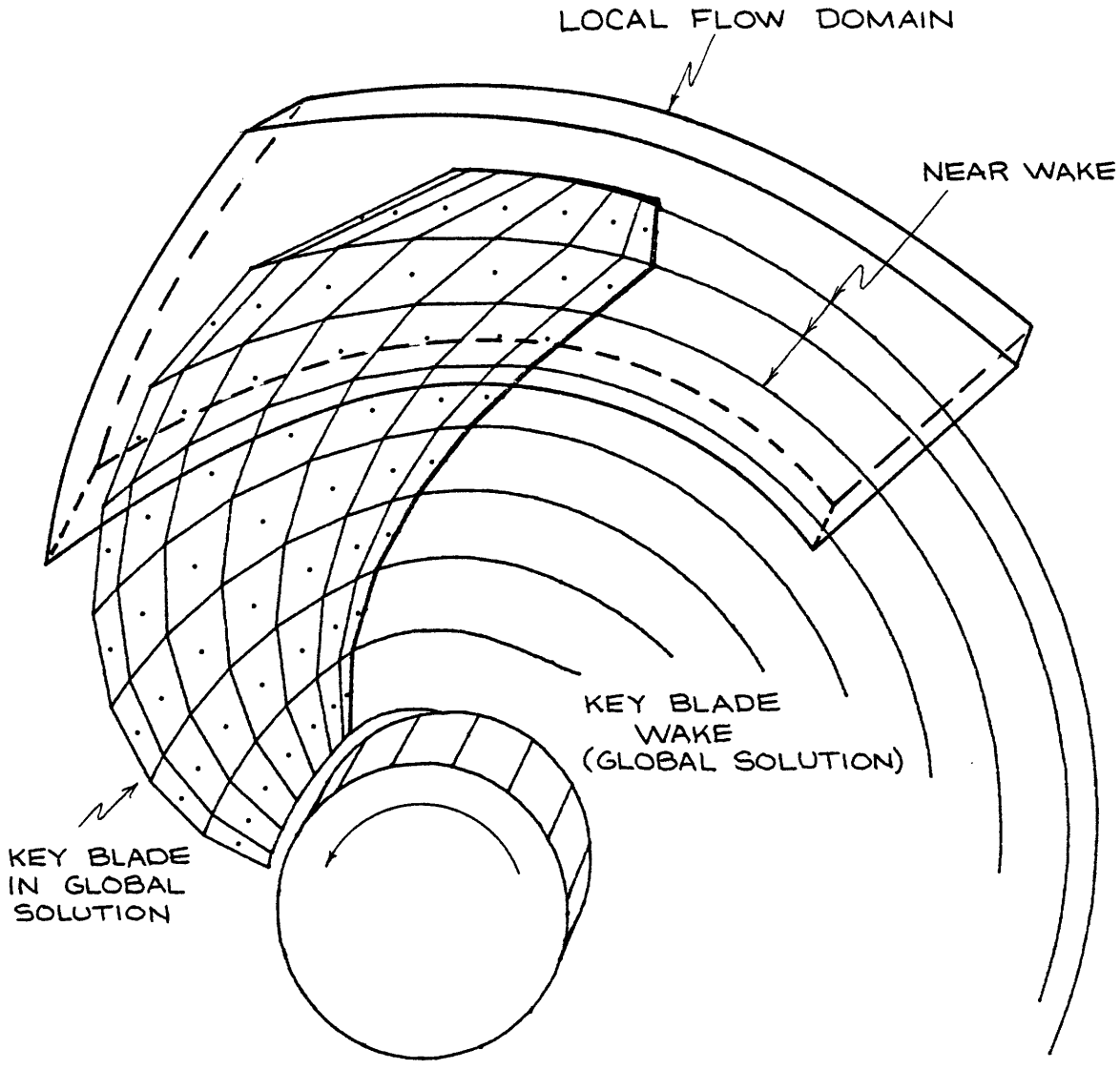

Figure 3.8.1 - Separation of problem into global and local domains

vortex wake in the local flow domain needs to be included.

From this point on we need only consider the problem of determining the flow around this isolated blade tip. No further account need be taken of the rest of the key blade and its trailing vortex wake, or of the other blades and their wakes. This results in a significant saving in computer time compared to calculating the details of the tip flow as part of the global solution.

A high resolution attached flow tip solution, using the same assumptions used in the global solution, is discussed below. This is used to provide input data for the viscous leading edge solution described in Chapter IV. Finally, the tip flow solution is re-solved in Chapter V, now allowing for the possibility of significant flow separation from the leading edge.

3.9 Calculation of Attached Flow Tip Solution

The method of calculating the attached flow tip solution is virtually identical to that used for the global solution, so that only those features peculiar to the tip solution will be discussed here.

In order to reasonably discretize a propeller blade with zero tip chord (planform having rounded tip in projected view) it was found necessary to divide the blade tip radially using "half-cosine" spacing instead of the uniform spacing used in the global solution. Dividing the tip region into M spanwise panels, the endpoints of the discrete

vortices are located at radii

$$\rho_m = r_{cut} + (1-r_{cut}) \sin\left[\frac{(m-1)\pi}{2M+1}\right], \qquad (3.9.1)$$

$$m = 1, 2, \ldots, M+1$$

and the control points are located at radii

$$r_m = r_{cut} + (1-r_{cut}) \sin\left[\frac{(m-1/2)\pi}{2M+1}\right] \qquad (3.9.2)$$

$$m = 1, 2, \ldots, M$$

where r_{cut} is the separation radius between global and local solutions.

The trailing vortex wake geometry for the attached flow tip solution is assumed to be the same as that used for the global solution. The approach developed in Section 3.4 for approximating the effect of flow separation from the tip is also utilized. Figs. 3.9.1 and 3.9.2 illustrates the vortex lattice grids typically used for global and local analyses.

An important part of the local tip solution is the determination of the loading near the leading edge, which is needed for the viscous leading edge analysis. Since thin airfoil theory (singularities on camberline instead of airfoil surface) is being used, the relevant descriptor of the leading edge flow is the magnitude of the leading edge suction force. This may be determined from the solution to the local tip flow boundary value problem by placing control points along the leading edge and computing the total upwash (normalwash) there, as shown in Appendix A. While there are other ways to determine the

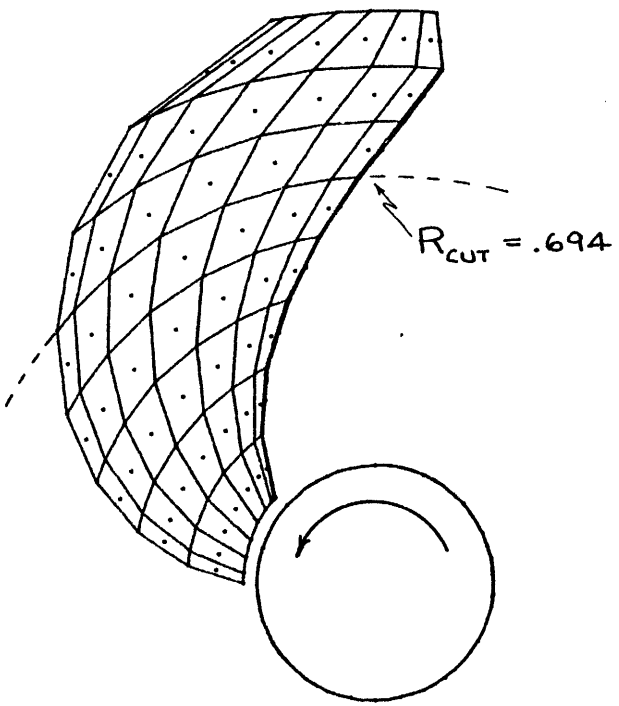

Figure 3.9.1 - Example of global vortex lattice

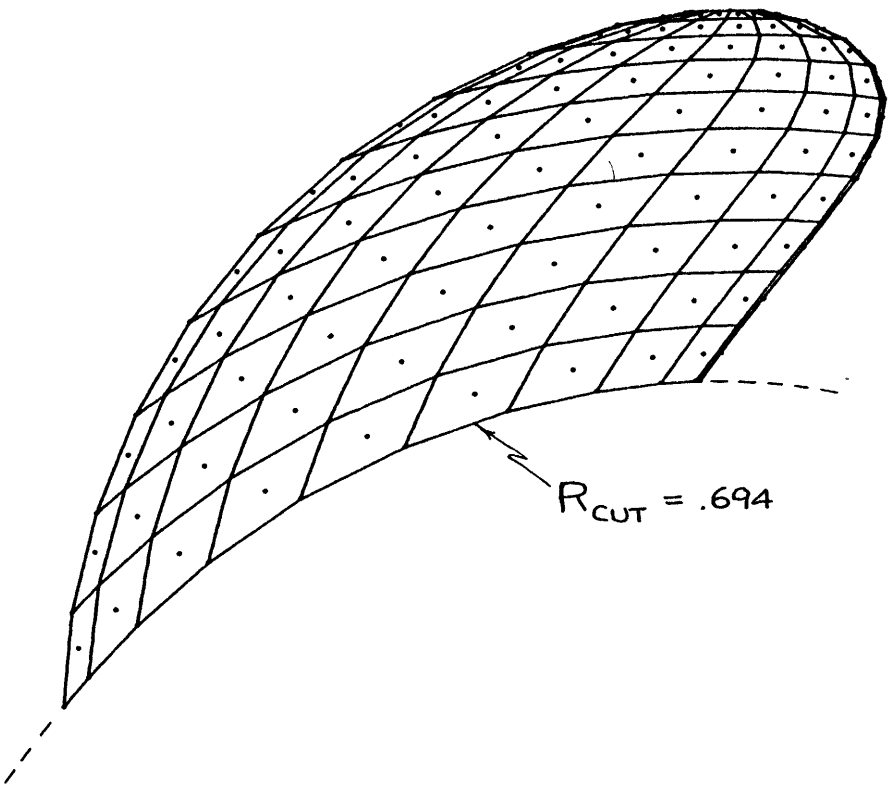

Figure 3.9.2 - Example of local vortex lattice

leading edge suction, the method used here is an integral part of the separated flow modeling in the tip region described in Chapter V.

3.10 Viscous Pitch Correction

The influence of blade boundary layers on propeller performance may be explicitly included in the present approach by altering the right hand side of Eq. 3.6.4 to account for a known boundary layer displacement thickness distribution. However, since solutions for propeller blade boundary layers are not routinely available, the influence of the boundary layers on blade section lift is approximated by reducing the pitch angle of each blade section by the amount

$$\Delta\alpha = 1.9454 \left(\frac{t_o}{c}\right)\left|\frac{f_o}{c}\right| \qquad (3.10.1)$$

where $\Delta\alpha$ is in radians. This is the same viscous pitch correction used by Kerwin and Lee (1978).

IV. Tip Region Leading Edge Flows

4.1 Types of Tip Region Flows

In order to calculate the flow quantities of interest in the tip region a model of the flow must be used. All models involve various approximations of some sort, and the usefulness of any given model depends on how realistic the approximations are and what information about the flow is to be computed. Four models for the types of flow near the blade tip are discussed below, at increasing levels of sophistication. The fact that these are models of the flow, and not representations of the flow itself, must be kept in mind. To simplify the discussion and figures, the flow about wing tips rather than propeller blade tips will be considered. The concepts are the same for either case.

a) Classical Lifting Surface Theory

This theory assumes that the flow is attached to the wing surface everywhere and the trailing vortex wake is shed off the trailing edge only. The wake is assumed to remain flat behind the wing and not roll up into discrete trailing vortices (see Fig. 4.1.1). This model is widely used because of its simplicity, and yields excellent predictions of lift, drag, and pitching moment for moderate- to high-aspect ratio wings. The predicted pressure distribution is also quite good except near the wingtip. Efforts to improve this latter problem by letting the trailing vorticity separate off of the trailing edge and then roll up do not yield much improvement.

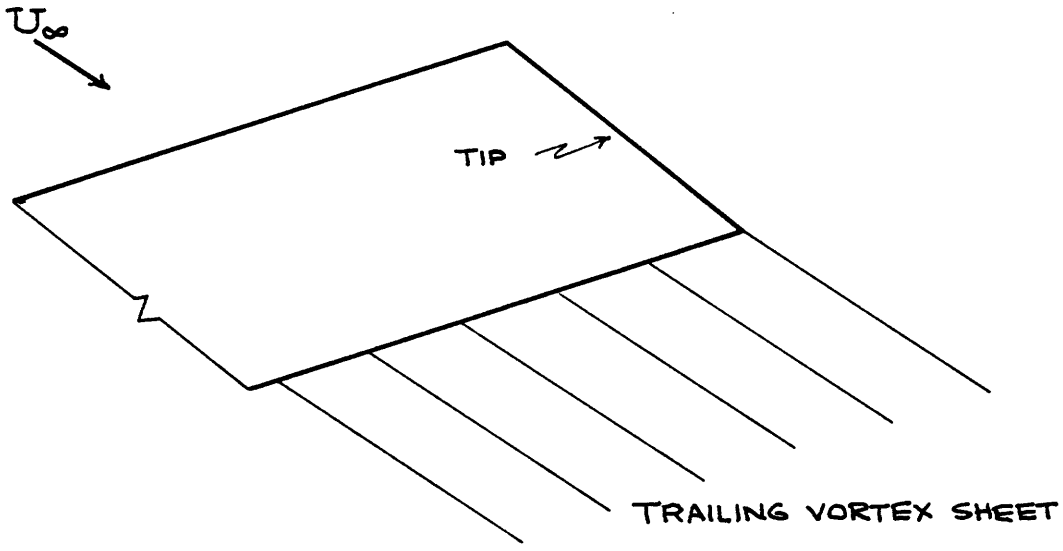

Figure 4.1.1 - Classical wake model

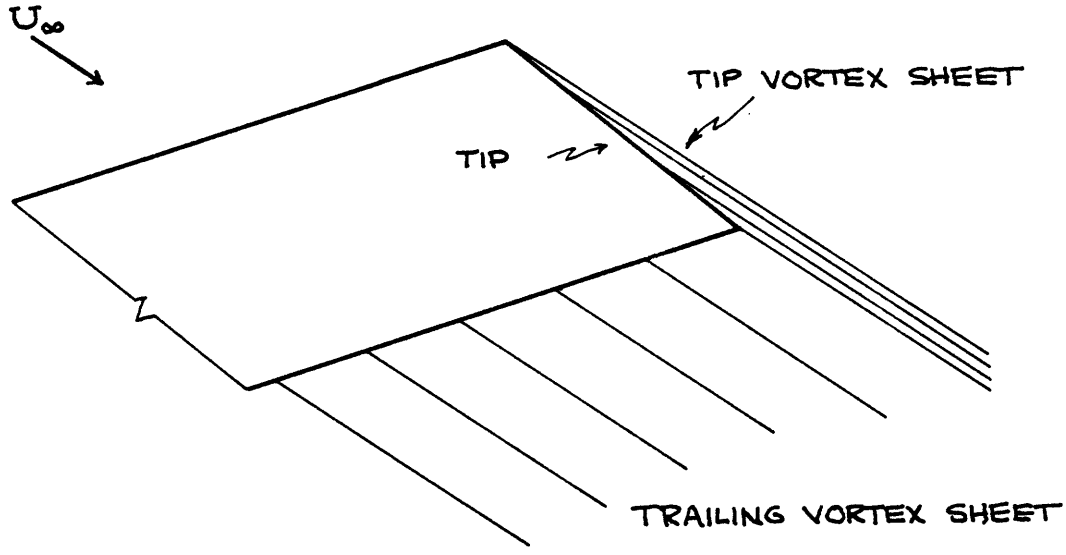

Figure 4.1.2 - Wake model with side edge separation

As already pointed out in Section 3.4, the above model is inadequate for calculating the loads on low aspect ratio propeller blades when they are heavily loaded.

b) Side Edge Separation

At high angles of attack (heavy loading), trailing vorticity is shed off of the tip chord of the wing and starts to roll up before the trailing edge is reached, with the centroid of the vorticity lying above the upper surface wing (Francis and Kennedy, 1979). While this side edge rollup process has been modeled successfully by Maskew (1976), many of the important effects on the wing pressure distribution can be determined by including a "tip vortex sheet" in the model, as shown in Fig. 4.1.2. The presence of a tip vortex sheet increases the circulation in the tip region and moves the center of pressure aft near the tip. The global solution for the propeller flow problem uses this type of model, as shown in Fig. 3.4.1. It is sufficient for calculating the total forces on the blade, but it is not adequate for computing the pressure distribution on the blade in the tip region.

c) Swept Leading Edge Flow (Sharp Edge)

Most propeller blades have leading edges in the tip region that are highly swept relative to the oncoming flow. Even on unskewed propellers, the leading edge is highly swept at the tip unless a finite tip chord is used. Some qualitative feel for the flow around such a swept leading edge may be gained by considering the flow around

a low aspect ratio delta wing. Since most studies of delta wings assume sharp leading edges, we will make this assumption initially. The effect of rounded leading edges will be dealt with subsequently.

A free shear layer separates from the sharp edge of a delta wing at incidence and rolls up into a leading edge vortex (LEV) lying above the wing surface and inboard of the edge, as shown in Fig. 4.1.3. The upper surface of the wing underneath the leading edge vortex is subjected to a strong sidewash, which decreases the upper surface pressures and greatly increases the wing loading and lift. Fig. 4.1.4 shows the pressure distribution on a delta wing as determined by experiment and a very elaborate vortex sheet model for the flow, with the suction peaks underneath the leading edge vortices very prominant. The large increase in lift at high incidence due to leading edge vortices is what enables delta wing aircraft (e.g., Concorde, Space Shuttle) to land at reasonable speeds.

Fig. 4.1.5 shows the surface flow patterns obtained on a sharp edged delta wing, and Fig. 4.1.6 shows the flow pattern in a crossflow plane for this wing. The flow separates at the primary separation line S1 (wing edge), and the resulting vortex sheet coils up above the wing to form the primary vortex core. The fluid near the wing surface flows outward from the primary attachment line A1. (For more discussion of three-dimensional flow separation and attachment, see Appendix D). The crossflow is accelerated as it passes under the primary vortex, but it then encounters an adverse pressure

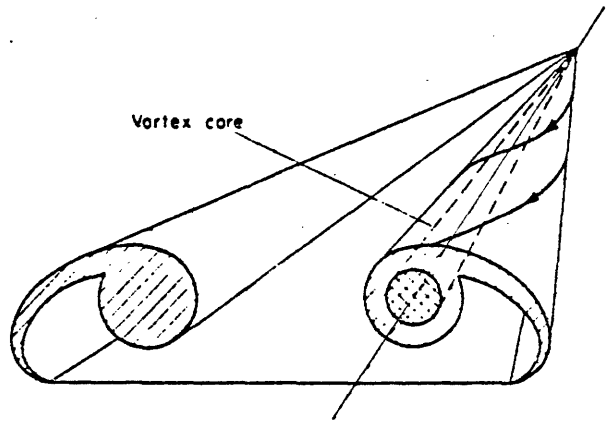

(From Hall, 1966)

Figure 4.1.3 - Vortex cores over slender delta wing

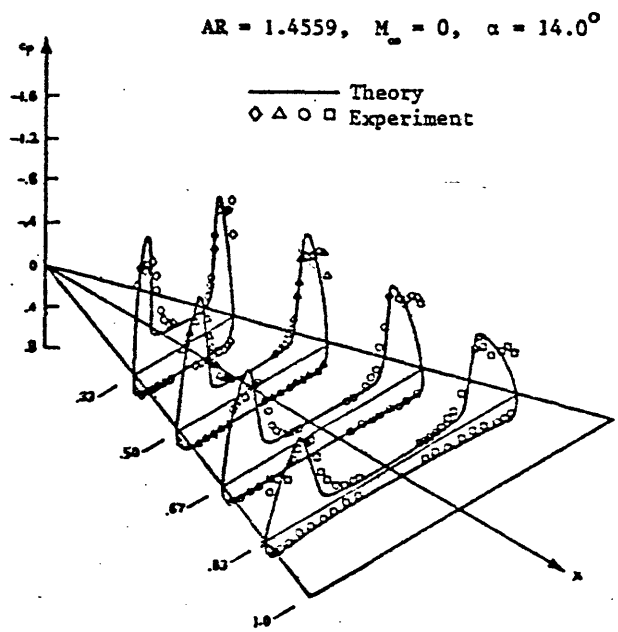

(From Smith, 1978)

Figure 4.1.4 - Pressure distribution on upper surface of delta wing

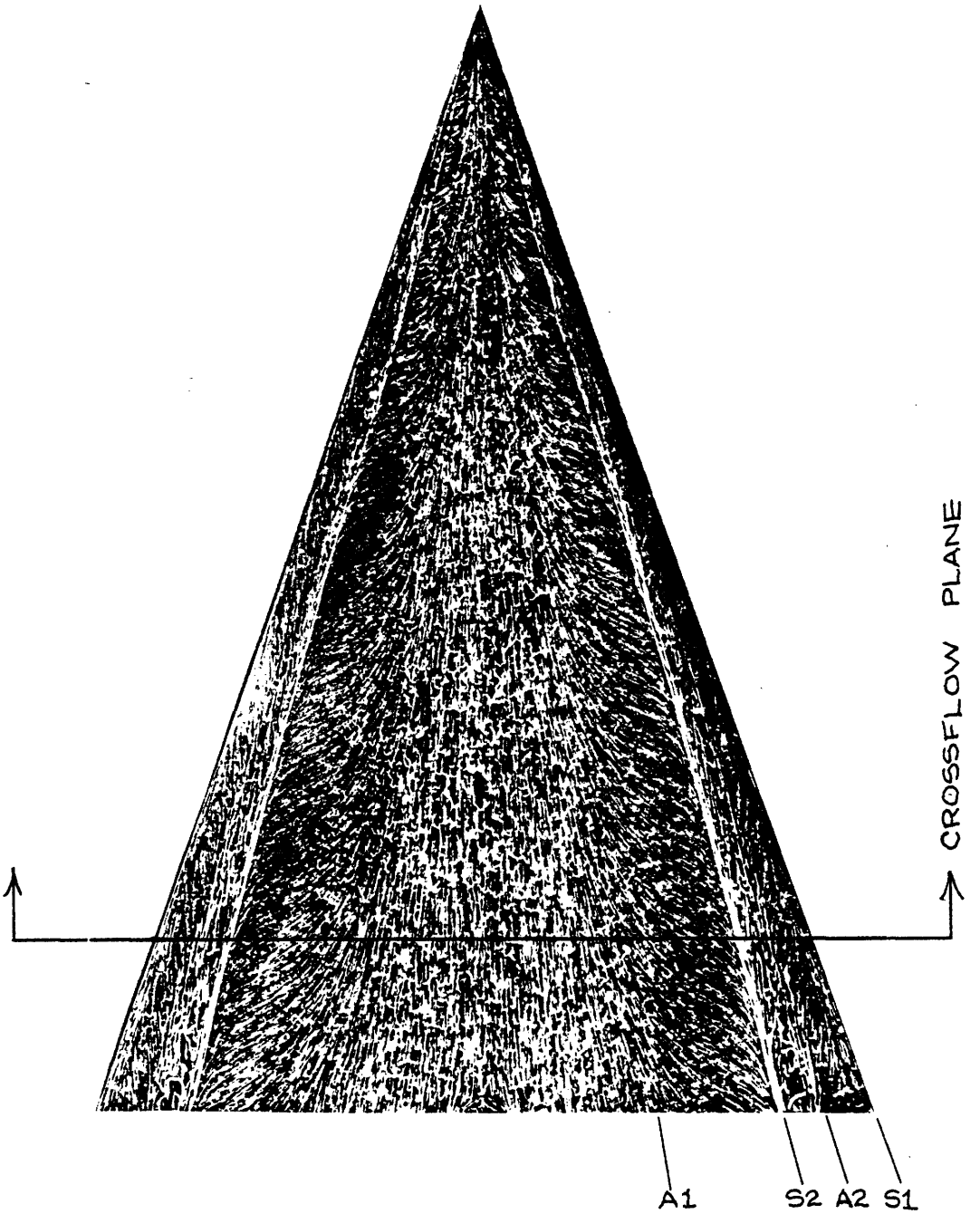

(From Marsden, Simpson, and Rainbird, 1958)

Figure 4.1.5 - Surface flow visualization on upper surface of delta wing (α = 14°)

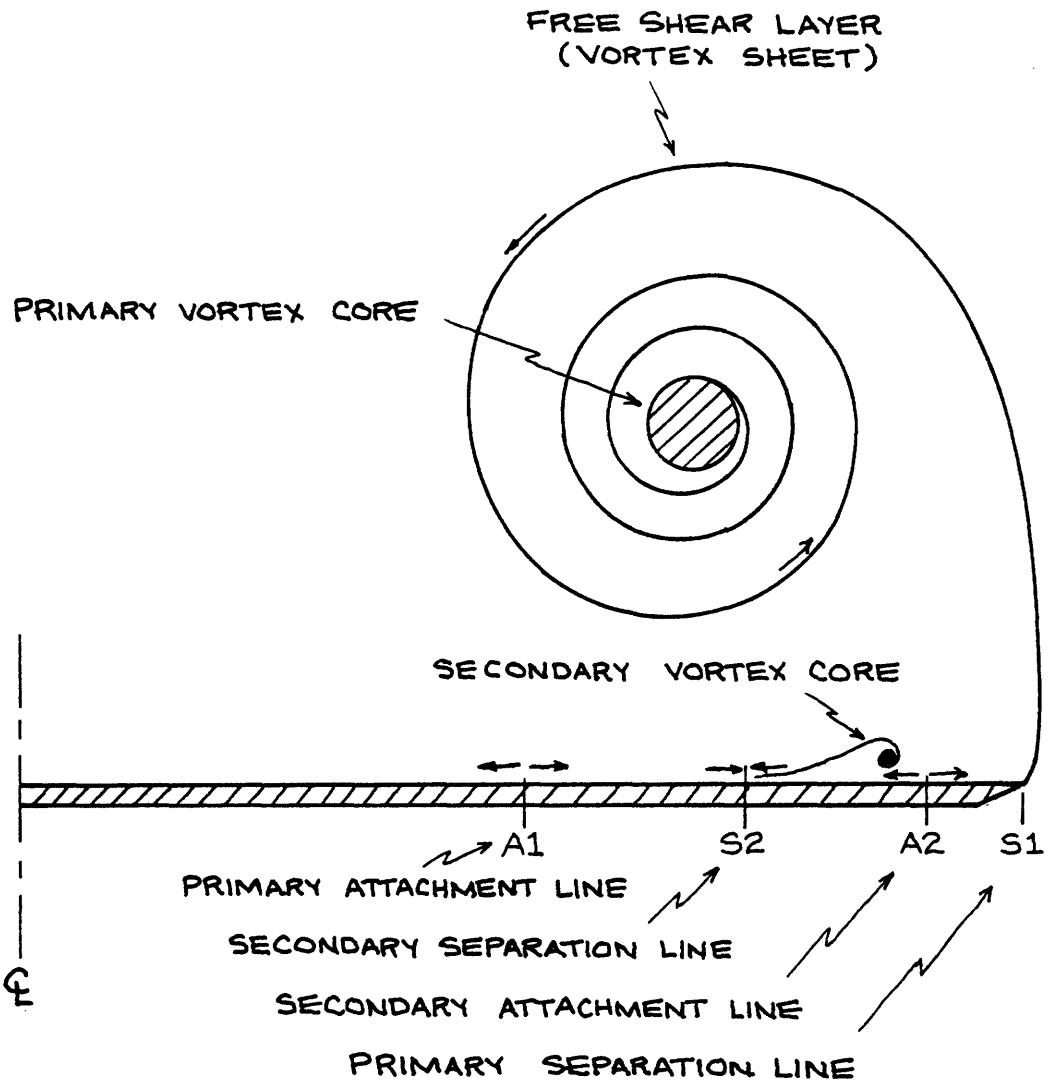

Figure 4.1.6 - Flow pattern in crossflow plane on delta wing

gradient and separates again at the secondary separation line S2, forming the secondary vortex. This process of generating further separations, attachments, and smaller vortex cores proceeds until viscosity and turbulence obliterate the small scale flow structures.

Fig. 4.1.7 shows the results of point tests on three different propellers at 30% slip (J = .70 x P/D). Propellers A and C clearly show an attachment line just inboard of the tip on the suction side, and from this we may infer the presence of a rolled up vortex lying above the blade tip, similar to a leading edge vortex on a sharp-edged delta wing. This type of flow is only pronounced when the propeller is fairly heavily loaded.

The discussion above deals with delta wings having sharp leading edges, so that flow separation along the leading edges occurs at all values of incidence except zero. The theoretical results by Weber et al (1976) shown in Fig. 4.1.4 depend on the wing edge being sharp, so that a Kutta condition (tangential flow requirement) can be applied at the leading edge in the mathematical model. However, propeller blades usually have nicely rounded leading edges in order to delay the appearance of leading edge sheet cavitation. In this case the presence or absence of flow separation at the leading edge depends on the details of the viscous flow, as shown below.

d) Swept Leading Edge Flow (Rounded Edge)

The flow behavior near rounded leading edges on airfoils is often governed by the behavior of laminar separation bubbles (see Appendix C

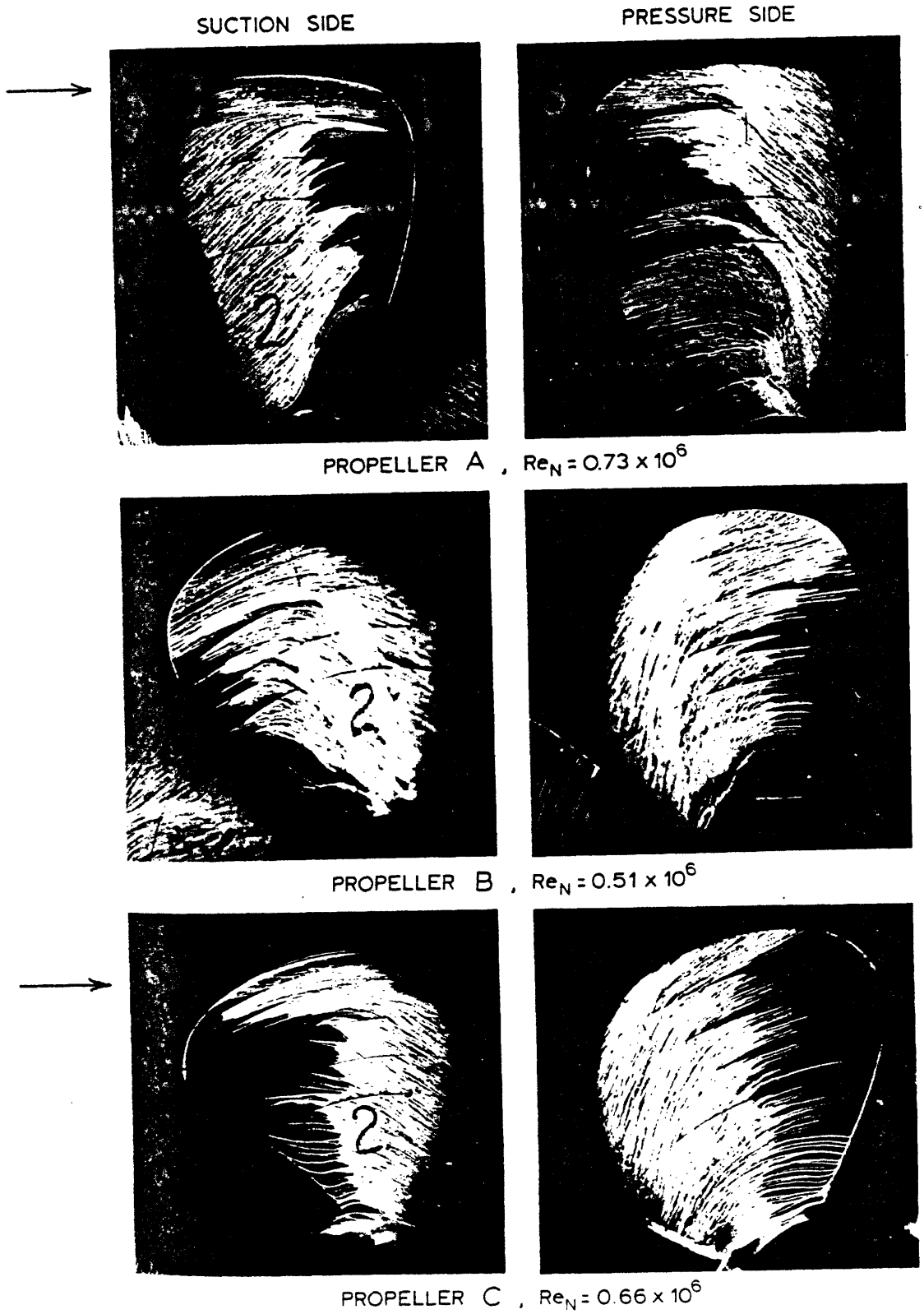

(From Kuiper, 1978)

Figure 4.1.7 - Paint flow patterns on 3 propellers at 30% slip

for a discussion of two-dimensional separation bubbles). If the foil or wing is operating above its ideal angle of attack there will be a suction peak near the nose, and the laminar boundary layer will usually separate and form a free shear layer when it encounters the adverse pressure gradient following the suction peak. This shear layer is quite unstable and undergoes transition to turbulence quite rapidly, at which point the flow usually reattaches to the wing surface as a turbulent boundary layer. There are two types of laminar separation bubbles found in practice:

a) Short bubbles (< 1% chord in length and < 0.01% chord in height) which have almost no effect on the flow around the foil except directly underneath the bubble, and

b) Long bubbles (>> 1% chord in length) which drastically alter the flow around the foil section, usually destroying the suction peak near the leading edge and producing a region of moderately low pressure under the bubble.

For a thin two-dimensional airfoil section a short bubble appears first as the incidence is increased above the ideal angle of attack, and at some point the short bubble "bursts" and a long bubble is formed. Kuchemann (1953) noted that the tips of swept-back wings operate at a higher effective angle of incidence (greater leading edge suction peak) than do the inboard sections as the angle of attack of the wing is increased. One would expect therefore that a short separation bubble would burst near the tip of the wing first as the

incidence is increased. Since the jump between a short and long bubble involves a rearrangement (and reduction) of the bound vorticity on the foil, a "part-span vortex" (PSV) must be shed from the junction between short and long bubbles on a swept wing, as shown in Fig. 4.1.8.

Figs. 4.1.9 illustrate some pressure distribution data on a 45° swept back wing of aspect ratio 3. Fig. 4.1.9a shows the minimum pressure near the leading edge as a function of span for several angles of attack. At α=20.6° and α=22.6° the suction peak has collapsed over the outer part of the wing, indicating the presence of a long bubble in this region. Fig. 4.1.9b confirms this, showing the chordwise distribution of upper surface pressure at the 61% semispan station for several angles of attack. The pressure distribution at α=16.4° is quite normal, and the short bubble most likely present does not show up in the pressure plot. At α=20.6° the suction peak has been greatly reduced by the presence of a long bubble, which is also responsible for the extended region of low pressure. The junction between short and long bubbles (and the associated part-span vortex) moves inward as the wing incidence is increased, giving rise to swept wing stall.

Figs. 4.1.10 and 4.1.11 illustrate the part span vortex phenomenon on a highly skewed propeller blade in steady flow, where the "tip" vortex has been made visible by reducing the water tunnel static pressure so that vortex cavitation occurs. The "tip" vortex leaves the tip of the blade when operating near the design advance coefficient

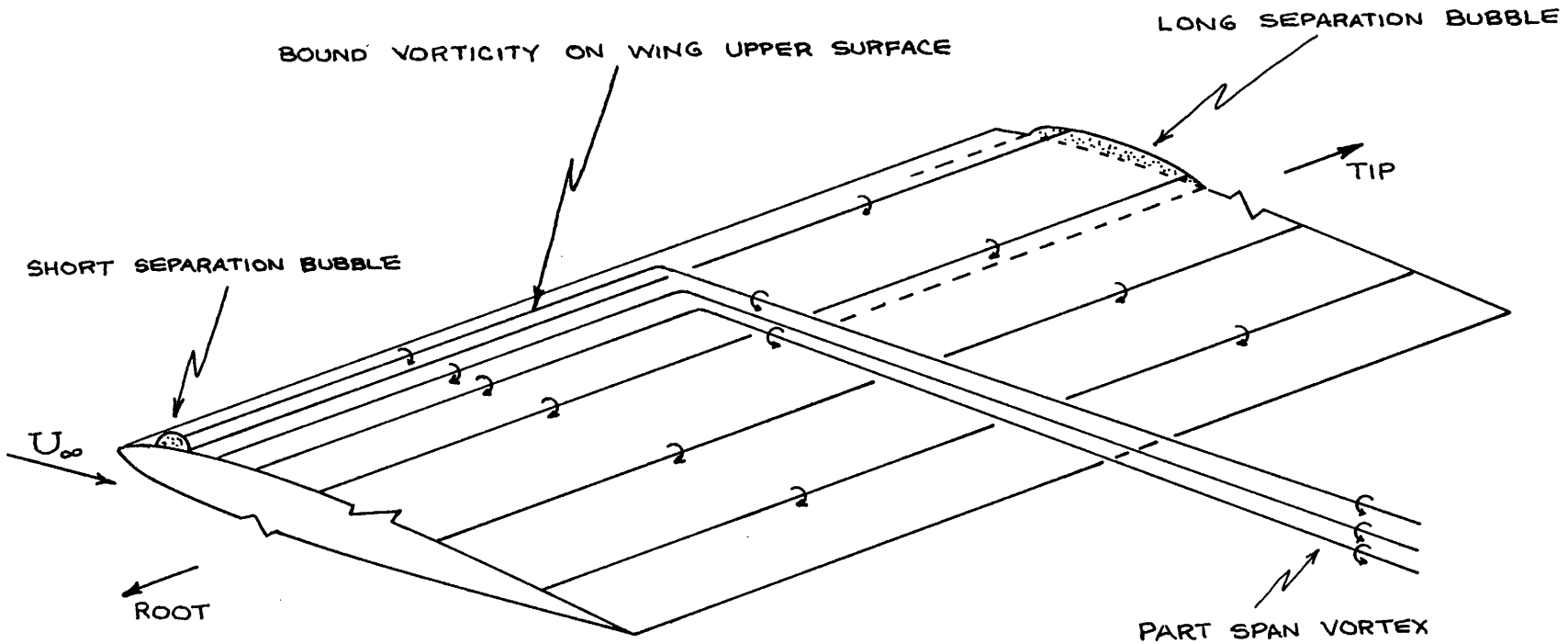

(FROM KÜCHEMANN, 1953)

Figure 4.1.8 - Formation of part-span vortex on swept wing

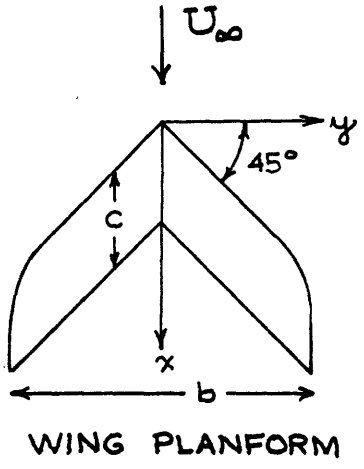

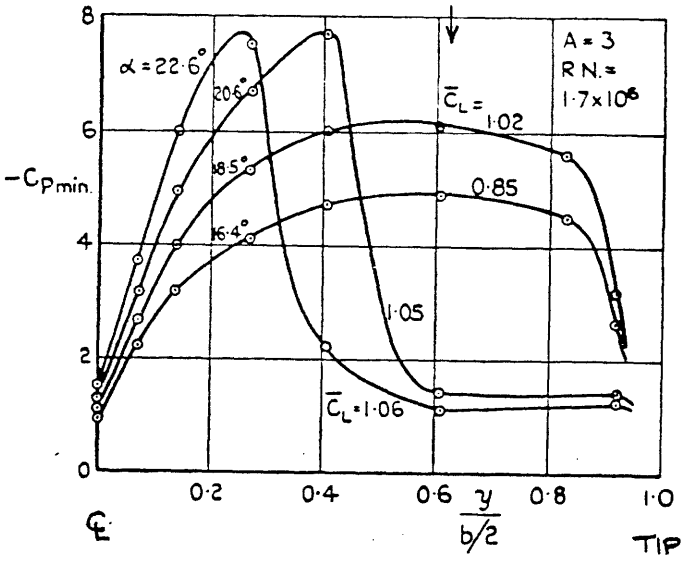

FIG. 4.1.9a MINIMUM PRESSURE NEAR LEADING EDGE ON 45° SWEPT-BACK WING vs. FRACTION OF SEMI-SPAN

(FROM KÜCHEMANN, 1953)

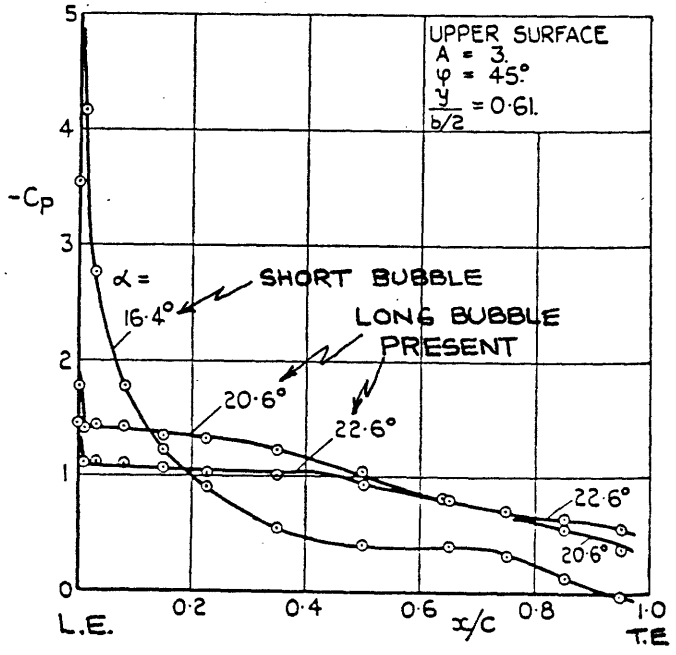

FIG 4.1.9b PRESSURE DISTRIBUTION OVER CHORD @ 61% SEMI-SPAN FOR WING OF FIG 4.1.9a

Figure 4.1.9 - Pressure distribution on swept-back wing

Figure 4.1.10 - Highly skewed propeller (#4498) operating near design J
(Tip vortex leaves tip of blade)

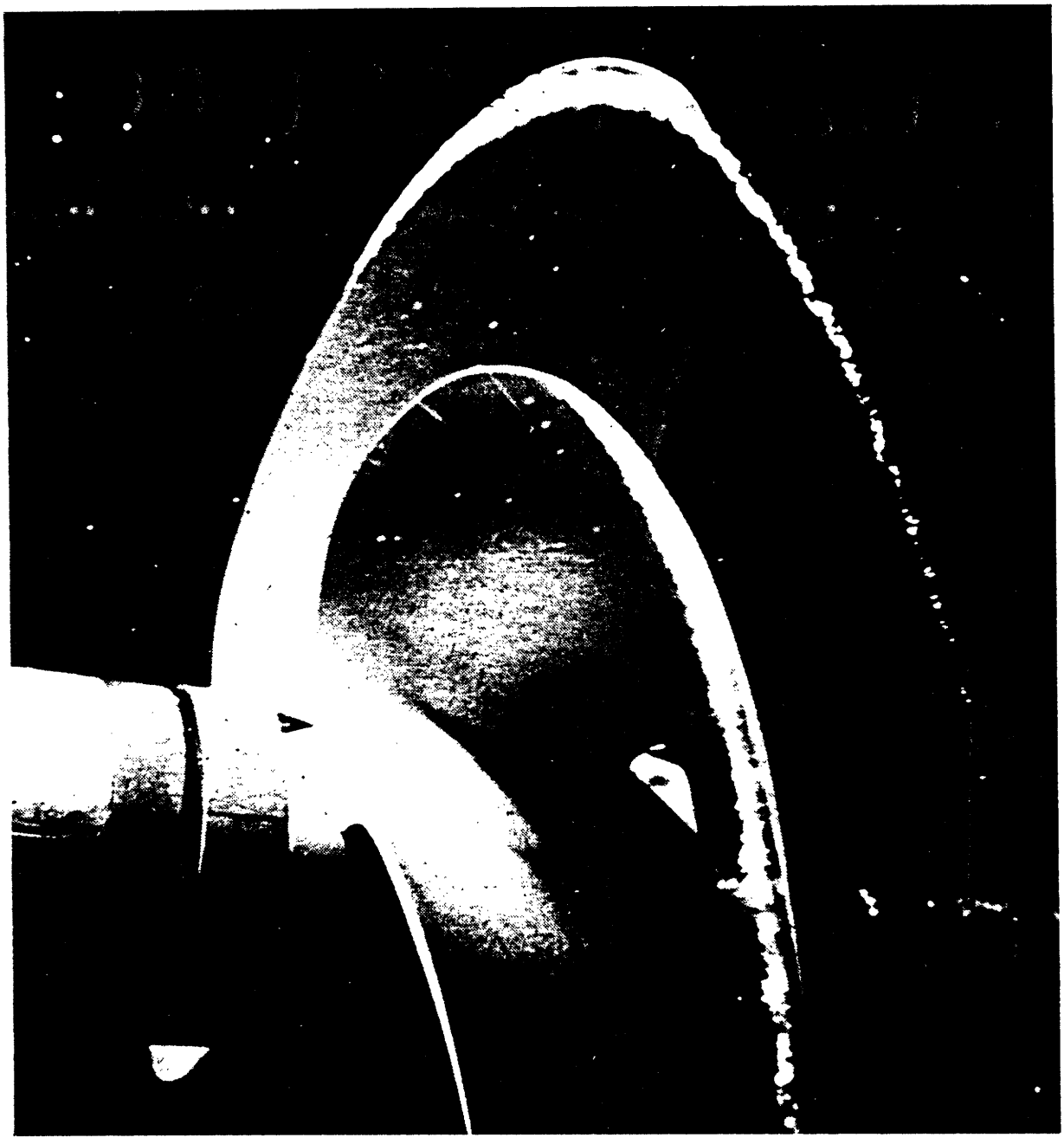

Figure 4.1.11 - Highly skewed propeller (#4498) operating at 60% of design J
(Tip vortex separates from leading edge and passes over blade)

(Fig. 4.1.10), but it separates quite far down the leading edge at a lower J and passes over the blade (Fig. 4.1.11).

If the part span vortex occurs very near the tip of a propeller blade where the leading edge sweep angle is changing rapidly with radius, the distinction between a part span vortex and a leading edge vortex is somewhat difficult to make. In the current work "part span vortex" will refer to a distinct vortex separating quite far down the leading edge of a propeller blade, while "leading edge vortex" will refer to the rolled up vortex downstream of a region of leading edge separation near the tip. A leading edge vortex tends to resemble a side edge vortex as the leading edge sweep angle approaches 90° (streamwise edge).

It is the intent of the present work to model the part span vortex phenomenon on propeller blades in an approximate manner. It is obvious from the above discussion that the first major problem is determining where the flow separates from the leading edge. The rest of this chapter explains the physics of viscous leading edge flows in greater detail, and the method developed to predict the starting point of a part span vortex on a propeller blade.

4.2 Viscous Leading Edge Flows

As noted in Section 4.1, laminar separation bubbles are a common feature on unswept wings when operating above their ideal angles of incidence. The flow remains laminar at the separation point up to very high free-stream Reynolds numbers because the flow from the

stagnation point to the suction peak is in a favorable pressure gradient which damps out instability and transition mechanisms (Tollmein-Schlicting waves and subsequent three-dimensional disturbances) which would tend to make the leading edge boundary layer turbulent. After the laminar boundary layer separates and forms a free shear layer it is much more susceptible to instabilities, and usually becomes turbulent and reattaches to the airfoil surface, forming a bubble of trapped fluid. If the flow reattaches shortly behind the separation point a short bubble is formed which has very little effect on the main flow. If the flow progresses quite far downstream before reattachment occurs a long bubble is formed, which drastically alters the pressure distribution on the foil upper surface. A further discussion of short and long bubbles is given in Appendix C.

Additional complications arise when considering separation bubbles on swept leading edges because mechanisms other than Tollmein-Schlicting instabilities may govern transition near the leading edge. The first mechanism is 'cross-flow instability' (Beasley, 1973) and is characterized by streamwise vortices in the laminar boundary layer. These vortices develop near the leading edge where there is a large chordwise velocity gradient. The boundary layer velocity profile viewed in a direction normal to the external inviscid streamline may contain a point of inflection, which is indicative of instability at low Reynolds numbers. Fig. 4.2.1 shows how this inflected cross-flow profile occurs.

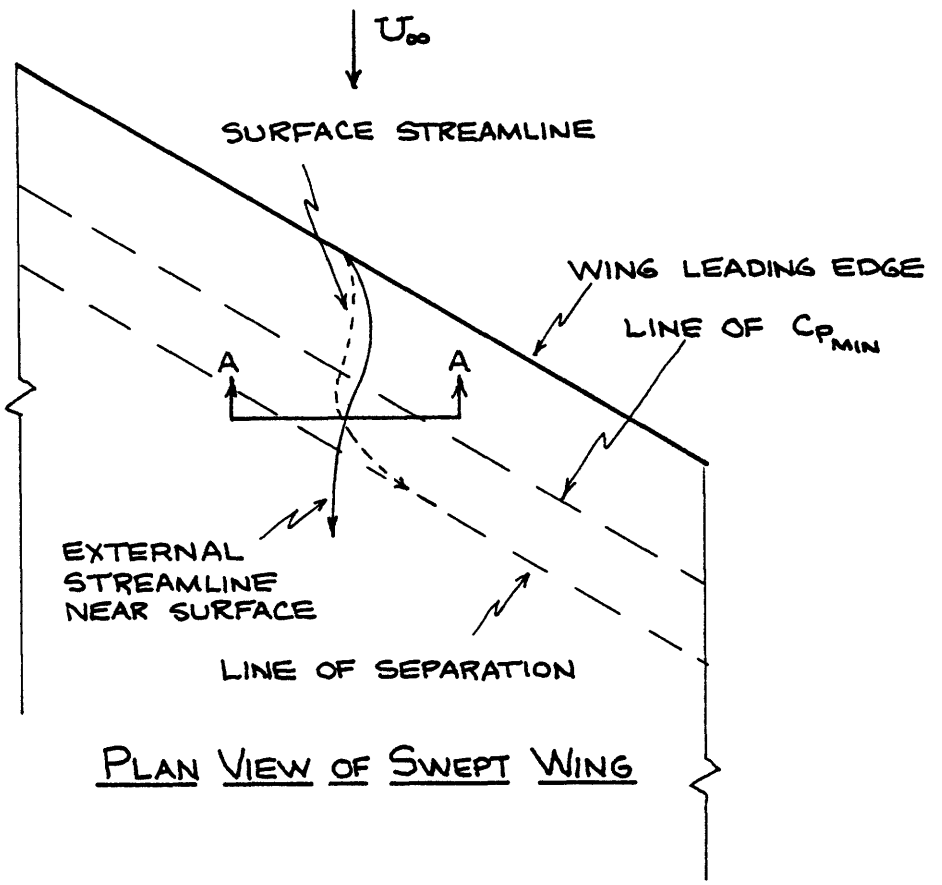

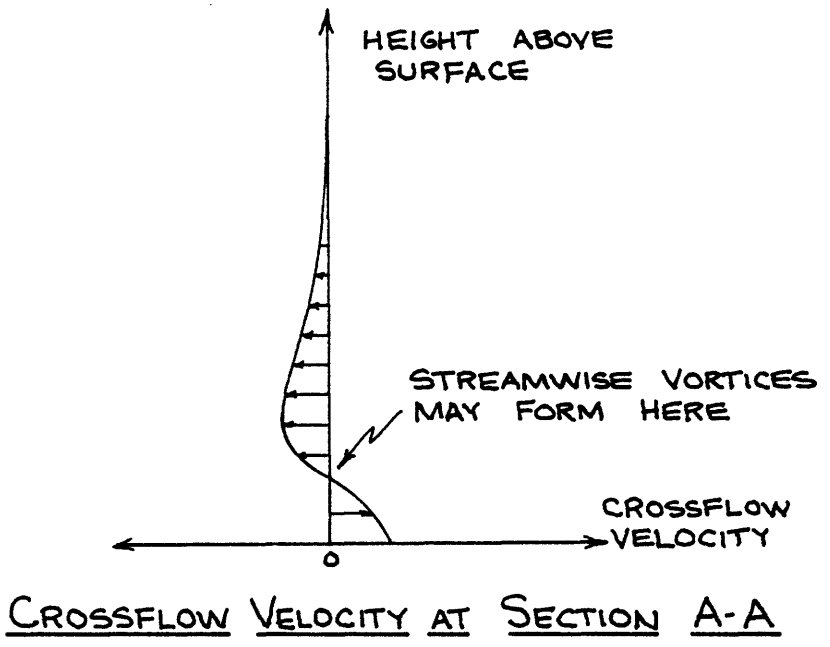

Figure 4.2.1 - Crossflow boundary layer profile near leading edge

A much more important mechanism is 'leading edge contamination', as described by Gaster (1967) and Cumpsty and Head (1967). In this case the flow along the forward attachment line of a swept wing is turbulent, so that turbulence propagates out along the span of a swept wing from the upstream (inboard) end, and the boundary layer around any section of the wing is initially turbulent without the need for undergoing Tollmein-Schlicting type instability and transition. Fig. 4.2.2 illustrates the attachment line flow on an infinite swept wing, with leading edge sweep angle Λ and inflow velocity U_∞. The component of the inflow normal to the leading edge is $U_n = U_\infty \cos\Lambda$, and the component of the inflow along the attachment line is $U_s = U_\infty \sin\Lambda$. The momentum thickness θ_{al} of the boundary layer along the attachment line (assuming laminar flow) is given by (Gaster, 1967),

$$\theta_{al} = 0.4044 \frac{\sqrt{\nu}}{\sqrt{\frac{dU_e}{ds}}} \qquad (4.2.1)$$

where ν = kinematic viscosity

$\frac{dU_e}{ds}$ = velocity gradient of component of potential flow normal to the leading edge, evaluated at the attachment line

and the Reynolds number describing the attachment line flow is given by

$$R_{\theta_{al}} = \frac{U_s \theta_{al}}{\nu} \qquad (4.2.2)$$

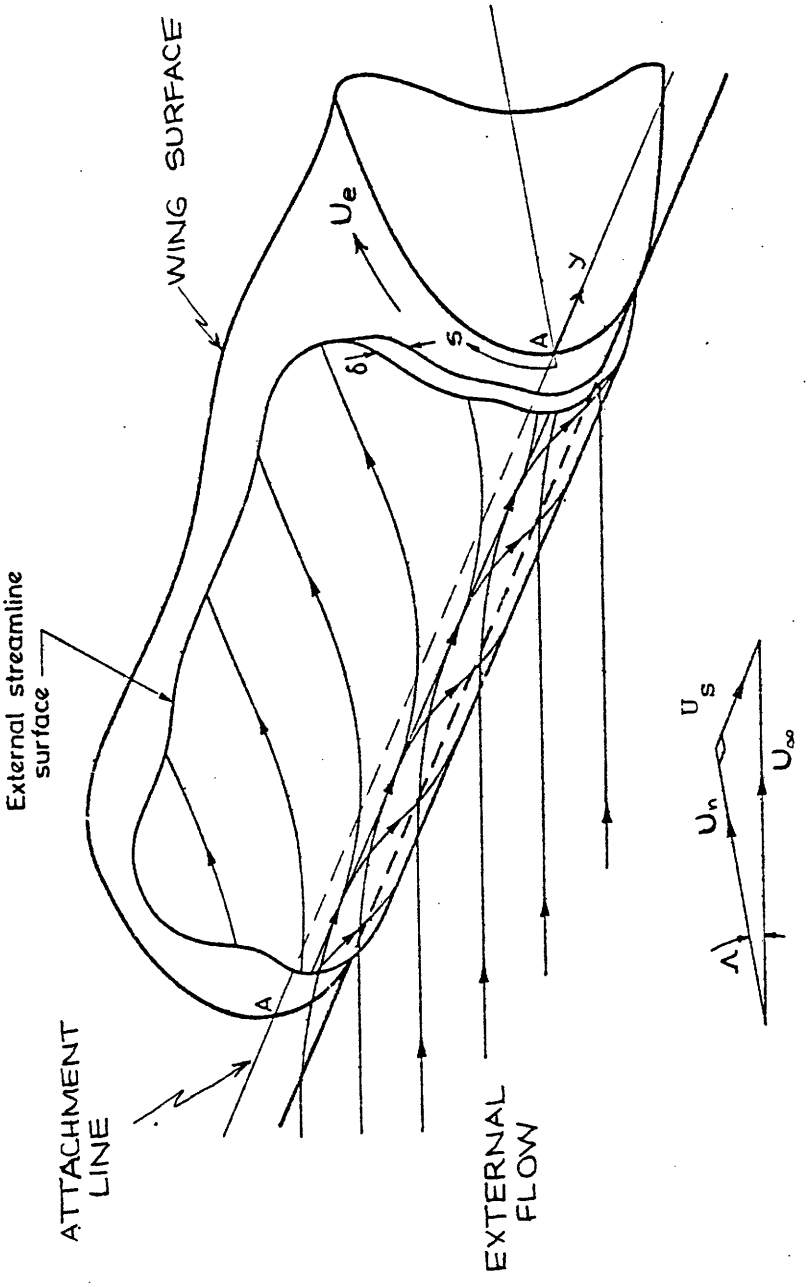

(From Poll, 1977)

Figure 4.2.2 - Swept leading edge attachment line flow (infinite sheared wing)

Although there are no definite values of $R_{\theta_{al}}$ which differentiate between different flow regimes, Beasly (1973) suggests the following values:

$R_{\theta_{al}} < 100$: no turbulent contamination possible (disturbances die out)

$100 < R_{\theta_{al}} < 240$: turbulent contamination possible (disturbances will propagate)

$R_{\theta_{al}} > 240$: turbulent contamination (attachment line boundary layer unstable to disturbances)

An additional complication occurs when the boundary layer around a section of a swept wing starts at a (possibly) turbulent attachment line but undergoes re-laminarisation as it passes through the favorable pressure gradient leading up to the suction peak. Launder and Jones (1968) suggested that re-laminarisation may occur if the parameter K_r exceeds 5×10^{-6}, K_r being defined as

$$K_r = \frac{\nu}{U^2} \frac{dU}{ds} \qquad (4.2.3)$$

where U = velocity along inviscid streamline

$\frac{dU}{ds}$ = velocity gradient along inviscid streamline

In addition to the considerations described here, it is expected that inflow turbulence and surface roughness may significantly influence flow transition and separation in the leading edge region of wings and propeller blades.

4.3 Prediction of Leading Edge Flow Behavior-Theory

The most important item to be determined from a viscous flow analysis of the leading edge of a swept wing or propeller blade is the point (if any) at which a part span vortex forms. If we accept the hypothesis put forward by Kuchemann (1953) and Smith (1975) that this point is where a short laminar separation bubble bursts, then whatever prediction method is used should predict the bursting of two-dimensional laminar separation bubbles as the leading edge sweep approaches zero.

The problem appears far too complicated for a direct theoretical assault, especially since instability and transition are involved, and these phenomena continue to defy an army of researchers. Therefore the approach taken here is to try to identify the relevant non-dimensional parameters governing the problem and collect as much data as possible upon which to regress, so that a semi-empirical model can be developed to predict the occurrence of part span vortices.

Two major assumptions were made in developing the leading edge flow model presented below:

a) It is assumed that each point on the leading edge can be considered to be part of an infinite sheared wing (Appendix E) having the same leading edge sweep and the same velocity gradients along the surface normal to the leading edge. This is equivalent to ignoring flow gradients along the direction of the leading edge: only those gradients normal

to the leading edge are assumed to matter. While it seems that spanwise gradients should be important at the leading edge of a low-aspect ratio wing or propeller blade tip, it is far from obvious how to include them in the model.

b) The attached flow inviscid load distribution calculated in Section 3.9 is used as input to the viscous flow calculations. Since the presence of a part span vortex radically alters the load distribution on the wing or propeller blade, it would seem necessary to iterate between the viscous leading edge analysis and a potential flow calculation which included the part span vortex, until convergence is obtained. There are two justifications for not doing so. Dixon and Sampath (1978) tried this approach in a very elaborate model for predicting flow separation on wings with round edges and found no convergence possible. They finally concluded that the leading edge boundary layer should be calculated only once, using the attached flow velocity distribution (their methodology has not been adopted for the present work due to excessive computing time and inconclusive results). A second reason for neglecting viscid-inviscid iteration is that a part-span vortex has little effect on the wing pressure distribution inboard of it, so the inviscid pressure distribution calculated, assuming completely attached flow, is probably quite accurate inboard of the actual part span vortex location.

As noted above, the flow at any point of the leading edge is assumed to be equivalent to that along an infinite sheared wing having the same leading edge sweep angle relative to the flow and the same distribution of the inviscid velocity component along the surface normal to the leading edge. If we make the further assumption that the leading edge region of a wing or blade section in a plane normal to the leading edge (Fig. 4.3.1) can be satisfactorily represented by a parabola having the same leading edge radius, then the surface velocity component normal to the leading edge in inviscid flow can be calculated using the equations in Appendix F. The only quantity remaining to be specified is the position of the stagnation point on the section normal to the leading edge (position of attachment line on infinite sheared wing). The descriptor used in the current work is the suction force per length of leading edge, F_s. This is convenient because calculations of the attached potential flow using thin wing theory (Appendix A) yield the leading edge suction force directly. A non-dimensional leading edge suction force coefficient is defined as

$$C_s = \frac{F_s}{\frac{1}{2}\rho U_n^2 r_n} \qquad (4.3.1)$$

where U_n = component of inflow velocity normal to leading edge

r_n = radius of leading edge in plane normal to leading edge

Note that C_s does not contain Λ.

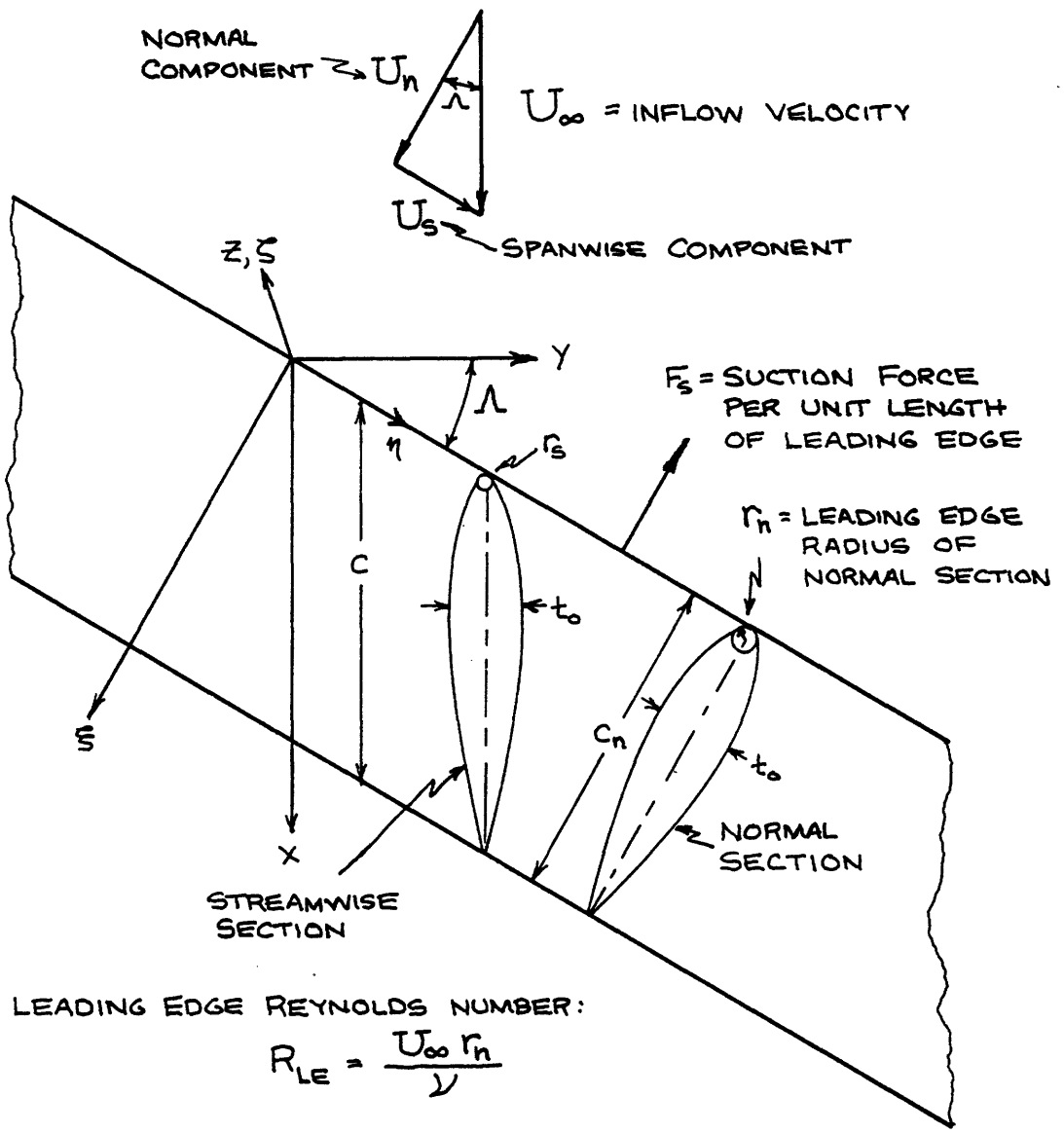

LEADING EDGE REYNOLDS NUMBER:

$$R_{LE} = \frac{U_\infty r_n}{\nu}$$

LEADING EDGE SUCTION FORCE COEFFICIENT:

$$C_s = \frac{F_s}{\frac{1}{2} \rho r_n U_n^2}$$

Figure 4.3.1 - Flow past infinite sheared wing

The proper Reynolds number for describing the leading edge flow on swept wings was determined to be

$$R_{le} = \frac{U_\infty r_n}{\nu} \qquad (4.3.2)$$

While it might be argued that U_n is the proper velocity to use, in accordance with infinite sheared wing theory, it must be remembered that the equations for the chordwise and spanwise components of the flow on a sheared wing only uncouple in the cases of inviscid flow or an attached laminar boundary layer. Once separation or turbulence appears the chordwise and spanwise flow velocities interact. Since we are concerned about leading edge flows involving separation and transition to turbulence it appears that U_∞ is the proper velocity to use in forming a leading edge Reynolds number.

4.4 Prediction of Leading Edge Flow Behavior - Correlation of Experimental Data

Wind tunnel data for swept wings [Black (1953), Garner and Bryer (1957), Garner and Walsh (1960), Garner and Cox (1961), Woodward and Lean (1971), Garner (1972)] was collected and analyzed using the following procedure:

a) For a given wing geometry, free stream Reynolds number, and angle of attack, the attached potential flow load distribution was determined using a vortex-lattice computer program very similar to the one used for the global propeller analysis.

b) The following quantities were computed at a series of points along the leading edge:

i) Λ - leading edge sweep angle

ii) $R_{\theta_{al}}$ - Reynolds number of attachment line flow (Eq. 4.2.2)

iii) K_r - relaminarisation parameter (Eq. 4.2.3)

iv) C_s - leading edge suction force coefficient (Eq. 4.3.1)

v) R_{le} - leading edge Reynolds number (Eq. 4.3.2)

c) The values of the above quantities were determined at the point along the leading edge where the part span vortex originiated.

d) The above process was repeated for a variety of different wings at different free stream Reynolds numbers and different angles of attack. The values of the parameters at the part span vortex separation point were cross plotted in various ways in a search for some sort of correlation.

The best correlation between parameters was obtained between C_s and R_{le}, as expected. The process used to generate one data point for the final C_s vs. R_{le} plot is shown in Fig. 4.4.1, and all of the resulting data points are shown in Fig. 4.4.2. The scatter in the data is discouraging but not surprising, given the strong influence of surface roughness and turbulence shown for the 49.4° swept wing. There are inaccuracies in estimating C_s also, since the influence of the wing boundary layer was not considered in determining the attached flow loading distribution, and Küchemann (1955) has shown that the influence

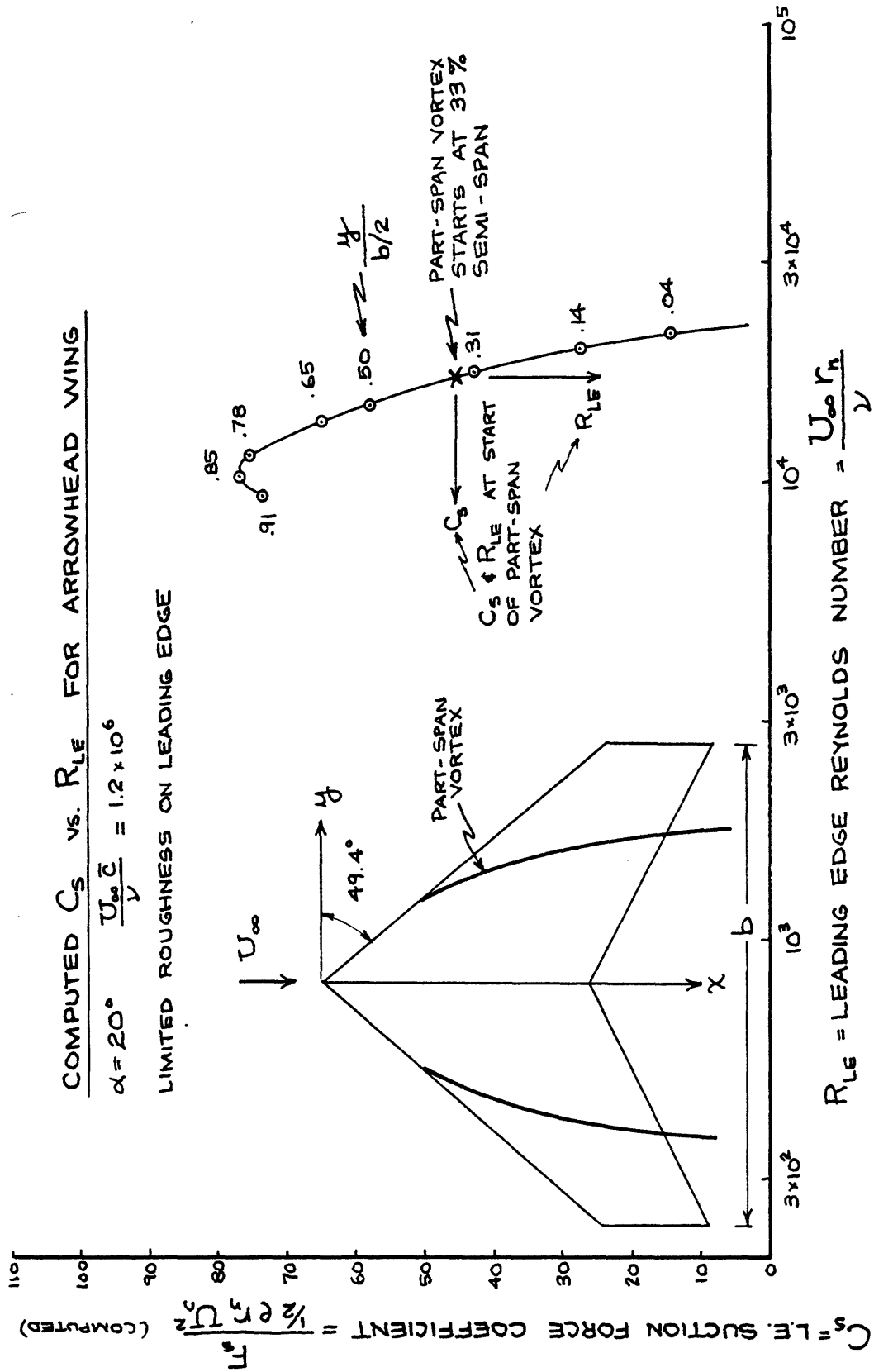

Figure 4.4.1 - Example of determination of R_{LE} and C_s at part-span vortex separation point

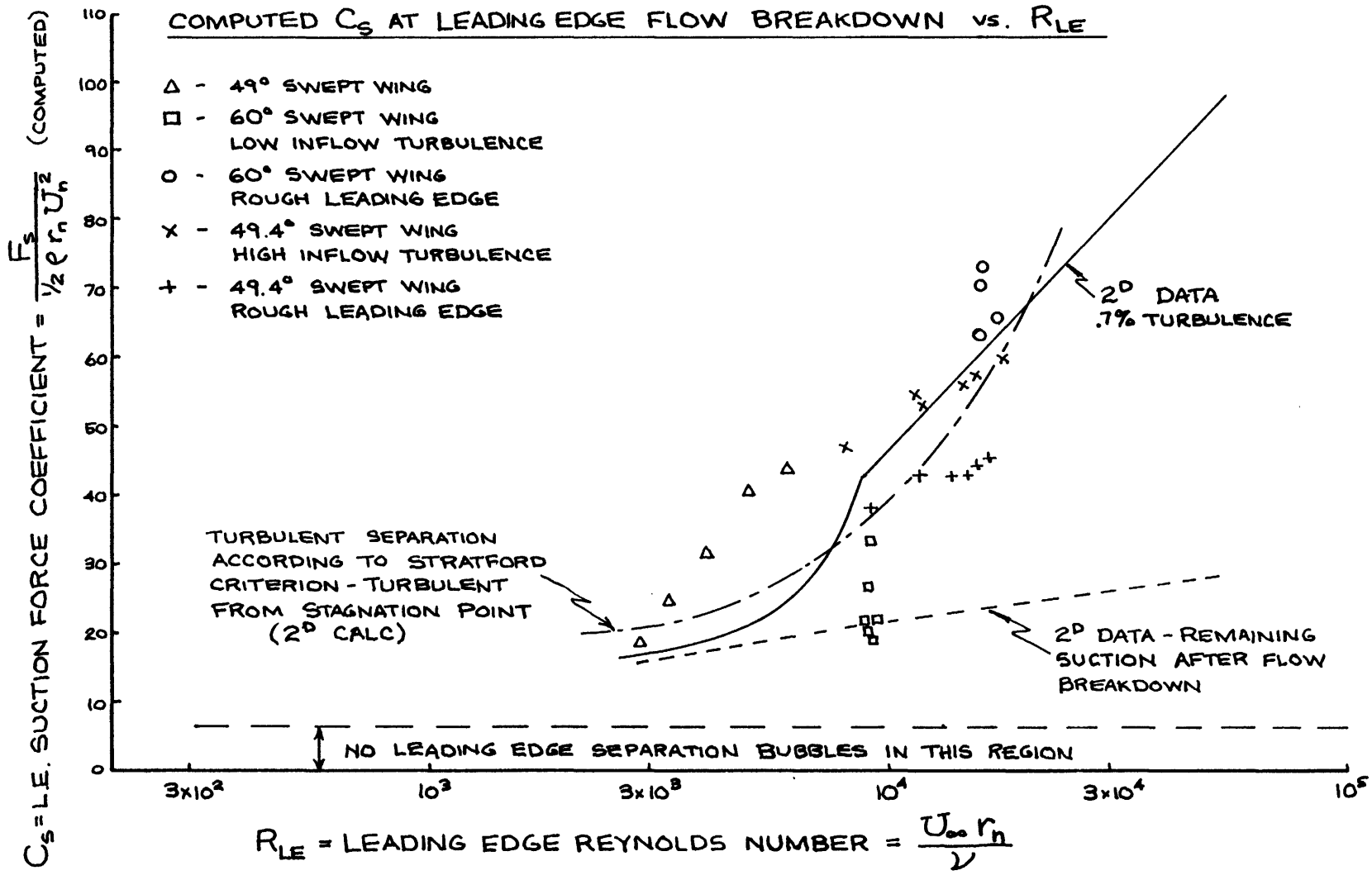

Figure 4.4.2 - C_s vs. R_{LE} at leading edge flow breakdown (data)

of the boundary layer increases with sweep. Nevertheless, there is a clear correlation between R_{le} and the computed C_s at the point where the part span vortex separates from the wing. No significant correlation could be found involving Λ, $R_{\theta_{al}}$ or K_r, although in some cases a high value of $R_{\theta_{al}}$ (indicating possible turbulent attachment line flow) occurred simultaneously with a high value of C_s at separation, which is to be expected.

Three other curves are shown in Fig. 4.4.2. The solid line is taken from Ridder (1974) and represents the results of a series of tests on two-dimensional airfoil sections. The line plotted is the maximum attainable leading edge suction force coefficient C_s (just before flow breakdown occurs) versus leading edge Reynolds number R_{le}. For the portion of the curve to the left of the knuckle ($R_{le} < 8.6 \times 10^3$) the cause of the flow breakdown is bursting of a short laminar separation bubble. To the right of the knuckle ($R_{le} > 8.6 \times 10^3$) the cause of flow breakdown is turbulent separation behind a short laminar bubble.

The line across Fig. 4.4.2 at $C_s = 6.5$ is the lower limit for the formation of laminar separation bubbles near the leading edge of a two dimensional section. This line was calculated using the velocity distribution around a parabolic leading edge (Appendix F) and the laminar boundary layer separation criterion developed by Stratford (1957a). This criterion is independent of Reynolds number, as it should be.

The dashed line is the computed C_s at which turbulent boundary layer separation is predicted to occur near the leading edge of two dimensional sections. This calculation was made using the inviscid velocity distribution around a parabolic leading edge and the turbulent boundary layer separation criterion due to Stratford (1957b).

The fact that both two-dimensional experimental data and the computed turbulent separation line pass through the experimental points for flow separation on swept wings is extremely encouraging. This appears to indicate that C_s and R_{le} are proper descriptors for the state of the leading edge flow on both swept and unswept wings. Other factors certainly influence the leading edge flow behavior, such as $R_{\theta_{al}}$, K_r, spanwise pressure gradients, surface roughness, and inflow turbulence; but the limited amount of detailed swept wing flow data available makes a correlation with these parameters difficult or impossible at present. It seems clear, however, that the suction force coefficient C_s and leading edge Reynolds number R_{le} are the most important parameters to consider.

Putting a line through all of the data shown in Fig. 4.4.2 results in a sort of "universal curve" for predicting the onset of leading edge flow breakdown, which is presented in Fig. 4.4.3. If the leading edge flow at some point on a wing has a computed C_s lying above the solid line in Fig. 4.4.3, then flow breakdown is expected. If the computed C_s lies below this limiting curve, then a short laminar separation bubble is predicted to occur. Applying

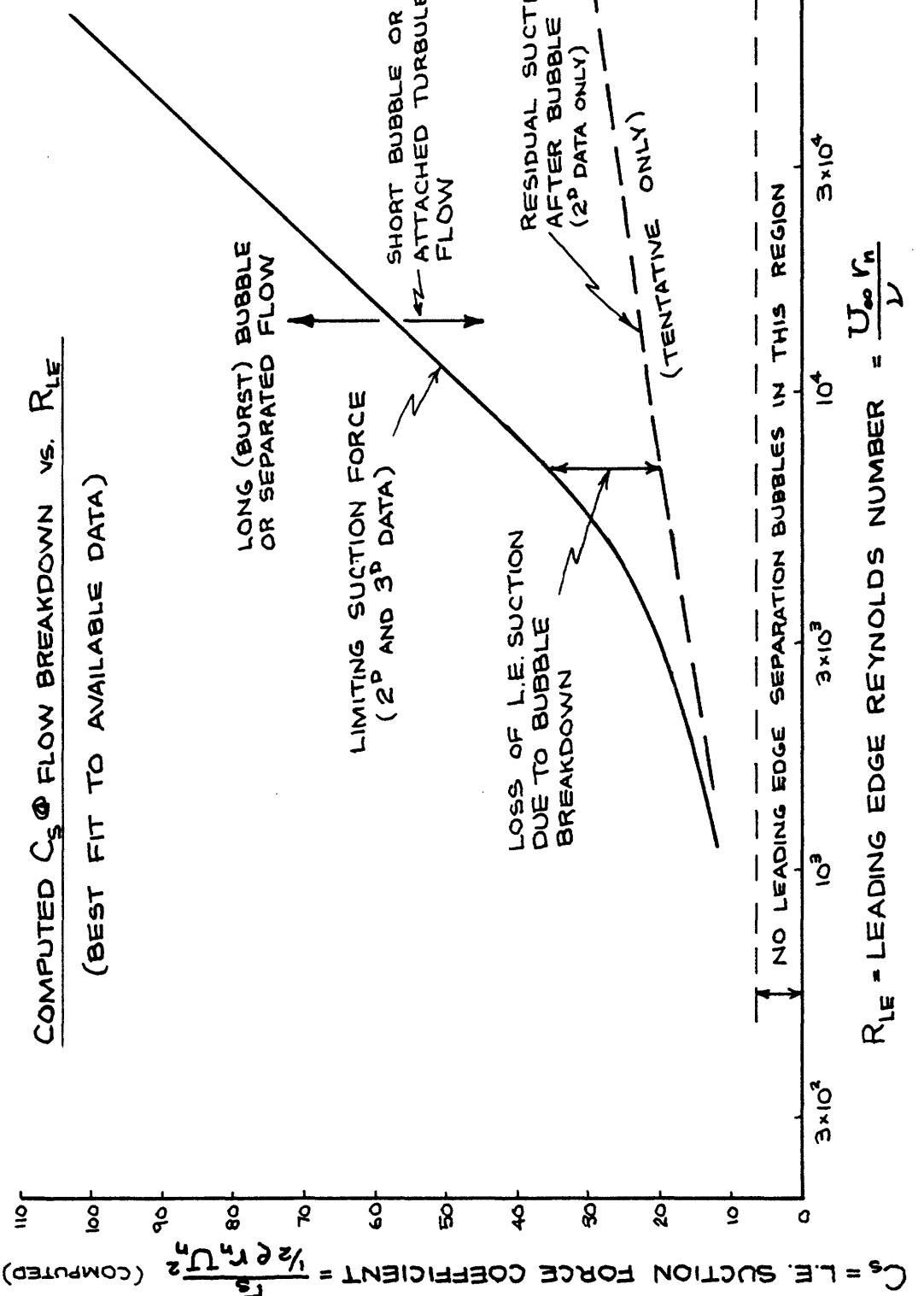

Figure 4.4.3 - C_s vs. R_{LE} at leading edge flow breakdown (Best fit to data)

this procedure to the case of propeller blades, good results are obtained in predicting the occurrence and origin of part span vortices, as shown in Chapter VI.

The dashed curve in Fig. 4.4.3 represents the level of suction force remaining after leading edge flow breakdown occurs. This curve is taken from Ridder (1974) and represents two-dimensional airfoil data only. The importance of this curve will become clear in Chapter V, but for now it suffices to say that swept wing data must be obtained to see if this curve holds for three dimensional wings also. At present this curve must be considered as tentative only.

V. Modeling of Tip Region Separated Flow

5.1 Physical Description

As shown in Chapter IV, heavily loaded wings and propeller blades often shed vorticity into the fluid from the leading edge as well as the trailing edge. Since the vorticity shed from the leading edge passes very close to the wing or blade, it is essential to correctly determine the strength and location of this shed vorticity in order to determine the load distribution on the blade.

Figure 4.1.10 (page 65) shows a heavily loaded propeller with a very strong part span vortex being shed from the leading edge. While it may appear that vorticity is being shed from only one location on the leading edge in this case, vortex shedding is actually occurring along the entire length of the leading edge outboard of the initial separation point. The vorticity shed from the leading edge then rolls up into the part span vortex core, so that the circulation around the core increases in the outward (downstream) direction.

At propeller loadings less severe than that shown in Fig. 4.1.11 (operation closer to design J), the initial separation point moves outward on the blade, and the strength of the vorticity shed from the leading edge is reduced. Perhaps more importantly, the tendency for the vorticity shed from the leading edge to toll up tightly is reduced. While adequate photographs of this phenomena are not available, detailed visual observations in the MIT Variable Pressure Water Tunnel of two different model propellers indicate that the tendency toward strong

rollup of the leading edge shed vorticity is reduced as the propeller loading is reduced. Flow visualization was accomplished by noting the trajectories of minute cavitation bubbles emanating from nicks in the blade leading edges. Hence, it would appear that for many cases of interest (operation not too far away from design J) the vorticity shed from the blade leading edge tends to resemble a vortex sheet rather than a tightly rolled up vortex core. Ideally, any model used to represent this separated flow should indicate the basic form of the shed vorticity (sheet or core) as part of the solution.

The amount of vorticity shed from the leading edge of a propeller blade or wing is determined by the nature of the flow at the leading edge. If the leading edge is sharp it is appropriate to impose a Kutta condition there to insure that velocities near the leading edge remain bounded. This is sufficient to determine the amount of vorticity shed from the leading edge using a wide variety of theoretical flow models. In fact, there are a tremendous number of papers in the aeronautical literature dealing with flow separation from the leading edges of low aspect ratio delta wings (see Figs. 4.1.4-4.1.6), and almost all utilize a leading edge Kutta condition in an inviscid flow model to predict the flow around the wing. In many cases this is quite a reasonable assumption: delta wings on supersonic aircraft tend to be quite thin and have very small leading edge radii.

However, propeller blades typically have generous leading edge radii to delay sheet cavitation inception so that a Kutta condition at the leading edge is inappropriate. The vortex shedding rate is actually determined by the details of the viscous flow near the leading edge. Just as in the leading edge separation problem discussed in Chapter IV, a frontal assult on the leading edge viscous flow problem for the purpose of determining the vortex shedding rate does not seem warranted at this time. A semi-empirical approach is utilized here, as in Chapter IV. Section 5.2 (below) shows that the amount of vorticity shed into the flow once leading edge flow breakdown occurs can be related to the residual leading edge suction force. For present purposes this is taken from an empirical correlation (the dashed line in Fig. 4.4.3, pg. 83).

Once the amount of vorticity shed from the leading edge is determined, the major problem in completing the flow solution is to determine the proper trajectory of the shed vorticity as it passes close to the blade surface. The proper boundary condition for the shed vortex sheet is that there is no pressure jump across it. For the inviscid steady-flow model used here this is satisfied if

$$\underline{\omega} \times \underline{V} = 0 \qquad (5.1.1)$$

everywhere on the sheet; i.e., the local vorticity vector must be parallel to the local velocity vector everywhere on the sheet in order for the sheet to be force-free.

The vortex sheet shed from the leading edge causes significant induced velocities on the blade, which will change the vorticity distribution on the blade required to satisfy the zero normal velocity boundary condition. Conversely, a change in vorticity distribution on the blade will change the velocity field seen by the free vortex sheet, and hence its correct (force-free) position. It is necessary to use an iterative approach to solve this non-linear problem, switching back and forth between satisfying the zero normal velocity boundary condition on the blade (determining the vortex strengths everywhere), and relaxing the position of the free vortex sheet. Under-relaxation of the free sheet position is usually necessary in order to make this process convergent.

5.2 Existing Methods for Solving Lifting Wing Problems with Leading Edge Separation

Several existing methods for determining the flow about slender delta wings with leading edge separation are discussed below in order to set the stage for the separated flow model utilized in the current work.

a) Conical Flow Theories

The British aeronautical community (e.g. Smith (1957), Clapworthy and Mangler (1974)) has devoted a great deal of effort toward analyzing delta wing flows utilizing the conical flow assumption. This assumption states that the flow in all planes normal to the direction of flight is self-similar. The problem is attacked by solving the two-

dimensional Laplace equation in the cross-flow plane by using conformal mapping techniques (including the influence of the leading edge vortices) and then including the streamwise interaction effects in the downstream direction only. Since upstream effects cannot be included the trailing edge Kutta condition is not satisfied. While much insight has been gained by pursuing conical flow theory for delta wings, the lack of applicability to more general geometries renders it useless for the problem at hand.

b) Vortex Lattice Method of Kandil, Mook, and Nayfeh

Kandil, Mook, and Nayfeh (1976) presented a vortex lattice technique for determining the flow about wings with arbitrary planform, camber, and angle of attack having leading-edge separation. The method is restricted to sharp leading edges, so that a leading edge Kutta condition may be imposed.

The method is based on the usual vortex lattice lifting surface theory such as that described in Chapter III. In addition to the horseshoe vortices and associated control points on the wing surface, there are "leading-edge horseshoes" which extend up the trailing wake to the wing trailing edge, through the wing to the leading edge, and then out of the leading edge and extending downstream to form part of the leading edge vortex sheet (see Fig. 5.2.1). By arranging the whole vortex system into horseshoe vortices Kelvin's theorem is automatically satisfied. For each leading edge horseshoe vortex a control point is added at the leading edge of the wing; requiring the

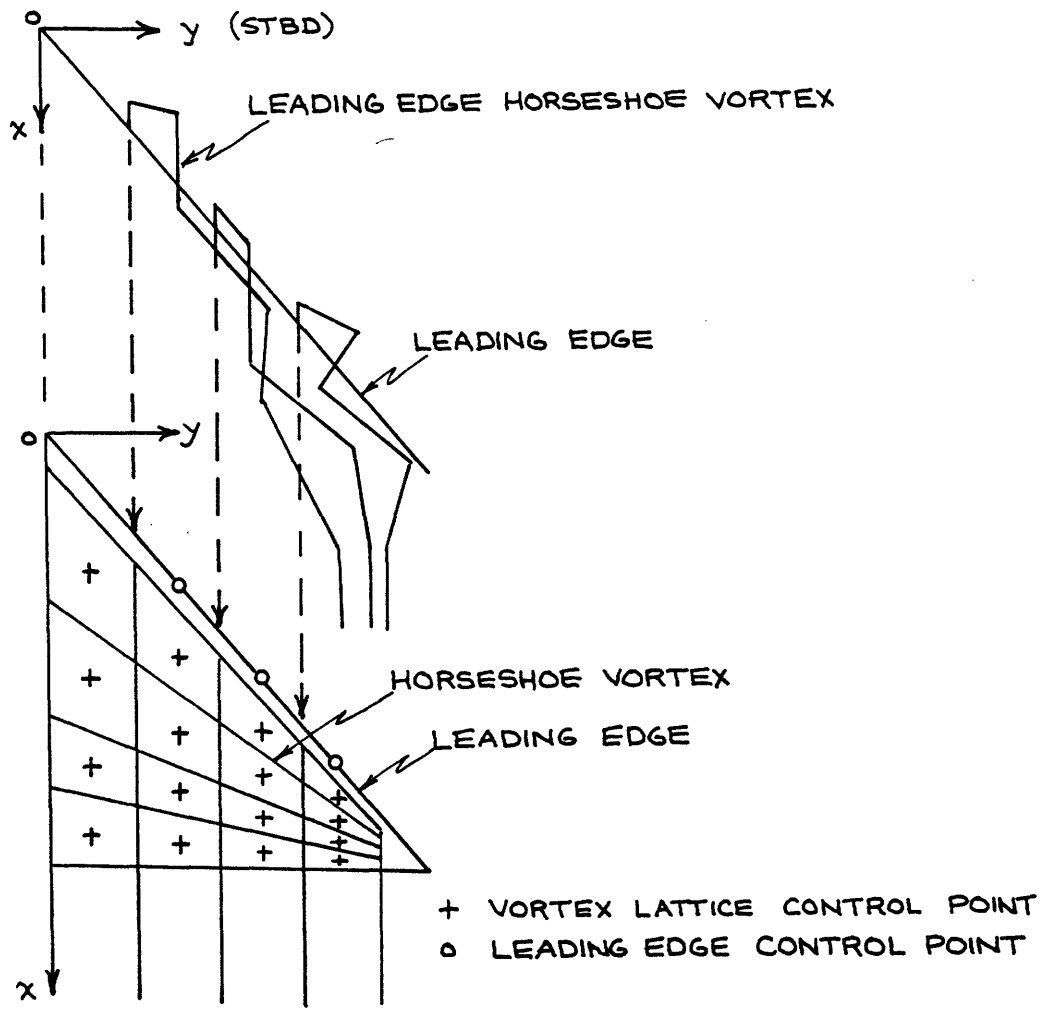

(From Kandil, Mook, & Nayfeh, 1976)

Figure 5.2.1 - Vortex lattice arrangement in Kandil, Mook, & Nayfeh model

total normal velocity to be zero there is equivalent to enforcing a leading edge Kutta condition.

The following iterative approach is used to solve the non-linear boundary value problem:

1) Initial positions for the discrete vortex segments representing the shed vortex sheet are selected.

2) A matrix $\underline{\underline{A}}$ of influence coefficients is computed from the Biot-Savart law: element A_{ij} represents the normal velocity induced at the j'th control point by a unit strength of the i'th horseshoe vortex (either in the wing, or a leading edge horseshoe vortex)

3) The strengths of all of the horseshoe vortices are determined by solving the set of simultaneous equations:

$$\sum_{j=1}^{NCP} A_{ij} \Gamma_j = -V_{nj} \quad , \quad i = 1, \ldots, NCP \qquad (5.2.1)$$

where

Γ_j = strength of the j'th horseshoe vortex

V_{nj} = normal component of the inflow velocity at the j'th control point

NCP = total number of control points

4. With the strengths of all of the discrete vortices known, the velocity at the upstream end of each vortex segment in the shed vortex sheet is computed, and the segment is aligned

with this computed velocity. Since the changing geometry of the free sheet changes the calculation of the velocity, this is an iterative procedure. This process is continued until the shed vortex sheet is force free for the assumed vorticity distribution on the wing.

5) Steps 2), 3), and 4) are repeated until the displacement of the free sheet vortex segments during step 4) is below a certain tolerance and a converged solution is obtained.

Fig. 5.2.2 shows a converged solution using this approach for a flat delta wing with aspect ratio = 1.46 and angle of attack = 14°. Note that the wake is represented by straight semi-infinite segments at some point behind the trailing edge in order to reduce computation time. This is reasonable because the minute details of the wake geometry behind the trailing edge do not significantly affect the loads on the wing.

c) Vortex Lattice Theory of Mehrotra and Lan

Mehrotra and Lan (1978) developed a vortex lattice theory for delta wings with leading edge flow separation which is quite similar to that developed by Kandil, Mook, and Nayfeh (1976). The unique feature in Mehrotra and Lan's work is that any arbitrary amount of leading edge suction force can be specified as part of the solution, and not just the case of zero leading suction force (leading edge Kutta condition). Mehrotra and Lan admitted that they did not know how to establish what the correct leading edge suction force should

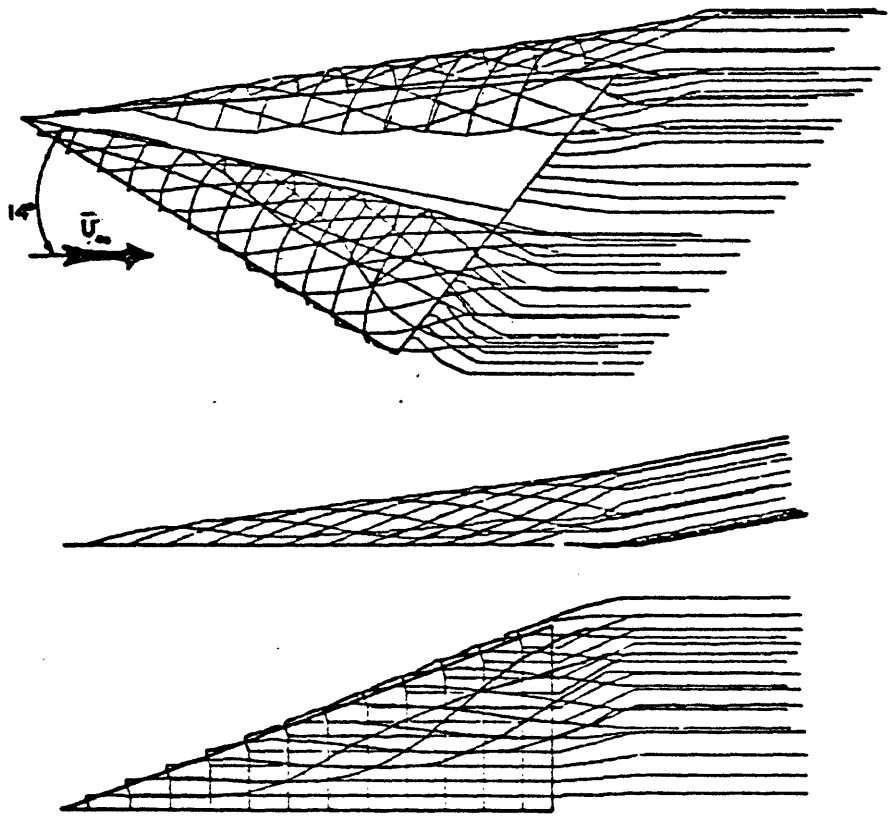

(From Kandil, Mook, & Nayfeh, 1976)

Figure 5.2.2 - Typical solution of wake shape for a delta wing using Kandil, Mook, & Nayfeh model

be for a rounded leading edge with partial separation. The semi-empirical correlation for leading edge suction force developed in Chapter IV (Fig. 4.4.3, pg. 83) can be used to supply this missing information.

Section A.3 in Appendix A shows that the leading edge suction force on a three-dimensional wing can be calculated from a vortex lattice program if cosine spacing of the bound vortices over the chord is utilized. In this case the suction force per unit length of leading edge is proportional to the square of the normal velocity computed at a leading edge control point ahead of the first bound vortex (Fig. 5.2.3). This calculation can be inverted to yield the proper normal velocity at the leading edge control points so that the desired leading edge suction force is attained.

When considering usual attached flow (no leading edge separation) the leading edge control points do not enter into the simultaneous equations to determine the bound vorticity distribution. The normal velocity at the leading edge control points is calculated after the vortex strengths are determined so that the leading edge suction force can be calculated. If the normal velocity is to be specified at several leading edge control points as part of the solution, then an equal number of leading edge horseshoe vortices of unknown strength must be included so that there are as many unknowns as there are equations. The resulting simultaneous equations can be expressed

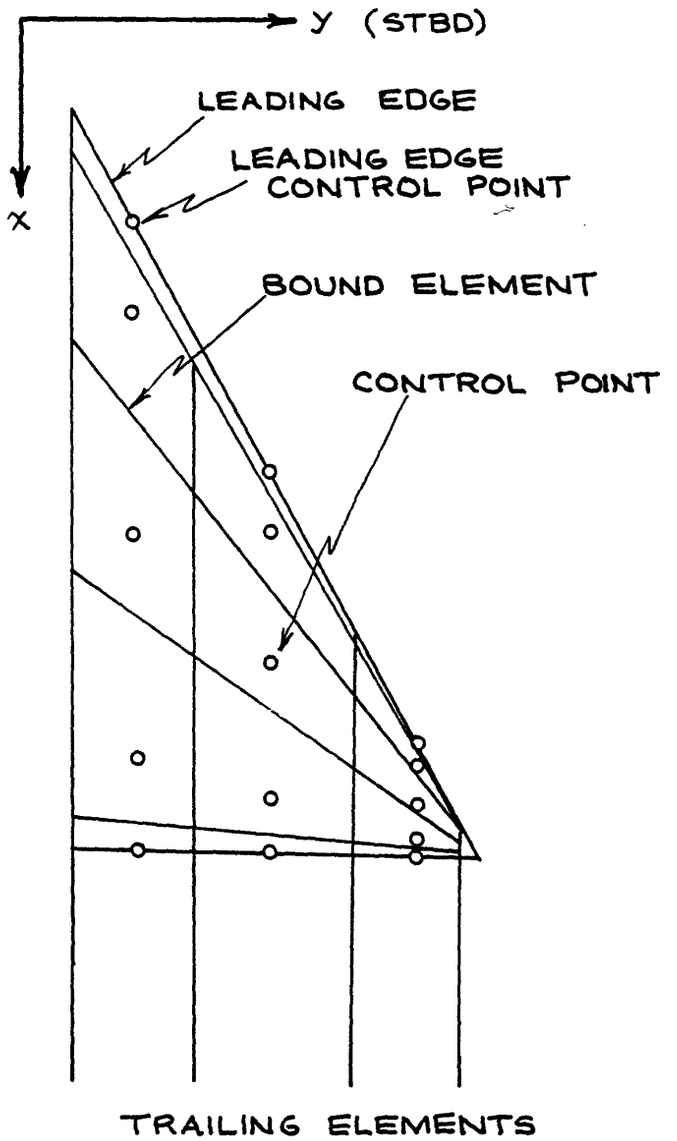

(From Mehrotra & Lan, 1978)

Figure 5.2.3 - Wing geometry without leading edge vortex system in Mehrotra & Lan model (1/2 of delta wing)

in matrix form as follows

$$A \cdot \Gamma = B \tag{5.2.2}$$

or

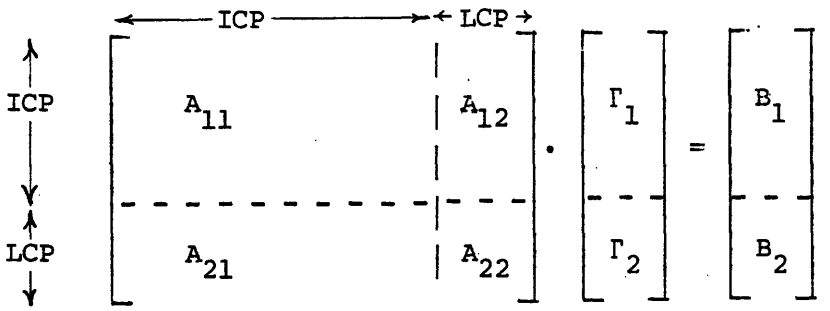

(5.2.3)

where

A = matrix of normal velocity influence coefficients (see Eq. 5.2.1)

A_{11} = submatrix expressing influence of regular horseshoes on regular control points

A_{12} = submatrix expressing influence of leading edge horseshoes on regular control points

A_{21} = submatrix expressing influence of regular horseshoes on leading edge control points

A_{22} = submatrix expressing influence of leading edge horseshoes on leading edge control points

Γ_1 = vector of regular horseshoe strengths

Γ_2 = vector of leading edge horseshoe strengths

B_1 = vector of the negative of the inflow velocity at the regular control points

B_2 = vector of desired induced velocities at the leading edge control points

ICP = number of regular control points

LCP = number of leading edge control points

Note that solving the attached flow problem without leading edge separation present is equivalent to solving the matrix equation

$$A_{11} \cdot \Gamma_1 = B_1 \tag{5.2.4}$$

The leading edge horseshoe system is superimposed on the regular vortex lattice grid. A typical leading edge horseshoe is shown by points A through J in Figure 5.2.4, with the initial geometry shown by dashed lines and the final (force-free) geometry shown by solid lines. Points A through D lie along the usual trailing vortex wake, and segment D-E coincides with the chordwise legs of the usual horseshoes on the wing. Points E, F, G, and H lie in the wing plane. The location of segment E-F is ahead of the first bound (spanwise) vortex and is given by

$$x_E = x_{1_E} + \frac{c_E}{2}\left[1 - \cos\left(\frac{\pi/2}{N+1}\right)\right] \tag{5.2.5a}$$

$$x_F = x_{1_F} + \frac{c_F}{2}\left[1 - \cos\left(\frac{\pi/2}{N+1}\right)\right] \tag{5.2.5b}$$

where the subscripts E and F refer to the points under consideration. The segments F-G and G-H are of the same length. Segments H through J form part of the vortex sheet shed from the leading edge.

The iterative scheme used by Mehrotra and Lan to solve the nonlinear boundary value problem is essentially identical to that used by Kandil, Mook, and Nayfeh (1976) and described above in part b). The calculated geometries of the vortex sheet shed from the leading

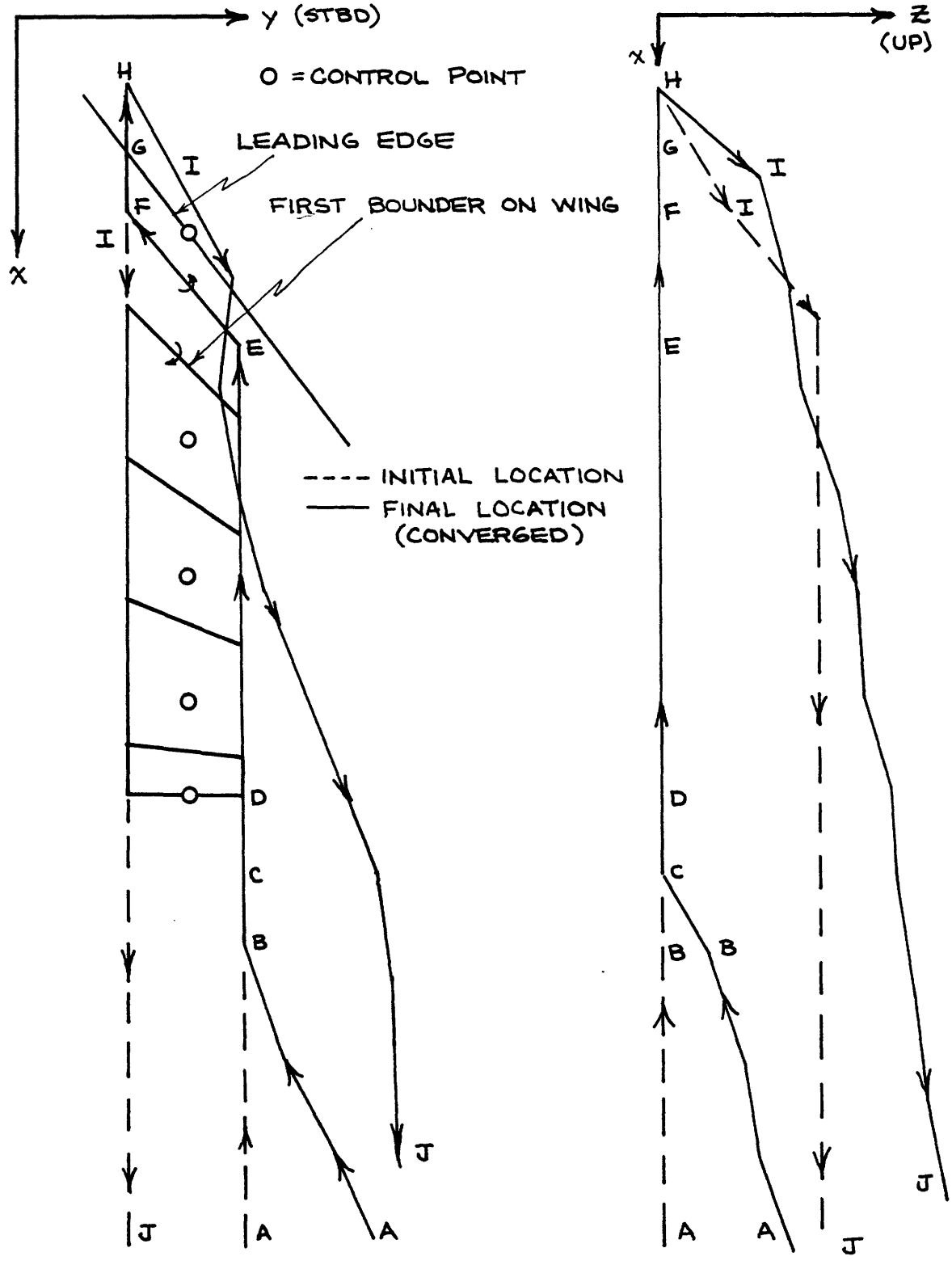

(From Mehrotra & Lan, 1978)

Figure 5.2.4 - Typical leading edge horseshoe vortex in Mehrotra & Lan model

edge are very similar for the two methods (Fig. 5.2.2).

Both of the vortex lattice methods described here yield adequate results for the lift, pitching moment, and pressure distribution on sharp-edged delta wings at high angles of attack. The method of Mehrotra and Lan has the added advantage of being able to deal with only a partial loss of leading edge suction, as opposed to the complete loss implied by imposing a leading edge Kutta condition.

However, neither one of these methods works very well at low angles of attack. The major problem is that the calculation of velocities at arbitrary points near the wing surface is required when lining up the segments of the leading edge vortex sheet with the flow. Unfortunately, the velocity field very close to the wing is grossly distorted because of the use of line vortices to represent the vortex sheet in the wing. Just as the control points on the wing must be very carefully located to get the correct normal velocity on the wing due to the vortex sheet, great care must be taken in computing induced velocities at points near the wing. Another problem with the vortex lattice methods described here is that at low angles of attack the vortices representing the leading edge vortex sheet may interact strongly with each other and either orbit around each other or attempt to force one of the vortices to pass through the wing surface. Many checks must be built into the free sheet alignment algorithm to make sure that such chaos does not occur. As a result, there may be many cases where the free sheet alignment algorithm fails to converge to a reasonable solution, or indeed, fails to converge at all.

5.3 Separated Tip Flow Model

Because the shed vorticity from the leading edge tends to remain as a vortex sheet for the operating conditions of interest (operation near design J), an attempt was made to use a model for the shed vorticity which represents a vortex sheet rather than a tightly rolled up vortex core. This was done by placing a replica of the vortex lattice used to represent the blade tip at a small distance above the suction surface of the blade (dashed lines in Fig. 5.3.1). This auxiliary lattice is a discretized representation of the leading edge vortex sheet. Vorticity "enters" this free sheet lattice through short segments connecting the free sheet lattice to the leading edge blade lattice. Instead of actually moving the vortex segments in the free sheet laterally to render them force-free, the vorticity is shunted back and forth between the segments of the free sheet lattice as the vorticity moves downstream so that the resulting vorticity vector at each node parallels as closely as possible the velocity vector at that node. This is referred to as lateral vorticity movement, and is discussed in detail in Appendix G. The height of the free sheet lattice may also be varied, as discussed in Section 5.4.

All calculations of induced velocities on the free sheet are made at the free sheet "control points"; that is, where the control points would be if the the free sheet lattice were the blade lattice. These are the correct locations for calculating the influence of the free sheet on itself. These are also the optimum locations for calculating

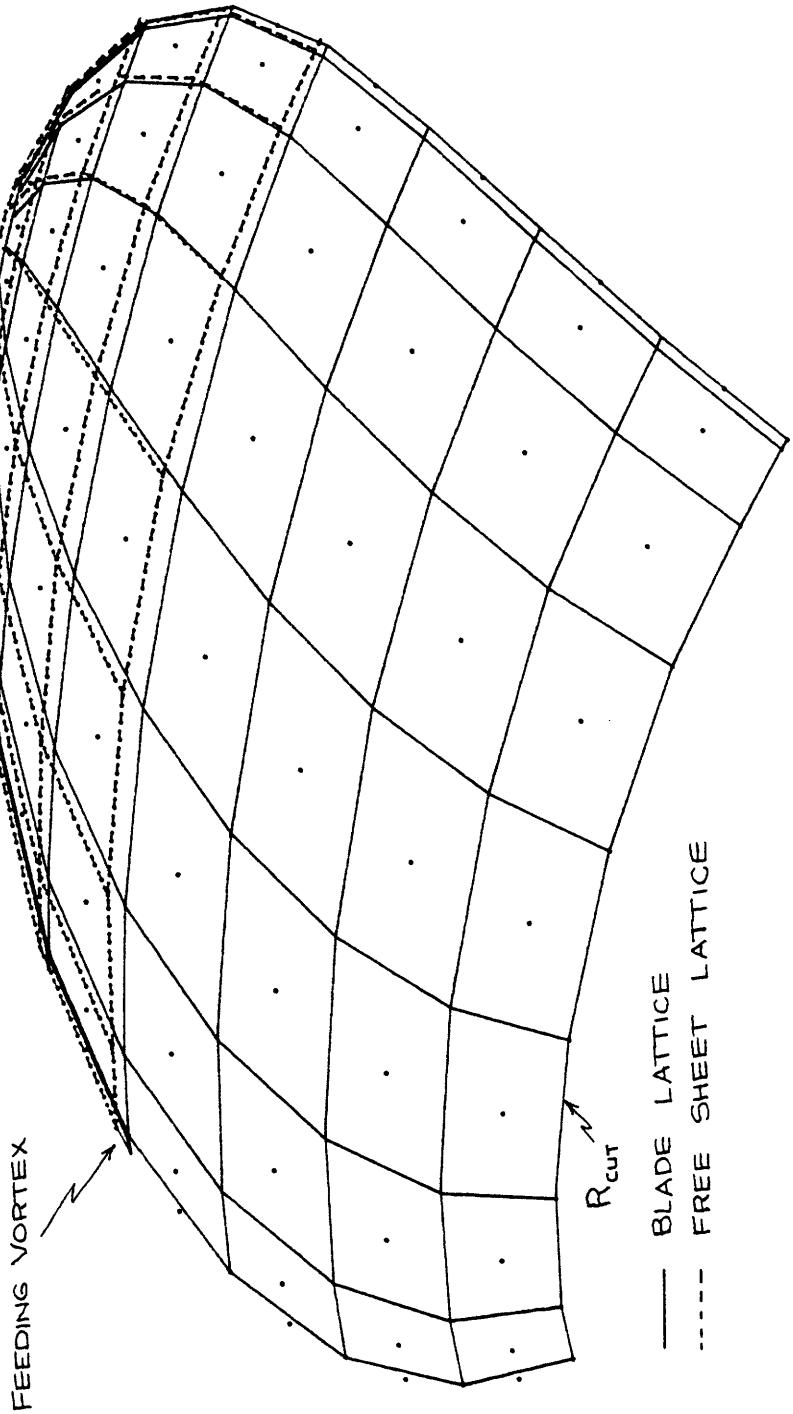

Figure 5.3.1 - Free vortex sheet lattice arrangement

the induced velocity due to the blade. The induced velocities at the free sheet nodes (required for directing the lateral vorticity movement) are obtained from the induced velocities at the free sheet "control points" by two-dimensional interpolation.

Using this discretized vortex sheet, the portion of a leading edge horseshoe representing part of the shed sheet no longer consists of a single line of short vortex segments passing over the blade surface, such as that shown in Fig. 5.2.4 (pg. 98). Instead, the free sheet portion of a leading edge horseshoe vortex consists of a number of spanwise and chordwise vortex segments in the free sheet, as shown in Fig. 5.3.2. The relative weights of the segments making up the horseshoe are assigned such that Kelvin's theorem (conservation of circulation) is satisfied at each node in the free sheet lattice, and so that the equivalent single vortex line (Fig. 5.3.2) is aligned as closely as possible with the local vorticity vector along its length.

Aside from the novel approach used to represent the shed vortex sheet, the rest of procedure was very similar to Mehrotra and Lan's (1978) method. Use was made of the capability for specifying an arbitrary leading edge suction force distribution, and the set of equations used to solve for the vortex strengths for an assumed vortex system geometry was identical to that given by Eq. 5.2.3.

It was hoped that the numerical problems encountered at low angles of attack when using a vortex lattice approach such as those discussed in Section 5.2 would be circumvented by this representation of the

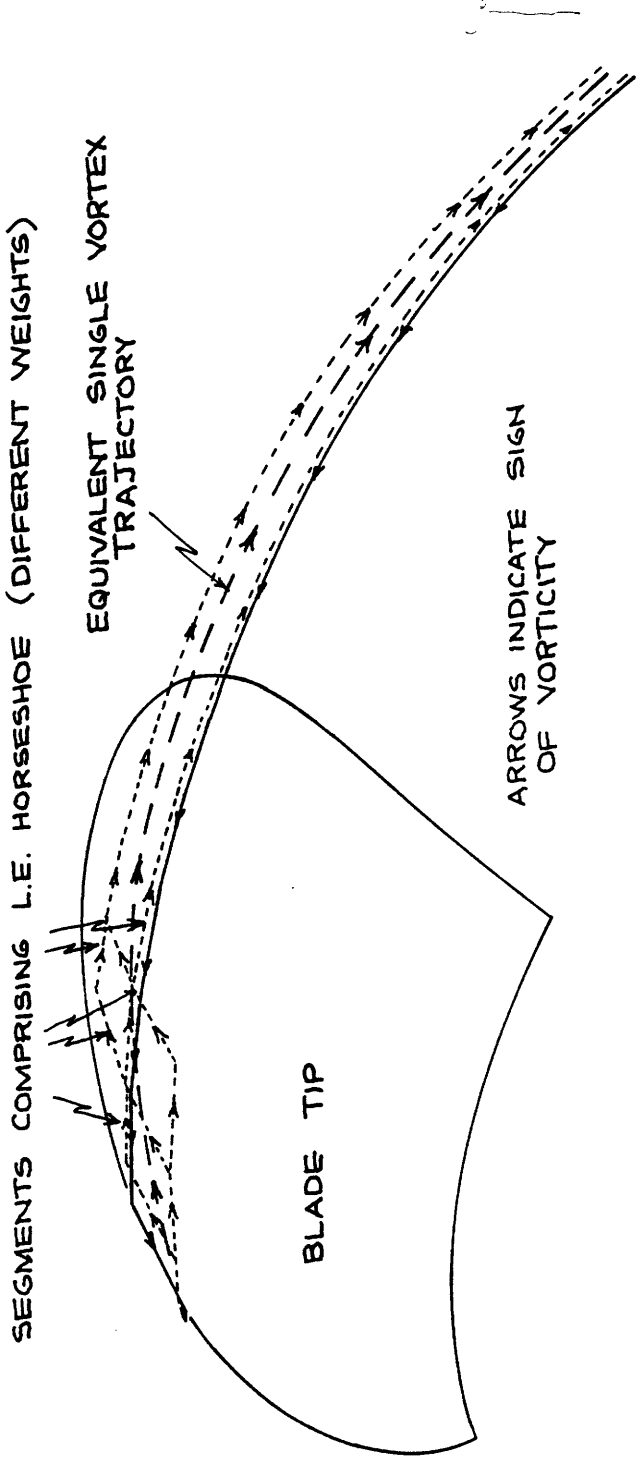

Figure 5.3.2 - Typical leading edge horseshoe vortex

vortex sheet shed from the leading edge of the blade. However, this scheme did not work at all. The lateral vorticity movement algorithm described in Appendix G kept moving all of the shed vorticity to the inboard edge of the sheet, whereas in reality the shed vorticity tends to remain close to the leading and tip edges of the blade. In hindsight, this result was to be expected. The direction of the radial velocity above the suction side of the blade tip is inward in the whole tip region, and this is responsible for the tip vortex being displaced slightly inward from the extreme blade tip. It is the rolling-up of the leading edge vortex sheet which is responsible for the shed vorticity concentrating near the leading and tip edges of the blade. This may be seen by examining the flow near the leading edge of the blade, as shown in Fig. 5.3.3. It is the outward induced velocity on the inboard portion of the sheet caused by the outboard portion of the sheet that is responsible for the shed vorticity remaining near the leading edge. Also, a strong rolling up is associated with an axial flow along the vortex "core" that causes entrainment and further concentration of the vorticity, as pointed out by Mc Mahon (1967) and Cummings (1968).

Hence, although the rolling up of the free sheet at operation near design J is not expected to be dramatic, it appears that the modeling of the rolling up process is important in calculating the correct trajectory of the shed vorticity. The vortex lattice methods described in Section 5.2 do allow the free sheet to roll up (see Fig.

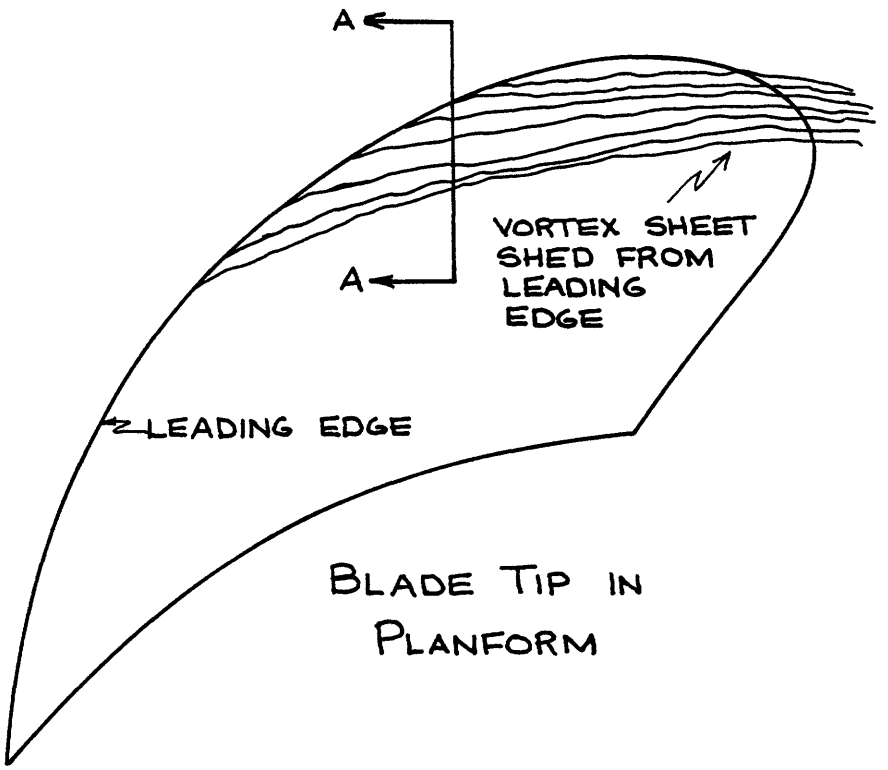

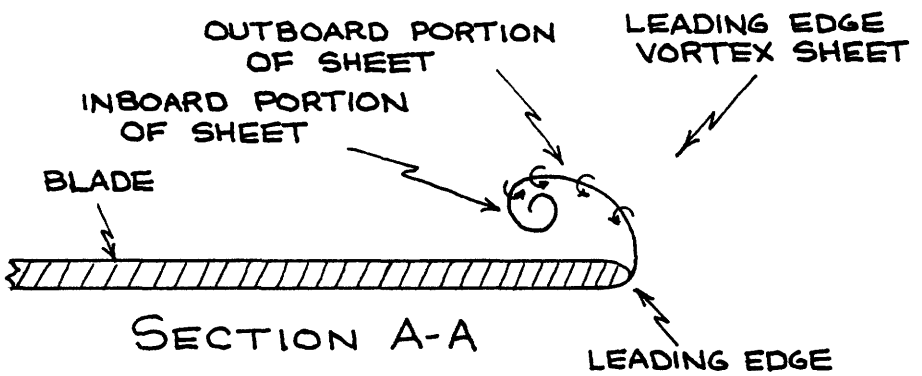

Figure 5.3.3 - Roll-up of leading edge vortex sheet

5.2.2, pg. 93) but as already pointed out these methods do not work well at low angles of attack because of the extremely close approach of the discretized sheet to the discretized blade.

Because the free sheet is so close to the blade surface for the operating conditions under consideration, the neglect of the no-slip boundary condition on the blade surface may be a serious omission. If this is true then no potential flow model, no matter how elaborate, will correctly predict the features of the real flow. In any event the disparate length scales involved in simultaneously modeling the free sheet roll up and the flow over the rest of the blade tip would cause problems in most potential flow modeling schemes.

Since the major interest in the current thesis lies in modeling the flow around the blade tip when the shed vorticity does not roll up too strongly, a "first order" free sheet model has been implemented. In this model of the sheet the free vorticity is shed from the leading edge and moves back over the blade in the chordwise direction only (no change in radius). The height of the free sheet above the blade camber surface is given by

Height above camber surface =

1/2 blade thickness + blade boundary layer thickness (5.3.1)

The resulting first order free sheet geometry is shown in Fig. 5.3.4.

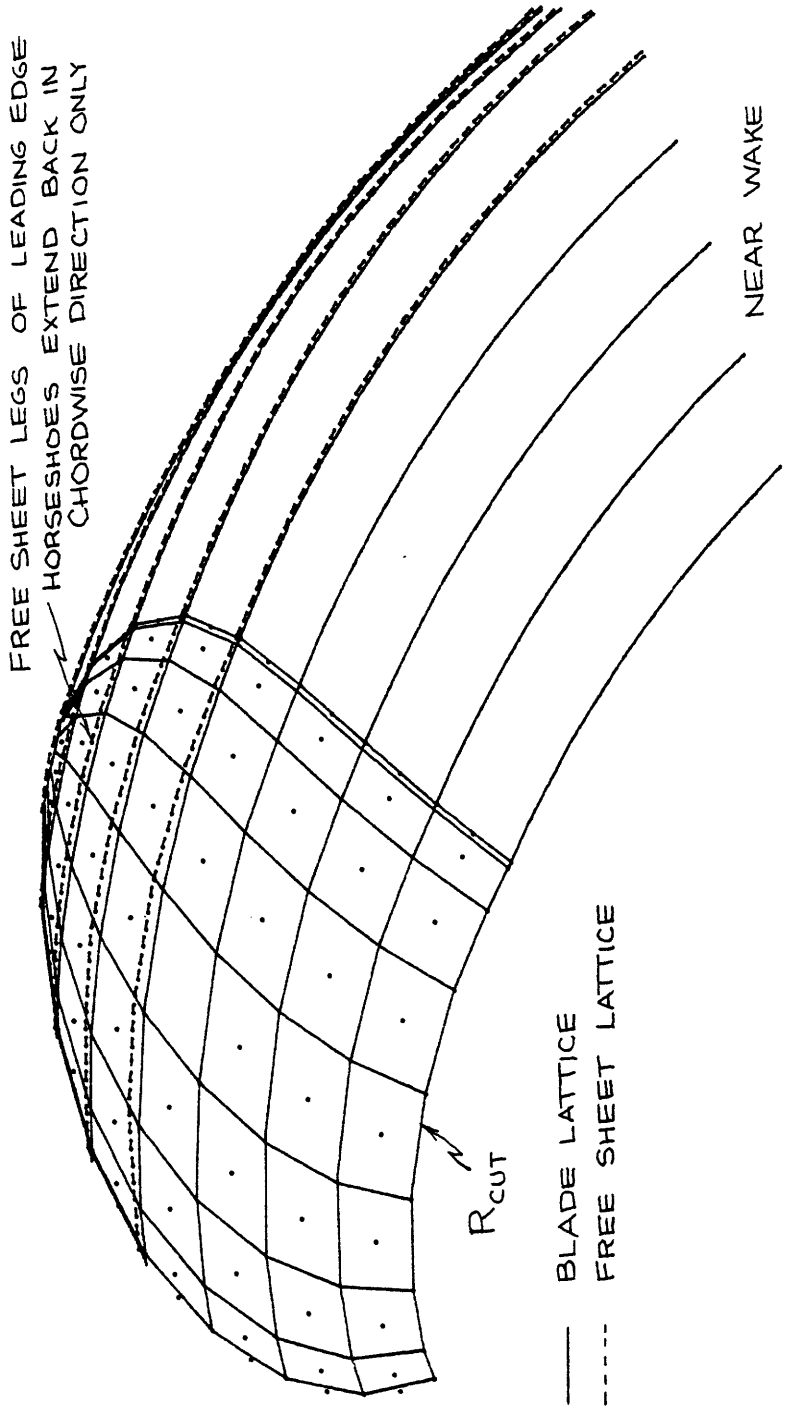

Figure 5.3.4 - First order model of leading edge vortex sheet

5.4 Tip Flow Solution Procedure

The complete procedure used to solve the boundary value problem for the flow around a propeller blade tip is outlined below. It is assumed that the global propeller analysis has already been completed and that a local tip flow domain has already been selected, as discussed in Sections 3.1 through 3.8.

a) A local tip flow solution using a fine vortex lattice is done, assuming no flow separation from the leading edge of the blade. This is discussed in Section 3.9.

b) Using the singularity distribution determined above, the normal velocities at the leading edge control points on the blade tip are calculated. As shown in Appendix A, this allows the leading edge suction force coefficient C_s to be determined along the leading edge.

c) Fig. 4.4.3 (pg. 83) is consulted to determine which portions of the leading edge have suffered leading edge flow breakdown. The assumption is made currently that vorticity is shed all along the leading edge outboard of the innermost separation point. This assumption appears to be valid for propellers having any kind of pitch distribution except for extreme unloading of the tip. For those sections of the blade predicted to have flow separation, the dashed line in Fig. 4.4.3 is used to estimate the residual leading edge suction force coefficient.

d) For each strip of the blade predicted to have leading edge flow separation, the required normal induced velocity at the leading edge control points is determined from the estimated residual leading edge suction force coefficient determined in c).

e) The "first order" model of the leading edge vortex sheet (Fig. 5.3.4) is set up covering all chordwise strips having leading edge separation. The height of the sheet is set by Eq. 5.3.1, using a simple two-dimensional zero pressure gradient turbulent boundary layer solution to estimate the blade boundary layer thickness (this is deemed sufficiently accurate for the current free sheet model). This first order free sheet model comprises the shed sheet legs of the leading edge horseshoes (Fig. 5.2.4).

f) The set of simultaneous equations (Eq. 5.2.3) is set up and solved to determine the strength of the blade vortex sheet and the shed vortex sheet. Since the free sheet geometry is not subsequently updated in an attempt to render it force free, this is in fact the final solution. No iteration is performed.

5.5 Determination of Blade Forces

The forces on the blade tip in the separated flow solution are calculated in a manner very similar to that used in the global solution and explained in Section 3.7. There are additional induced velocities due to the leading edge vortex sheet which must be included. The leading edge suction force for those portions of the leading edge experiencing flow separation is taken from Fig. 4.4.3.

VI. Numerical Results and Comparison With Experiments

6.1 Propeller Performance Analysis (Global Problem)

A series of computations were made to determine the accuracy of the propeller analysis procedure. For all of the computations described here the appropriate values of the ultimate wake radius (r_w), ultimate hub vortex radius (r_{wh}), and tip vortex contraction angle (δ_c) were determined from the experimental measurements of Min (1978). The two propellers described here are members of the NSRDC series of skewed propellers [Boswell (1971), Nelka (1974)]. Propeller 4381 is the unskewed parent propeller while propeller 4498 has 72 degrees of warp (72 degrees of midchord skew in the projected view, with the skew-induced rake removed). The design advance coefficient for both propellers is J = .889. A vortex lattice representation for 4381 is shown in Fig. 6.1.1, while 4498 is shown in Fig. 3.5.1 (pg. 43).

The importance of the correct trailing vortex wake pitch is illustrated in Fig. 6.1.2. The alignment of the wake with the flow is done using the algorithm described in Section 3.3 and Appendix B. Excellent agreement between measured and computed thrust is usually obtained if the wake geometry is correctly aligned with the flow, even at very low J values.

The influence of different grid arrangements on the predicted performance of 4381 is shown in Table 6.1.1. For each lattice arrangement the first number refers to the spanwise number of panels on the key blade, while the second gives the chordwise number of panels on

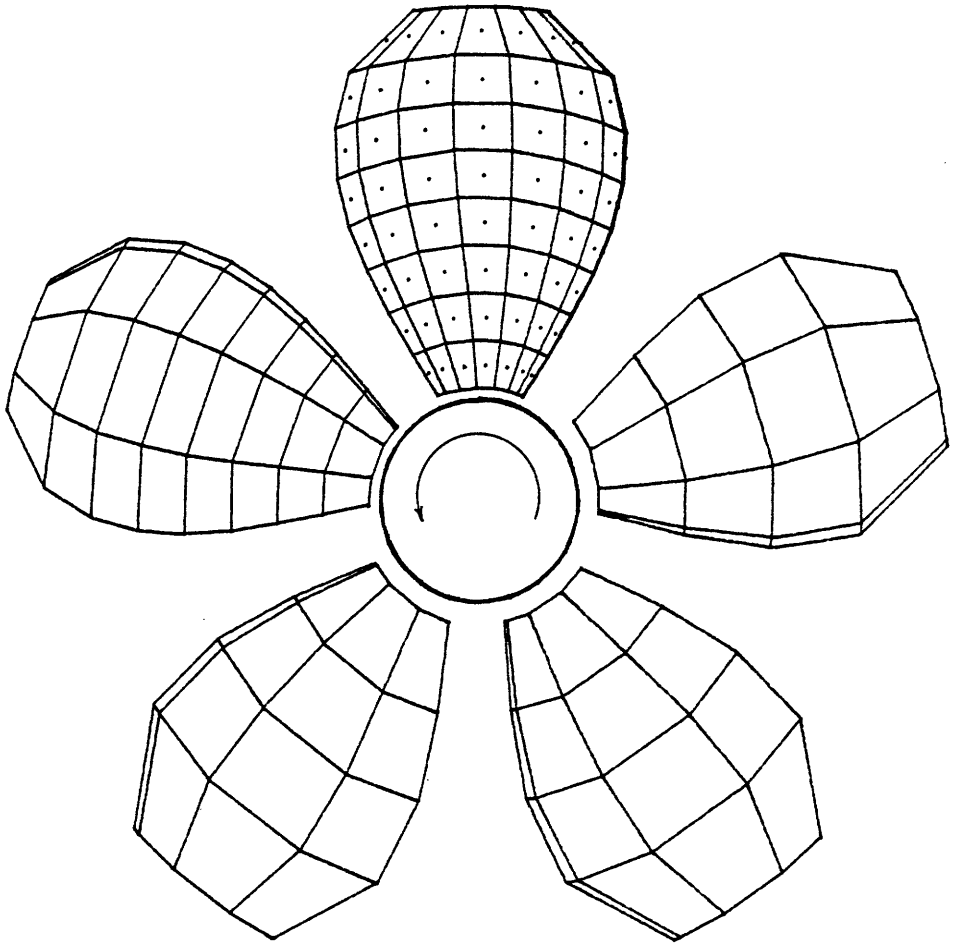

Figure 6.1.1 - Vortex lattice arrangement
for propeller 4381 (8 × 8 grid)

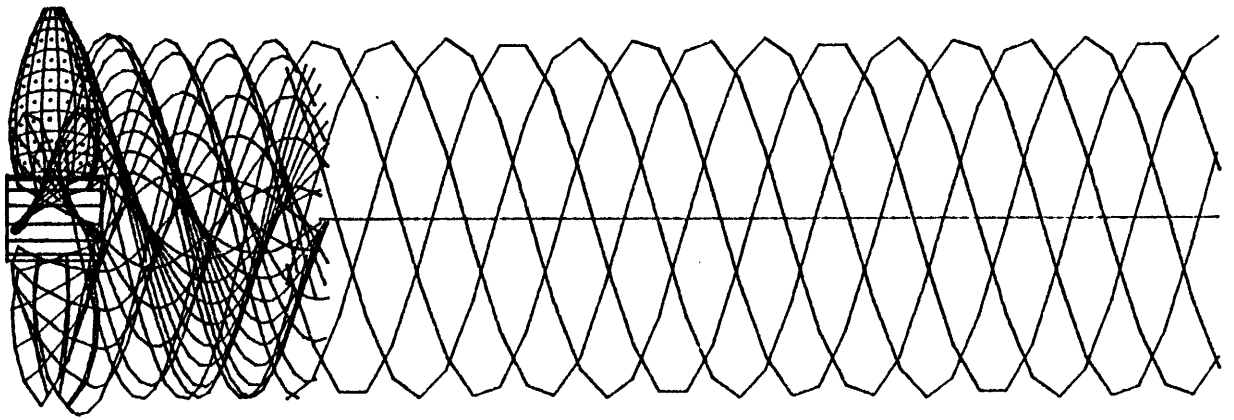

$\beta_w = \beta$ (LINEAR THEORY) PREDICTED $K_T = .3222$

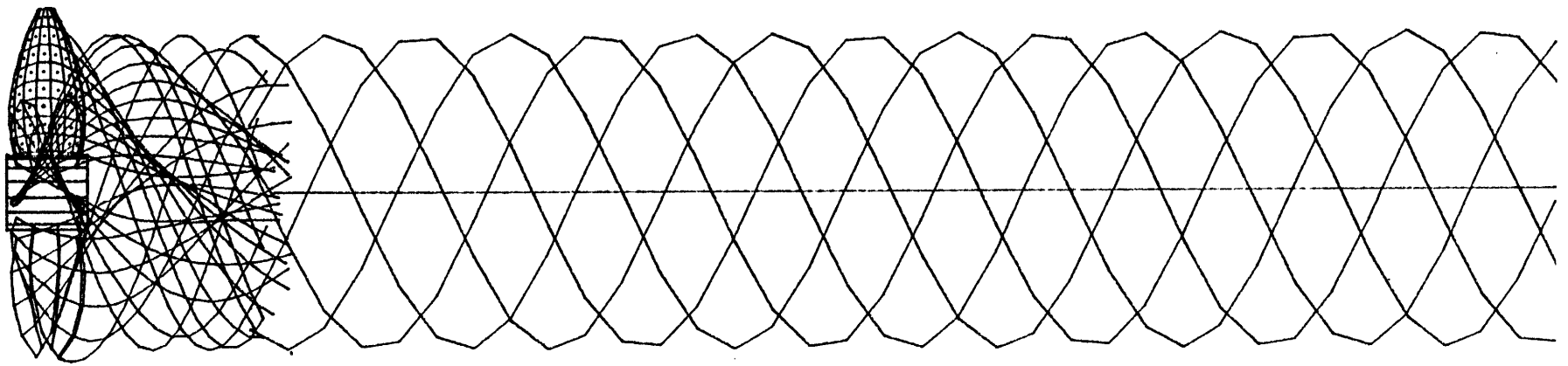

WAKE ALIGNED WITH FLOW. PREDICTED $K_T = .3406$, MEASURED $K_T = .340$

Figure 6.1.2 - Effect of wake geometry on predicted thrust

the key blade. For these and all other computations shown here the blade section viscous drag coefficient was taken to be 0.007.

Table 6.1.1

Effect of Lattice Arrangement on Predicted Performance of 4381, J = .889

Lattice	K_T	K_Q	η
8 × 8	.2048	.04196	.691
12 × 8	.2049	.04196	.691
8 × 12	.2055	.04161	.699
12 × 12	.2054	.04160	.699

Since these results are quite close and the 8 × 8 grid is much less expensive to use than the others, and 8 × 8 grid is used for most routine calculations.

Measured and computed open-water characteristics for propellers 4381 and 4498 are shown in Figures 6.1.3 and 6.1.4. Agreement is seen to be satisfactory, considering the spread in the experimental results. The under-prediction of torque for 4498 (72° warped prop) may be related to the fact that swept vortex lattices under-predict the induced drag of swept-back wings, as noted by Kalman, Giesing, and Rodden (1970) and Tulinius et al (1972).

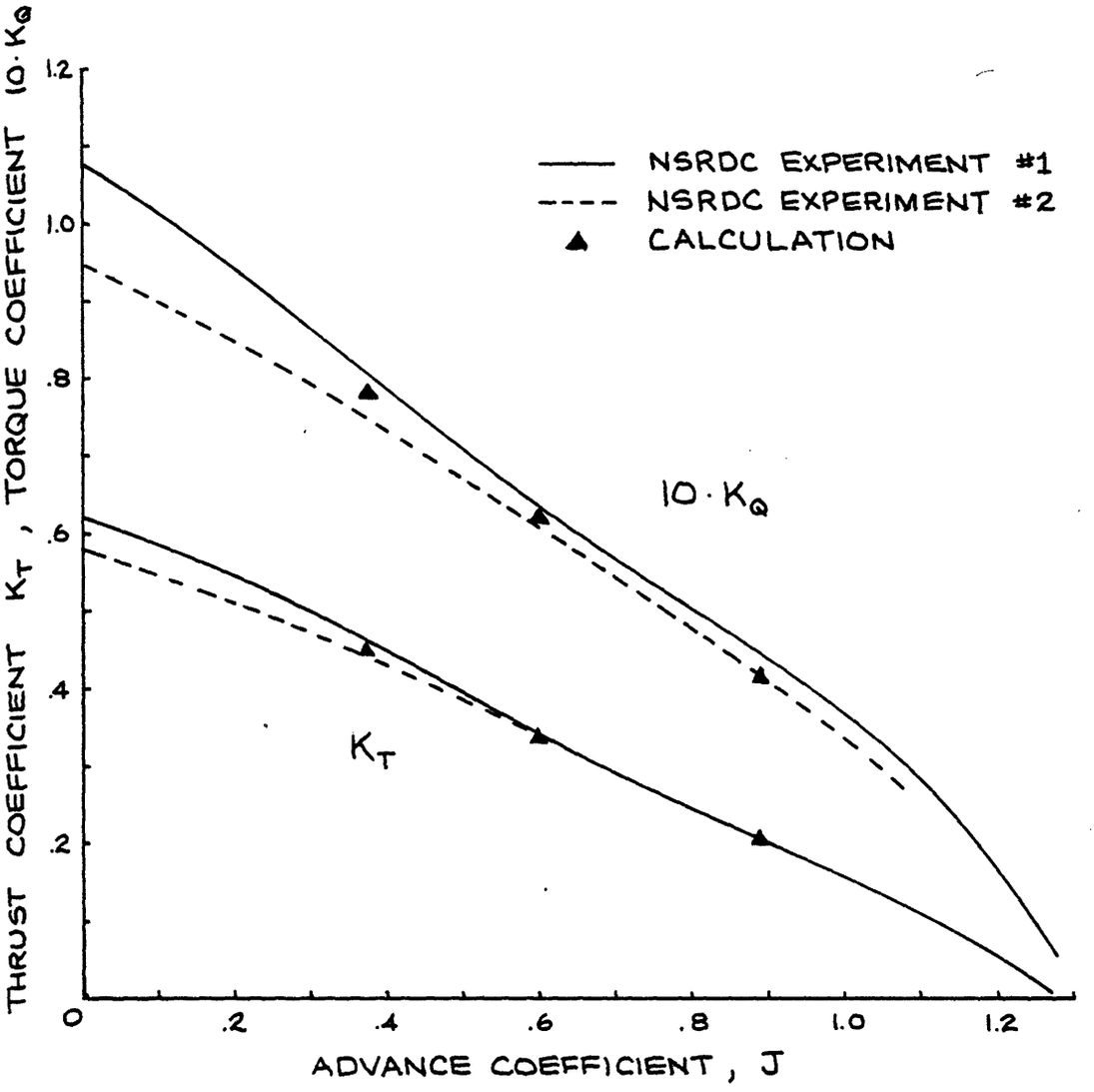

Figure 6.1.3 - Measured & calculated open water characteristics of NSRDC propeller 4381 (0° skew)

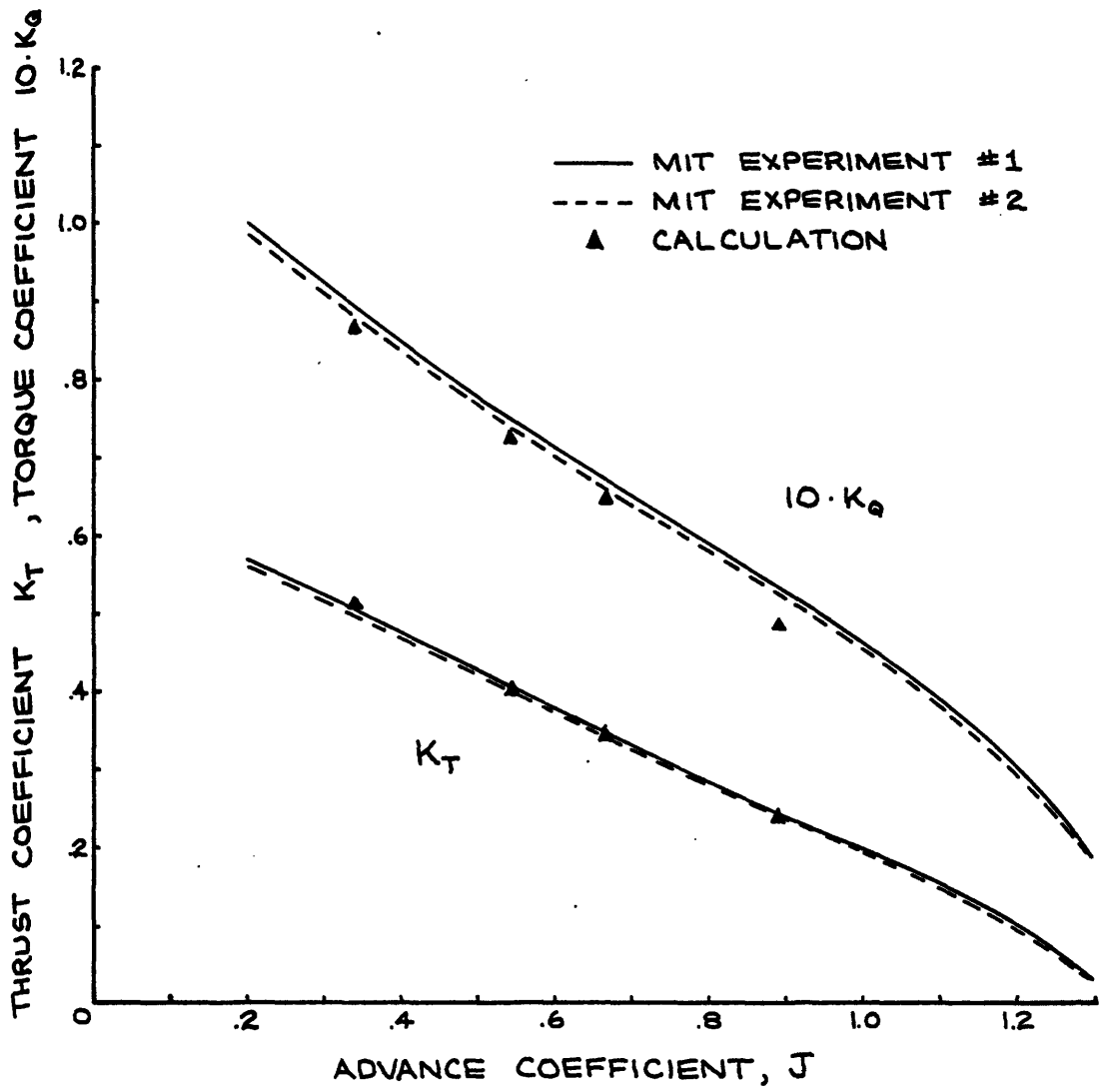

Figure 6.1.4 - Measured & calculated open water characteristics of NSRDC propeller 4498 (72° warp)

6.2 Attached Flow Tip Solution

The validity of the global-local problem separation was established by extensive numerical experimentation. Some typical results are presented here.

Fig. 6.2.1 shows the predicted bound circulation distribution for propeller 4498 operating at design J. The solid line is the bound circulation computed using an 8 × 8 grid in the global solution. The blade tip was "cut off" at r/R = .788 and several different lattice arrangements were used on the tip to solve the attached flow tip problem, yielding the results shown in Fig. 6.2.1. The circulation near the tip is artificially high in the global solution because of the large tip chord used in the global vortex lattice (compare Figs. 3.9.1 and 3.9.2, pg. 50). There is less discrepancy in the predicted forces and moments on the tip of the blade, as shown in Table 6.2.1. This may be due to the method of calculating blade forces, discussed in Section 3.7. It is assumed there that the average velocity over the length of a line singularity in the lattice is given by the velocity at its midpoint. Since the velocity gradients are large in the tip region, this assumption is only valid if short line singularities are used in the lattice, as in the tip solution. This appears to be responsible for the fact that the discrepancies between global and local solutions are not the same for circulation and forces.

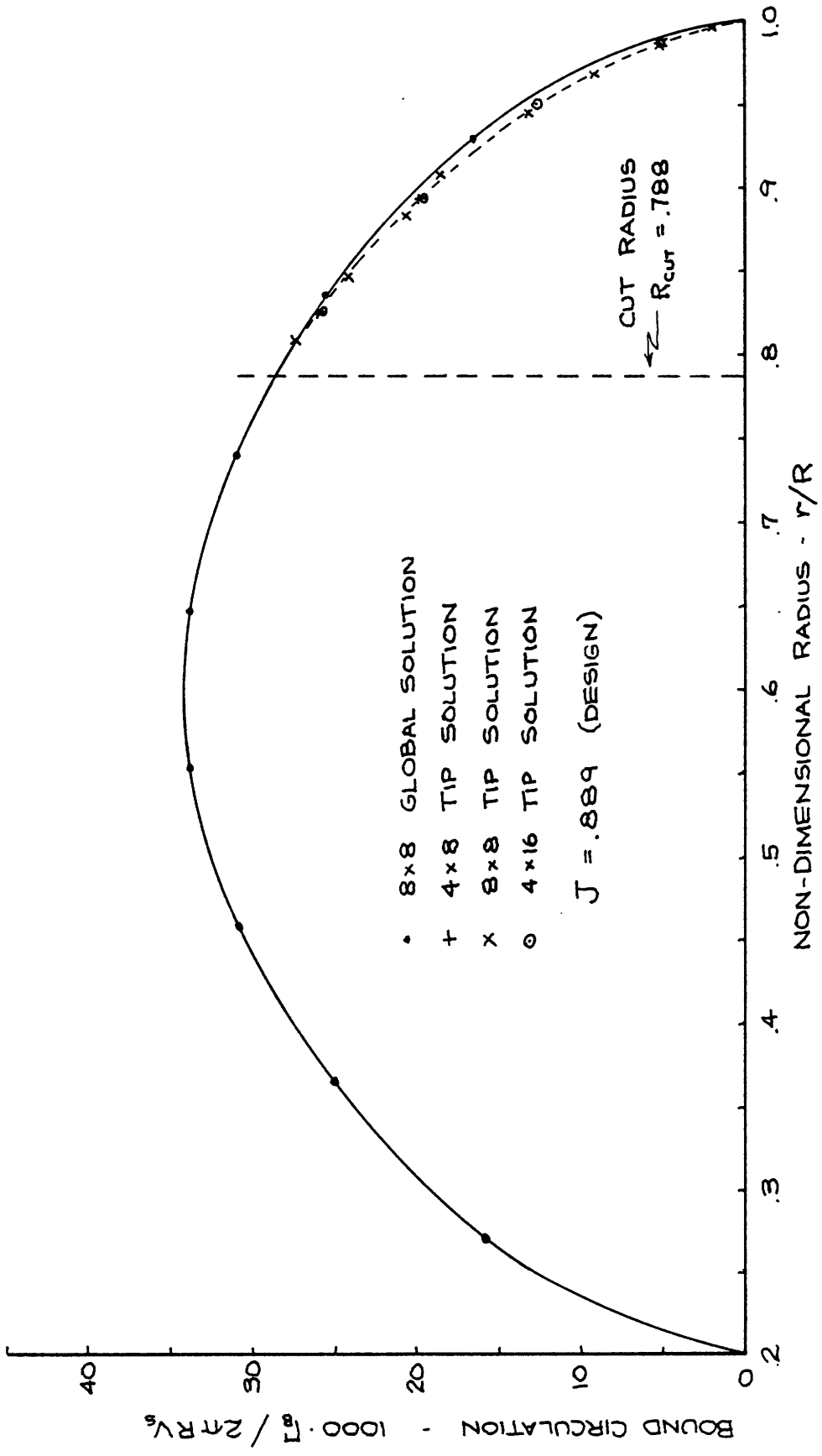

Figure 6.2.1 - Comparison of global and local solution bound circulation distributions for propeller 4498

Table 6.2.1

Predicted Forces & Moments on Tip of 4498 Blade Outboard of r/R = .788, Operating @ Design J = .889

SOLUTION	K_{F_x} (thrust)	K_{F_y}	K_{F_z}	K_{M_x} (torque)	K_{M_y}	K_{M_z}
Tip Portion of Global Solution	-.01556	-.01013	-.004456	.002905	-.005601	.003680
4 × 8 Tip	-.01591	-.01000	-.004423	.002856	-.005765	.003724
8 × 8 Tip	-.01581	-.00994	-.004363	.002846	-.005723	.003703
4 × 16 Tip	-.01579	-.00977	-.004374	.002814	-.005736	.003658
Rest of Blade Inboard of r/R = .788	-.03260	-.03539	.003769	.006831	-.005136	.007720

Figure 6.2.2 shows the predicted chordwise distribution of bound vorticity (proportional to the pressure jump across the blade) at r/R = .835 for the global and local solutions. Agreement is quite good.

These results indicate that the present technique of splitting up the problem is a viable method for obtaining a high resolution tip solution without the computational expense associated with a high resolution solution over the whole blade.

6.3 Prediction of Leading Edge Separation Point

Very little data is available for comparing predicted leading edge separation points with experimentally determined values. There is no full scale data available. Obtaining model scale data is limited by two factors:

a) Very few model propellers are available having accurately finished (and undamaged!) leading edges. The leading edge radius near the tip of a model propeller is only several thousandths of an inch.

b) The only technique currently available for leading edge flow visualization is to induce cavitation in the leading edge vortex. Unfortunately, there is only a limited range of operating conditions where other forms of cavitation (especially leading edge sheet cavitation) do not obscure leading edge vortex cavitation. This problem is especially severe at operation near design J, where the vorticity shed from the leading edge is weak.

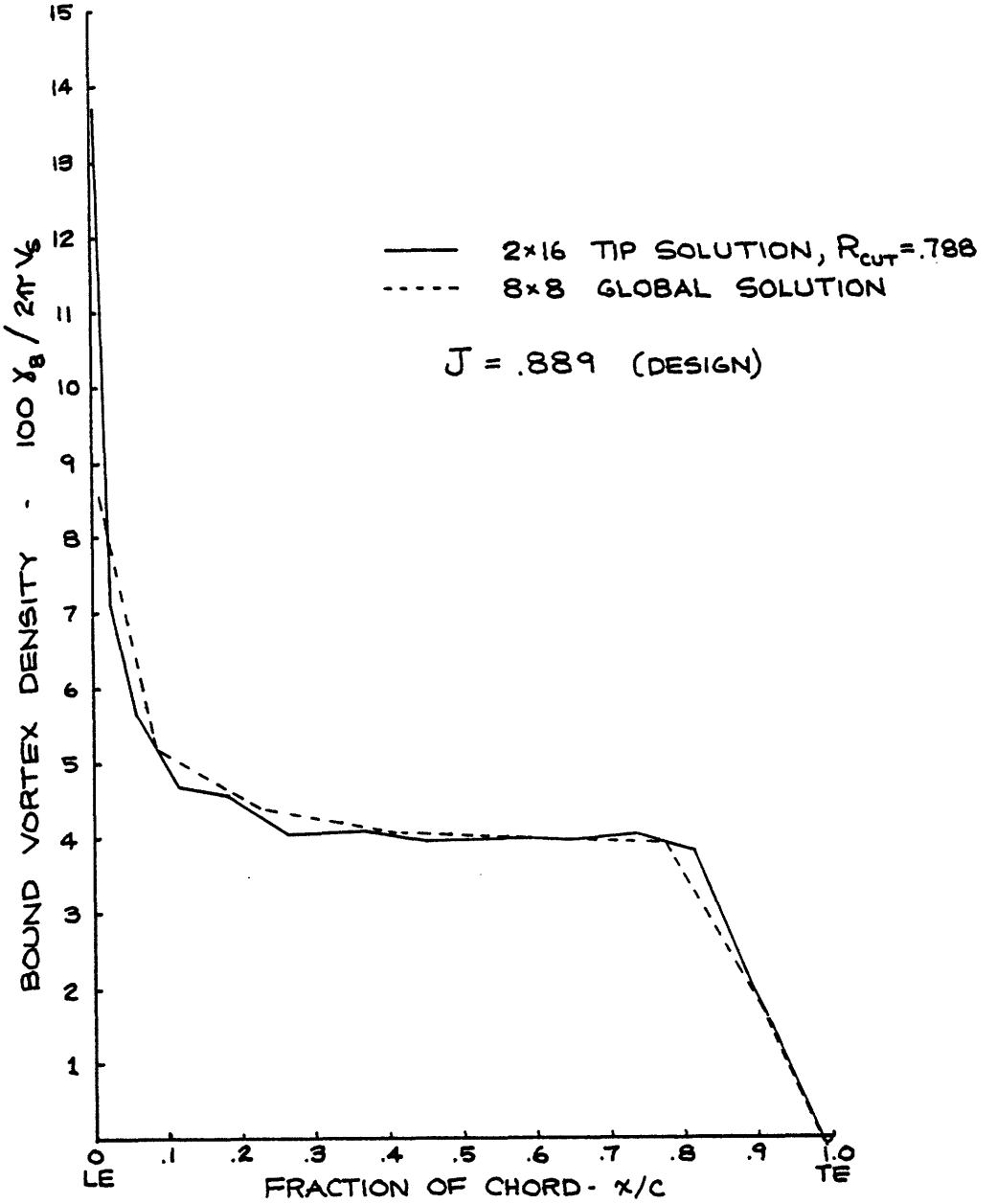

Figure 6.2.2 - Comparison of global and local solution chordwise loading distributions @ r/R = .835 for propeller 4498

The available data was taken in the MIT Variable Pressure Water Tunnel with two propellers: #4498, and #4119, which is a three-bladed unskewed constant pitch propeller designed for J = .833. (The global solution vortex lattice for 4119 is shown in Fig. 3.2.1, pg. 32). Fig. 6.3.1 shows the observed and calculated results. The vertical bar indicates the variability between different blades on the same propeller and the uncertainty involved in establishing the separation point from the cavitation patterns. Agreement is deemed to be satisfactory, but much more data is needed to validate the model.

The current viscous leading edge flow analysis qualitatively explains the observed phenomenon that skew delays the inception of leading edge sheet cavitation [Boswell (1971)]. Consider two propellers having the same chordlengths, section thicknesses, and load distribution; but let one be highly skewed and the other unskewed. The leading edge radius of the normal section (r_n) varies inversely with leading edge sweep angle Λ (Eq. E.2):

$$r_n \propto \frac{1}{\cos\Lambda} \tag{6.3.1}$$

and the component of the inflow velocity normal to the leading edge (U_n) varies as the cosine of the sweep angle Λ squared:

$$U_n \propto \cos^2 \Lambda \tag{6.3.2}$$

Hence the leading edge suction force coefficient C_s, defined by

$$C_s = \frac{F_s}{\frac{1}{2} \rho U_n^2 r_n} \tag{4.3.1}$$

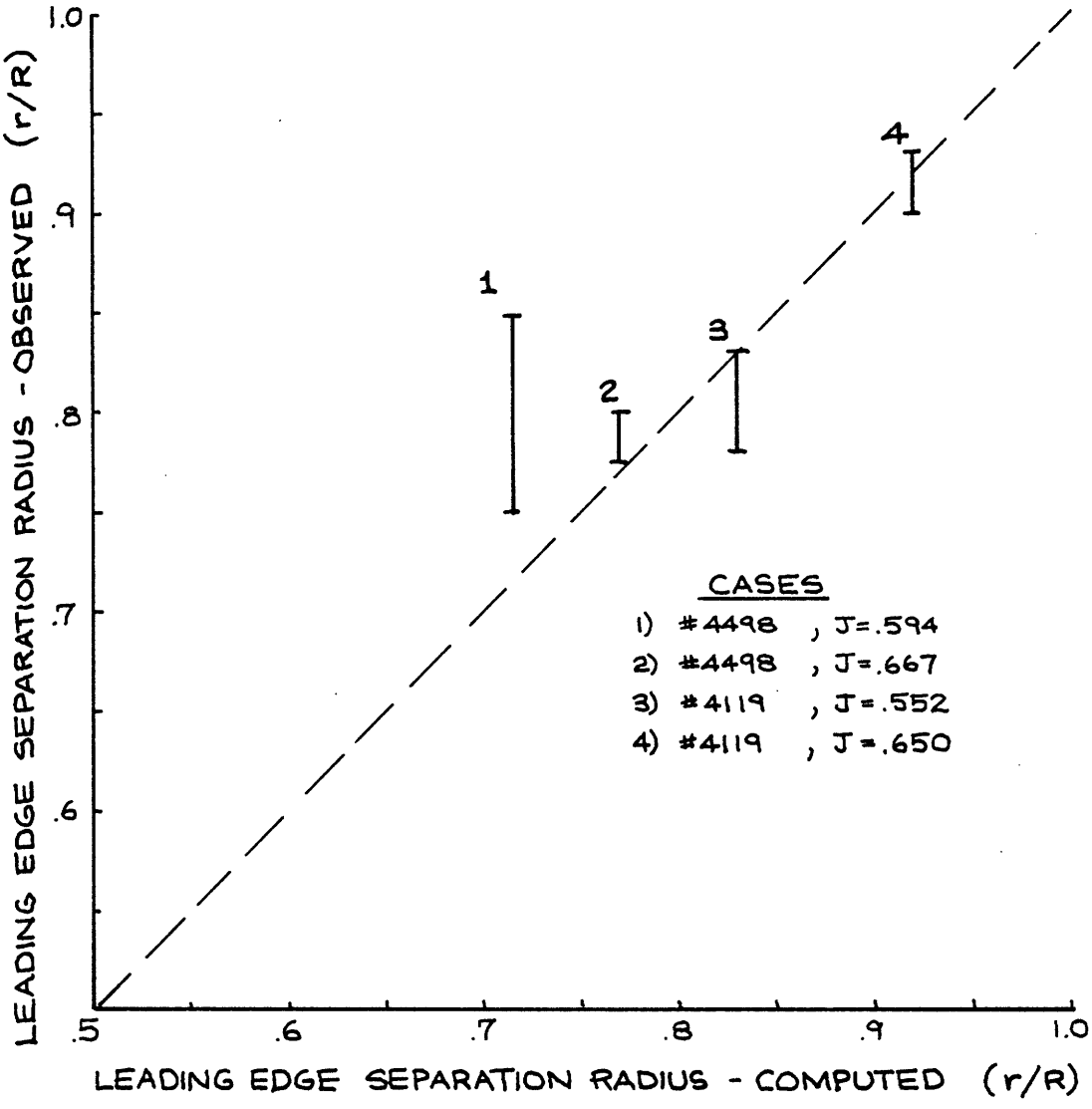

Figure 6.3.1 - Comparison of Calculated & Observed Leading Edge Separation Points

varies like

$$C_s \propto 1/\cos \Lambda \qquad (6.3.3)$$

for the two otherwise identical propellers. Similarly, the leading edge Reynolds number (Eq. 4.3.2) varies as

$$R_{le} \propto 1/\cos \Lambda \qquad (6.3.4)$$

Referring to Figure 4.4.3 (pg. 83), it can be seen that the propeller with the higher leading edge sweep Λ (the highly skewed propeller) will operate with its sections closer to the limiting suction force line in Fig. 4.4.3. So for a given J ($J < J_{design}$), the highly skewed propeller will have leading edge separation extending further inboard than on the unskewed propeller. Since the presence of leading edge separation knocks down the minimum pressure peak at the leading edge which is responsible for leading edge sheet cavitation, we may infer that the highly skewed propeller will be less susceptible to leading edge sheet cavitation than its unskewed partner, for a given loading and cavitation number. This phenomenon has been observed by Boswell (1971) and others.

Figure 4.4.3 also indicates that there may be significant Reynolds number ("scale") effects on leading edge cavitation inception. Arguments similar to those given above show that leading edge separation will occur to a greater extent on a model propeller than on its full scale geosim, as shown in Figures 6.3.2 and 6.3.3, when both are operating at the same advance coefficient. Leading edge sheet cavita-

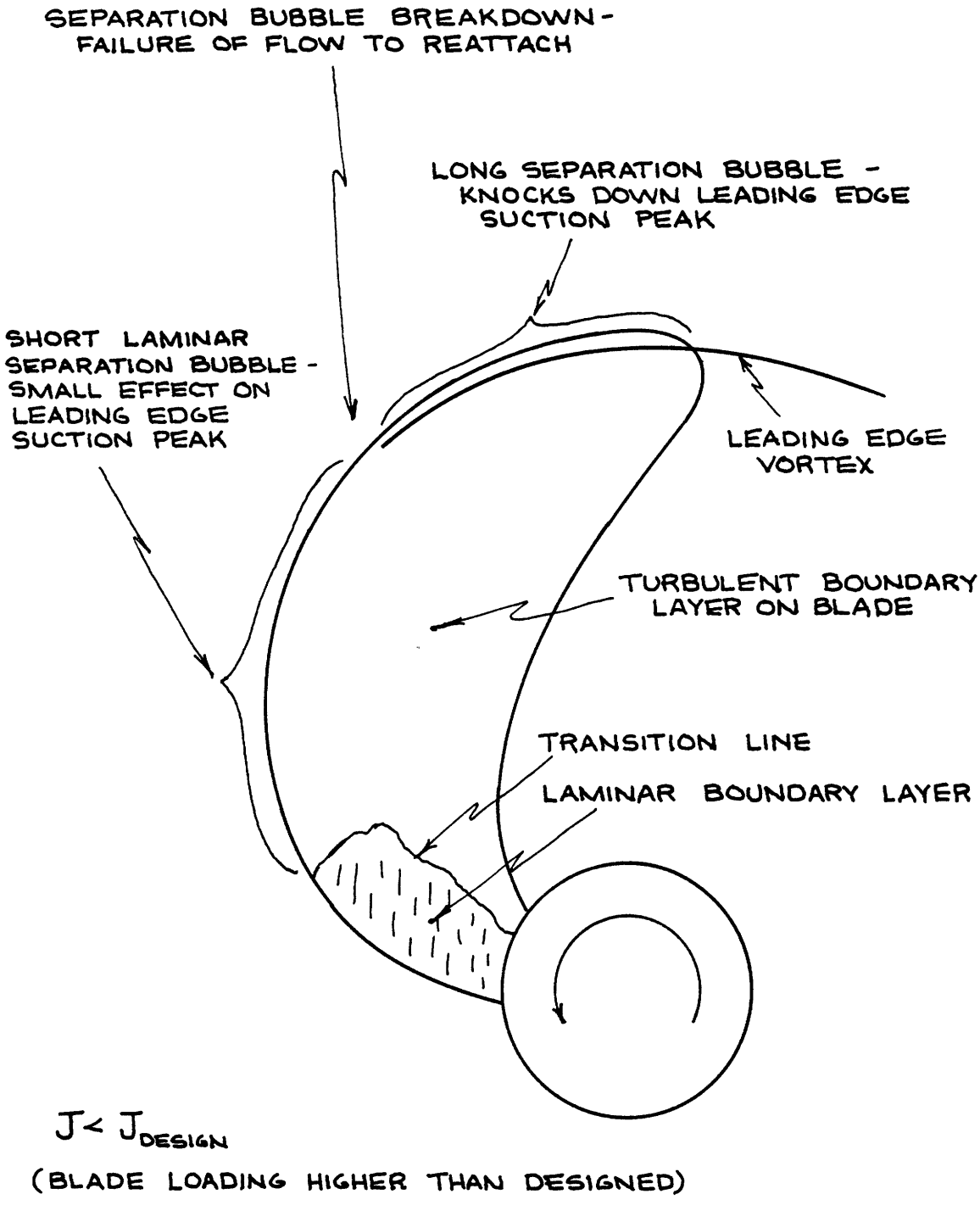

Figure 6.3.2 - Schematic of suction side flow on model propeller blade

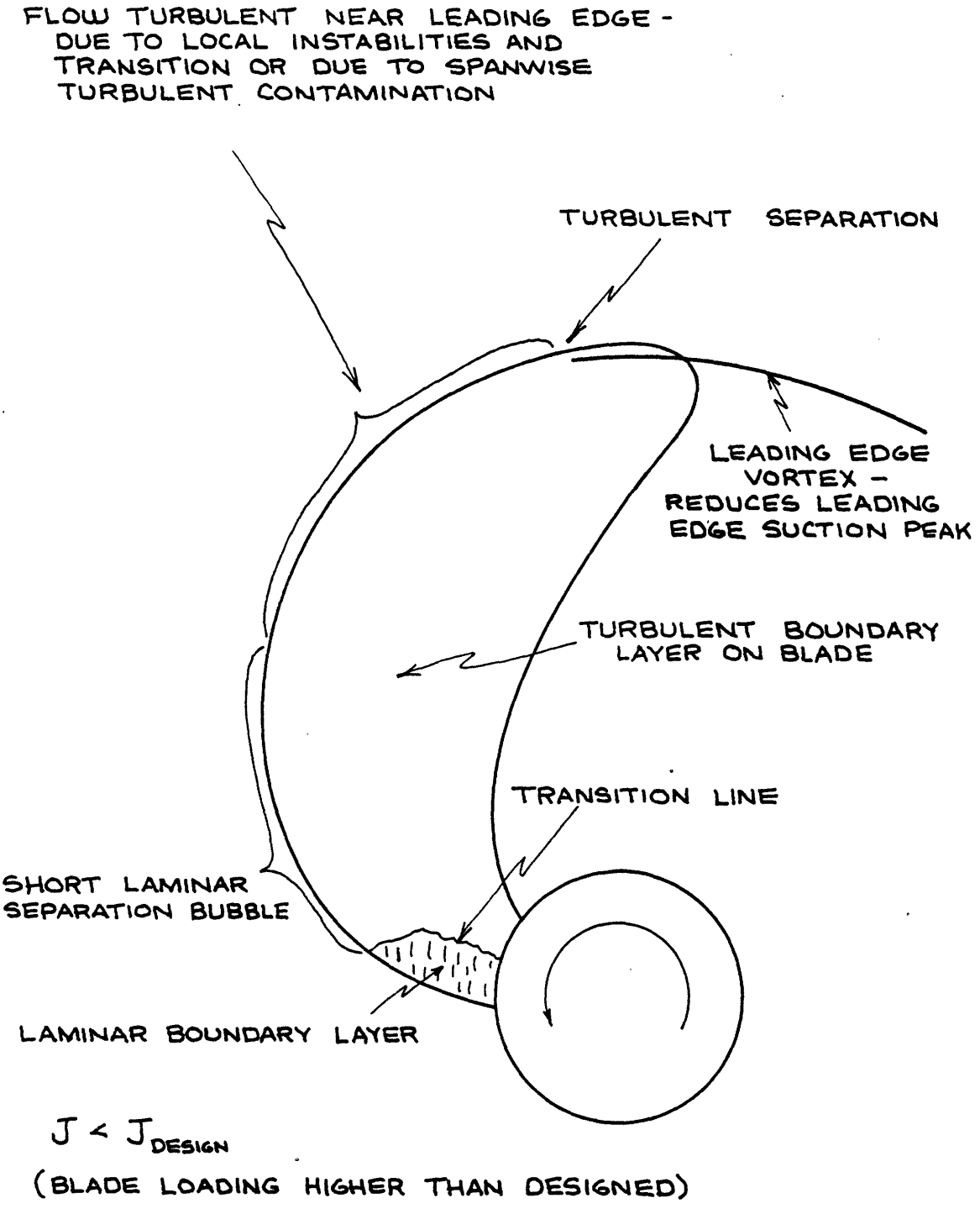

Figure 6.3.3 - Schematic of suction side flow on full-scale propeller blade

tion will be inhibited on the model propeller because of the greater extent of the leading edge where the minimum pressure peak has been reduced due to flow separation. This means that model tests should give optimistic predictions of full scale cavitation behavior, and indeed this often occurs.

6.4 Tip Solution Including Leading Edge Separation

A calculation was done using the theory outlined in Section 5.4 in order to predict the flow around the tip of the blade of propeller 4498, when operating at J = .800 (Design J = .899). At model scale, leading edge separation was predicted to occur outboard of r/R = .85. Fig. 6.4.1 shows the predicted bound circulation distributions, and it is seen that the presence of leading edge separation unloads the extreme tip of the blade and increases the loading inboard of the leading edge vortex sheet. Fig. 6.4.2 illustrates the predicted strength of the vortex sheet shed off of the leading edge.

Figures 6.4.3 through 6.4.10 show the computed chordwise load distributions at the radii at which calculations were performed. As expected, the major effect of the separated flow is to reduce the loading near the leading edge in the region where leading edge flow separation is expected to occur. The severe dip in the loading near the trailing edge at r/R = .993 (Fig. 6.4.10) is probably an anomoly due to the inadequate representation of the leading edge vortex sheet as it passes over the trailing edge of the tip.

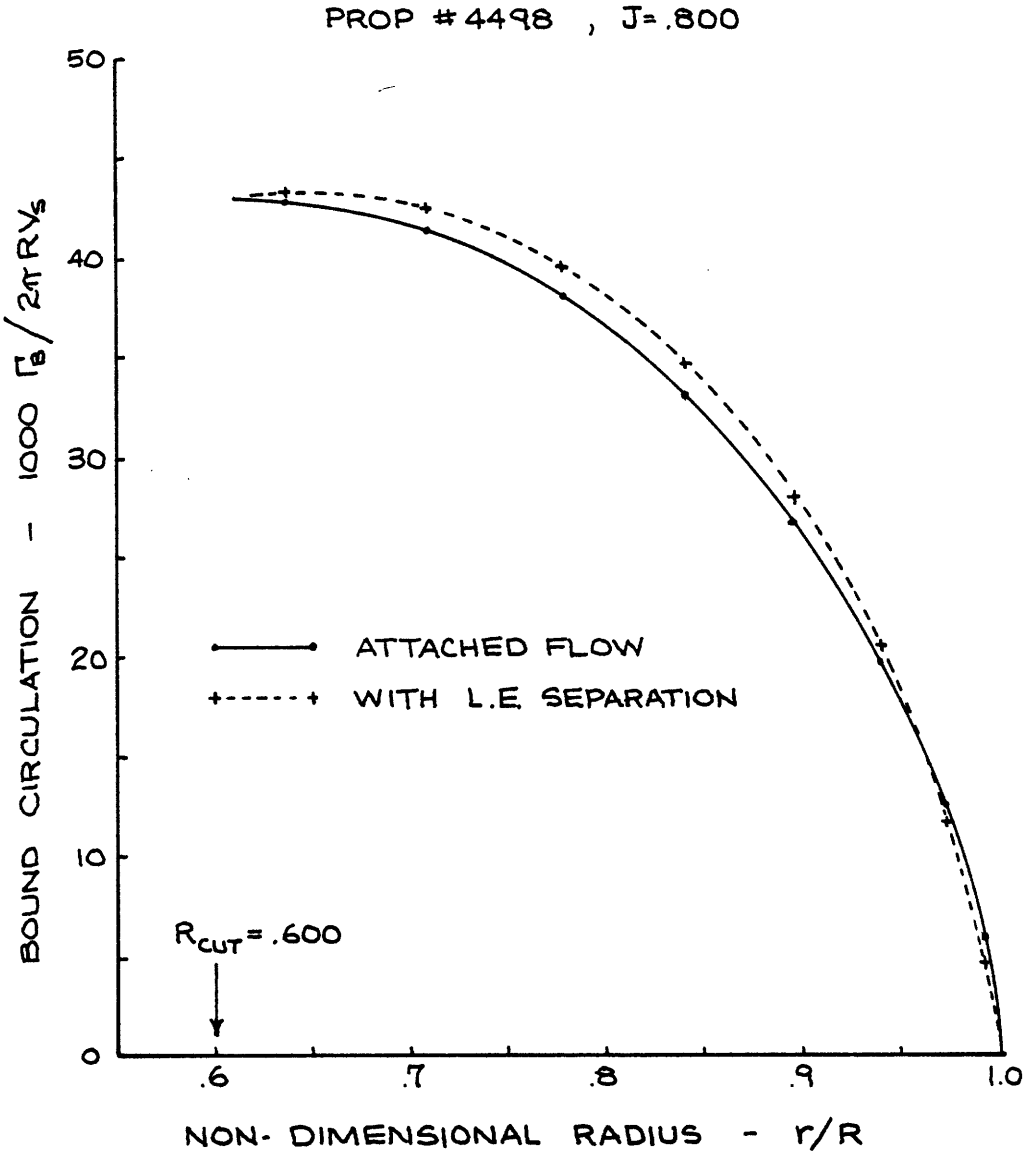

Figure 6.4.1 - Comparison of predicted bound circulation distributions for attached and separated flow

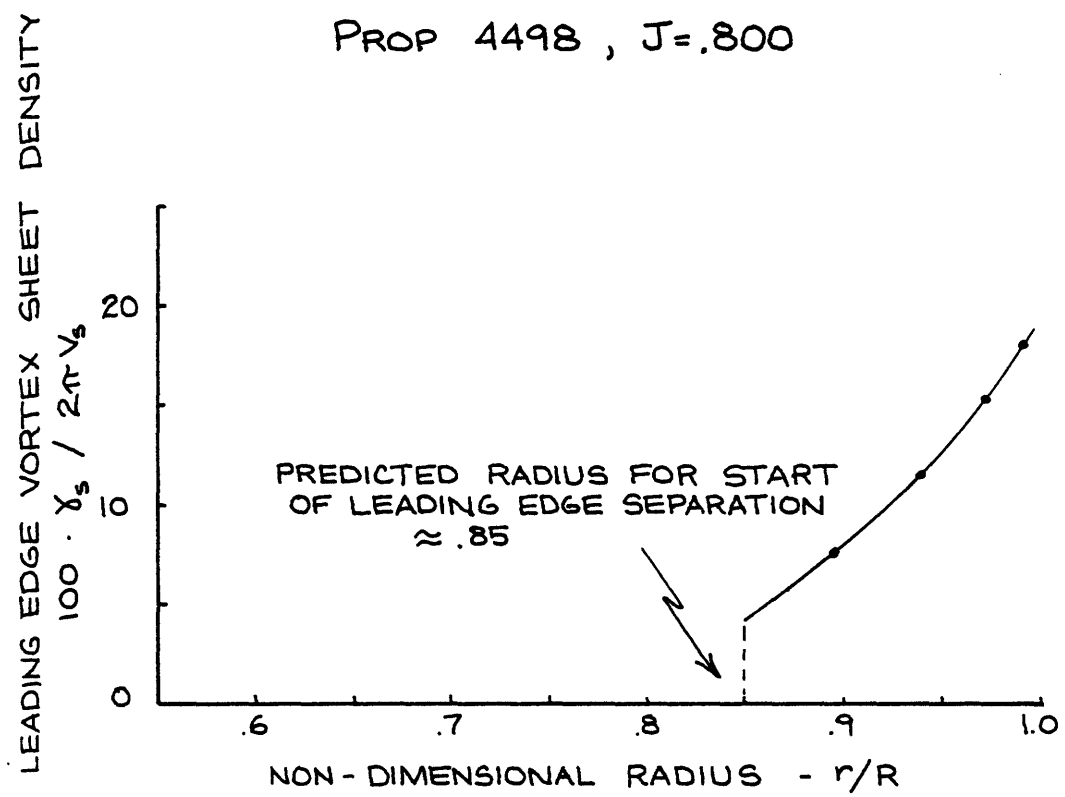

Figure 6.4.2 - Predicted strength of leading edge vortex sheet

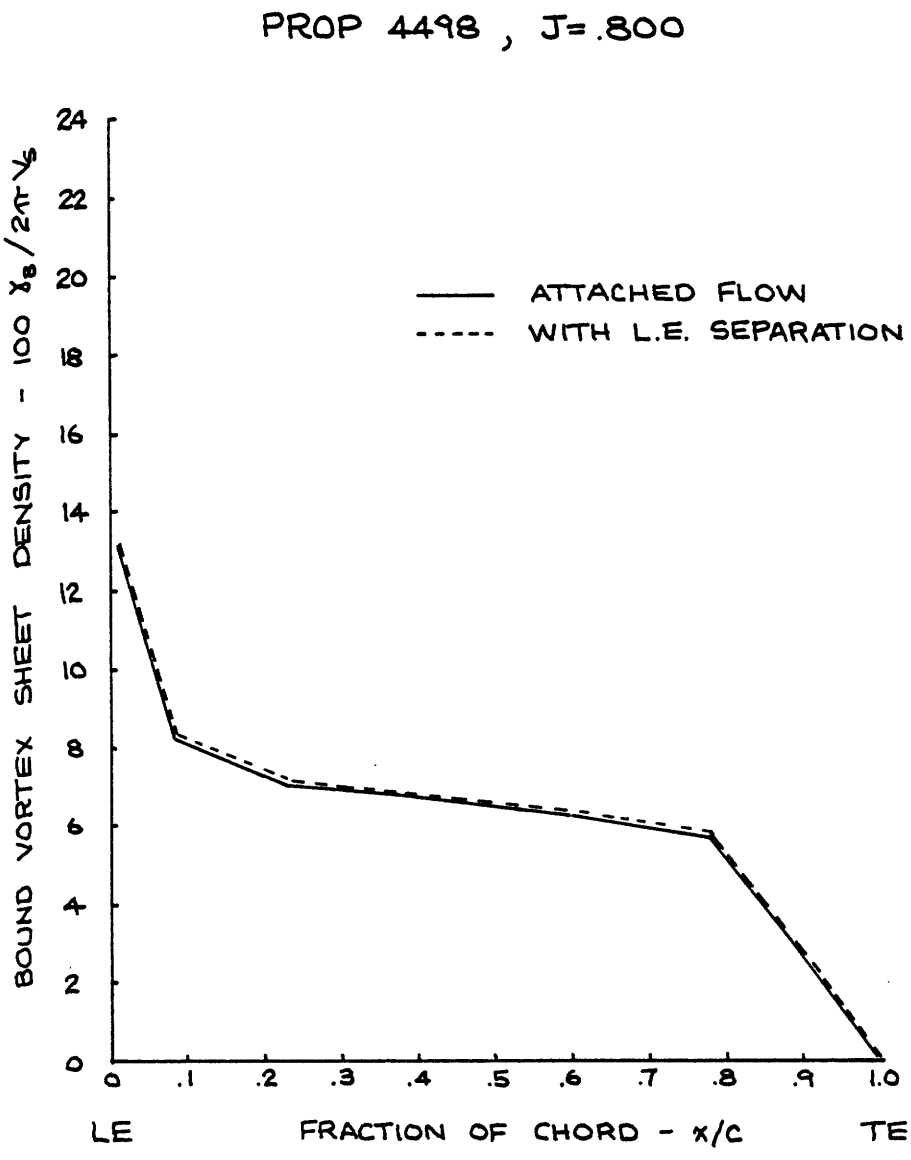

Figure 6.4.3 - Predicted chordwise loading
at r/R = .637

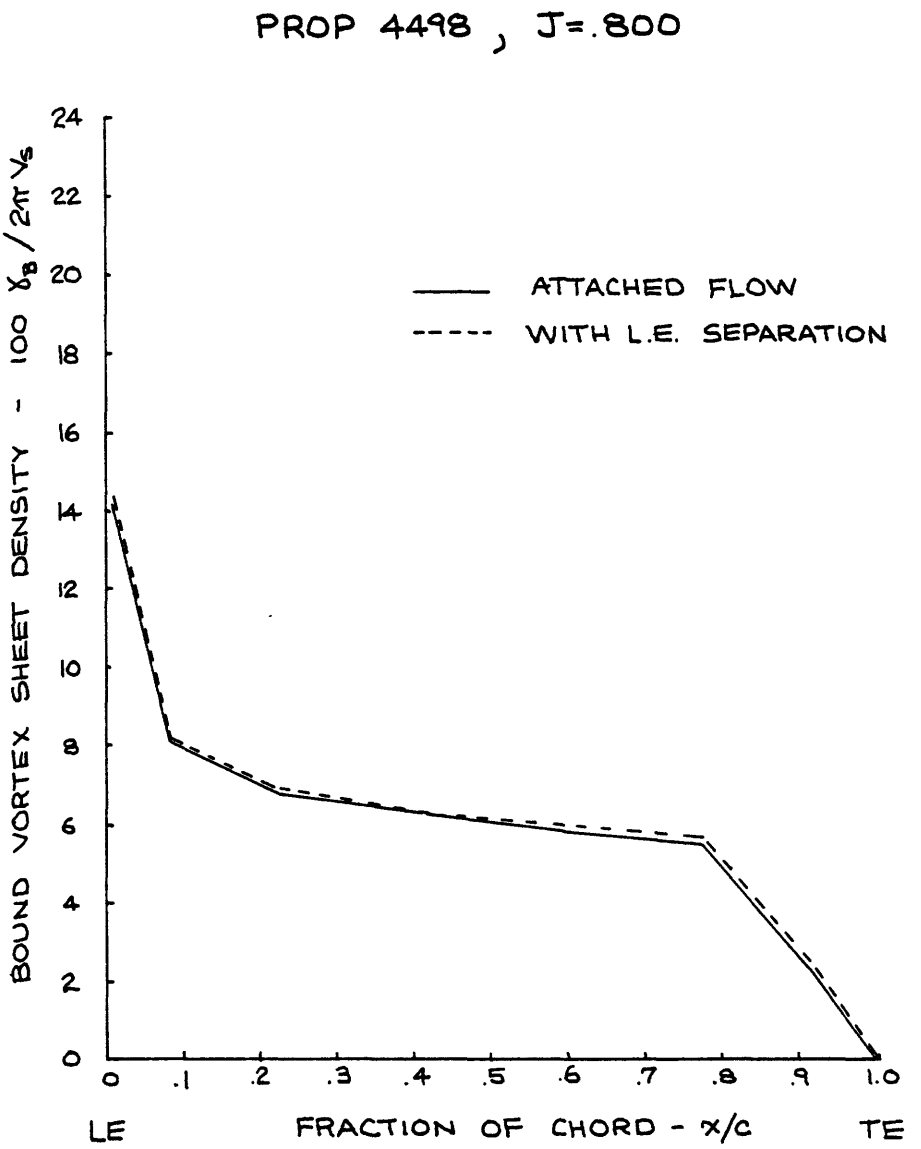

Figure 6.4.4 - Predicted chordwise loading
at r/R = .709

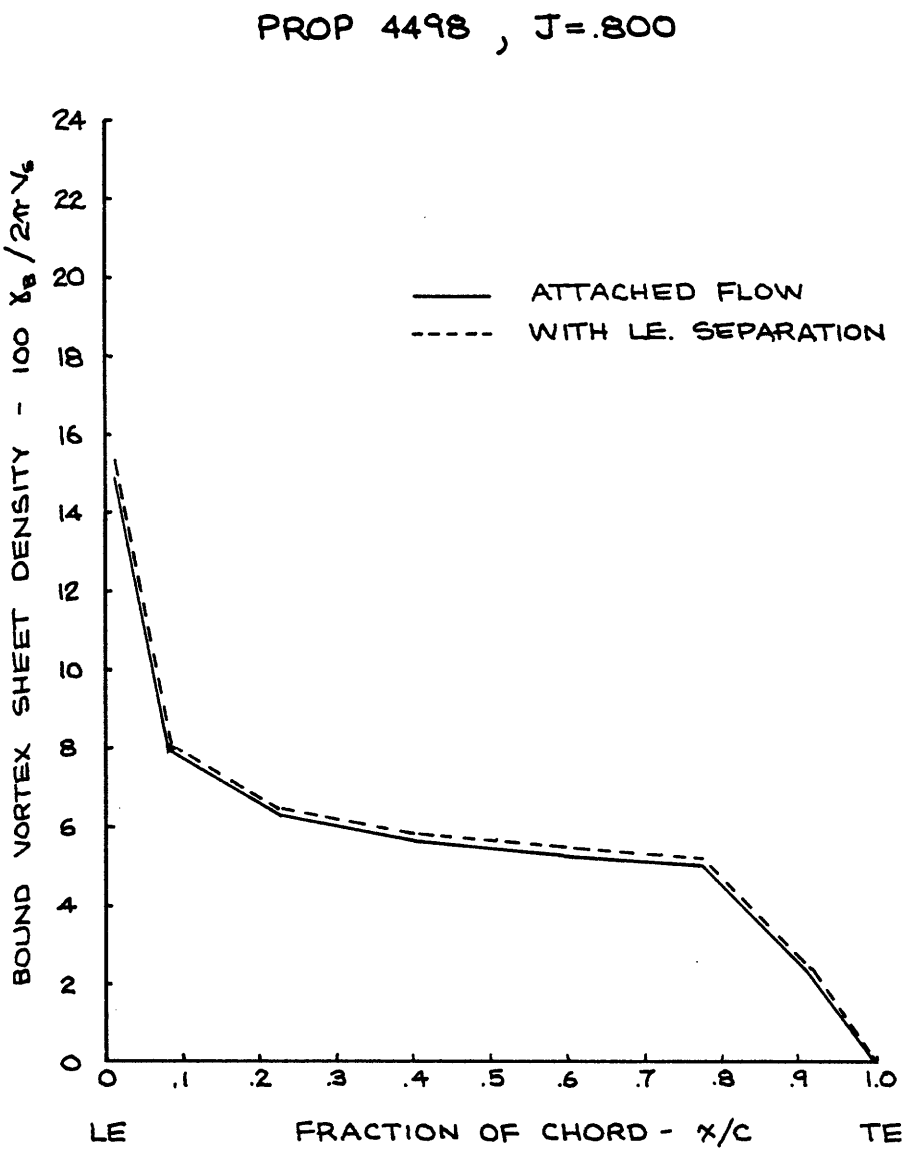

Figure 6.4.5 - Predicted chordwise loading
at r/R = .778

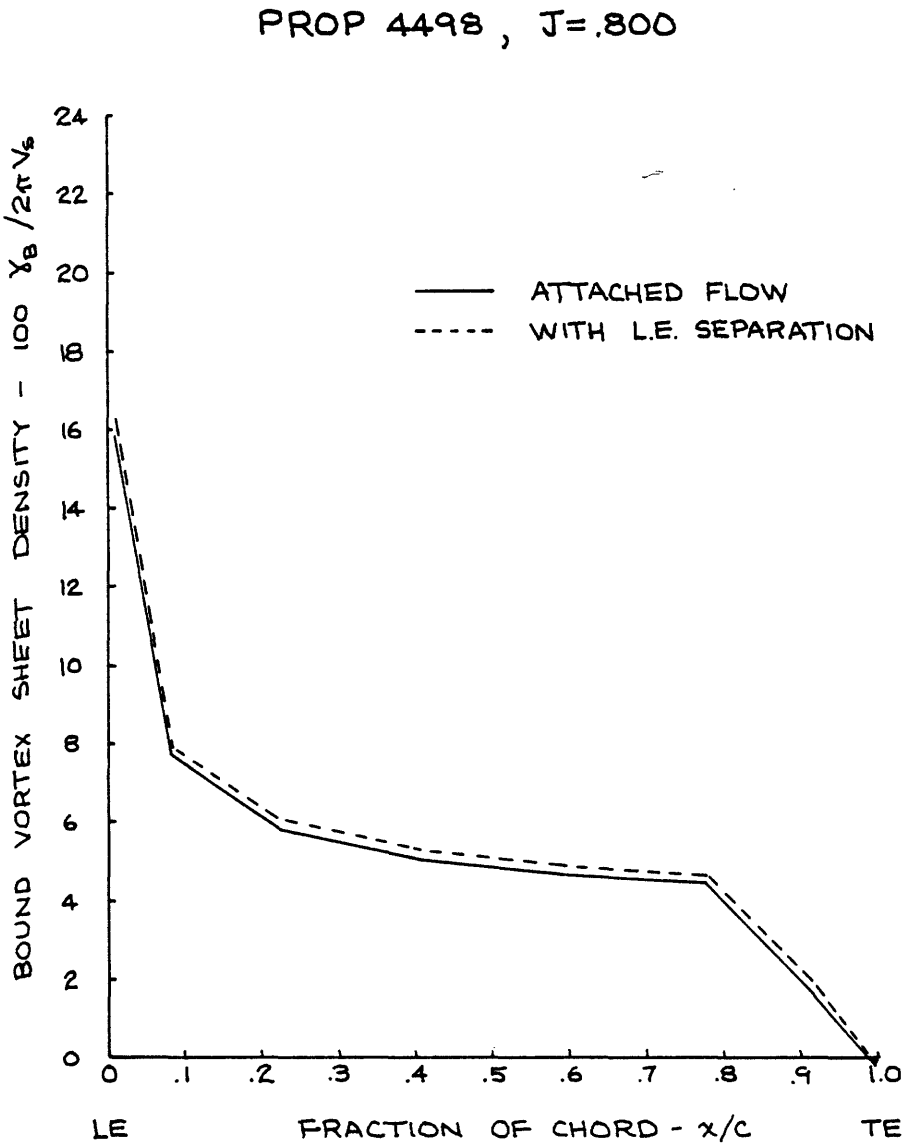

Figure 6.4.6 - Predicted chordwise loading
at r/R = .841

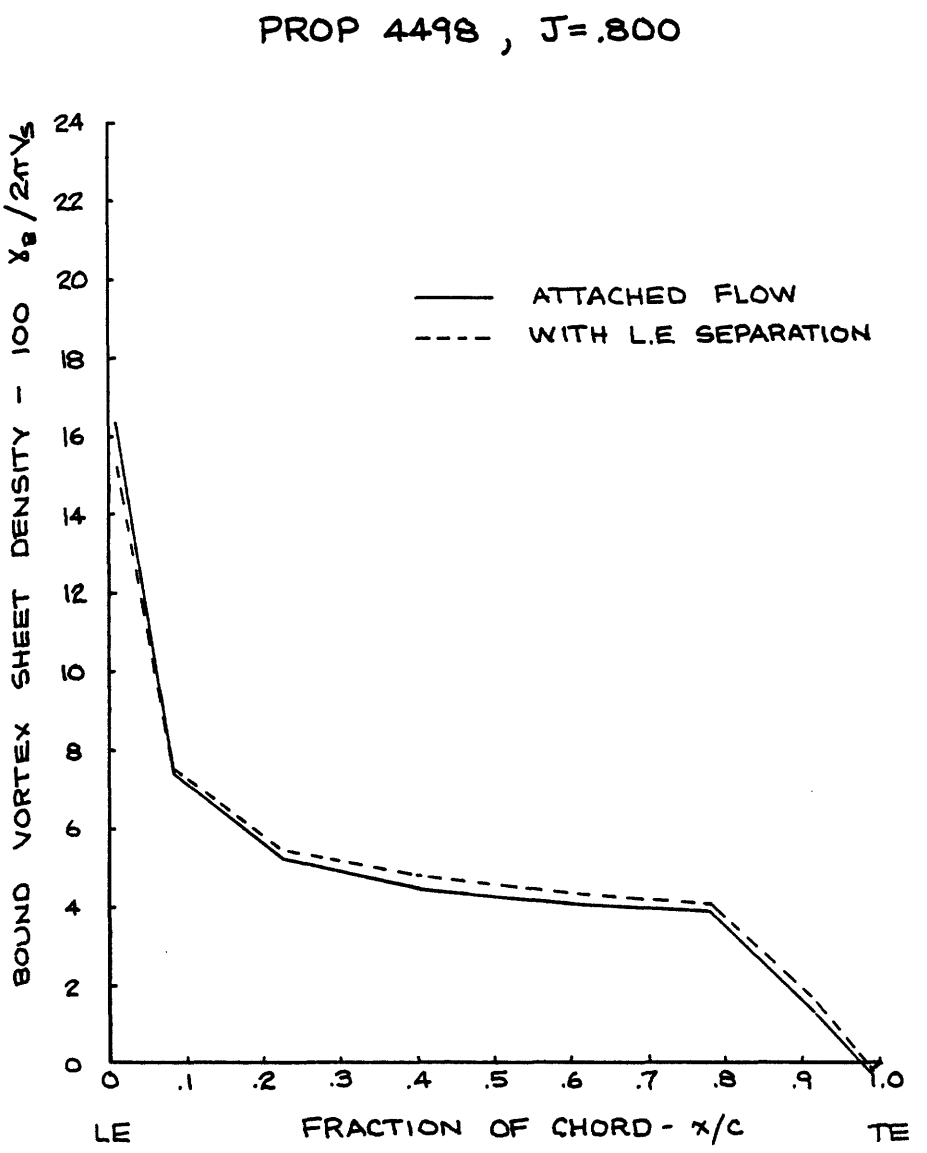

Figure 6.4.7 - Predicted chordwise loading
at r/R = .896

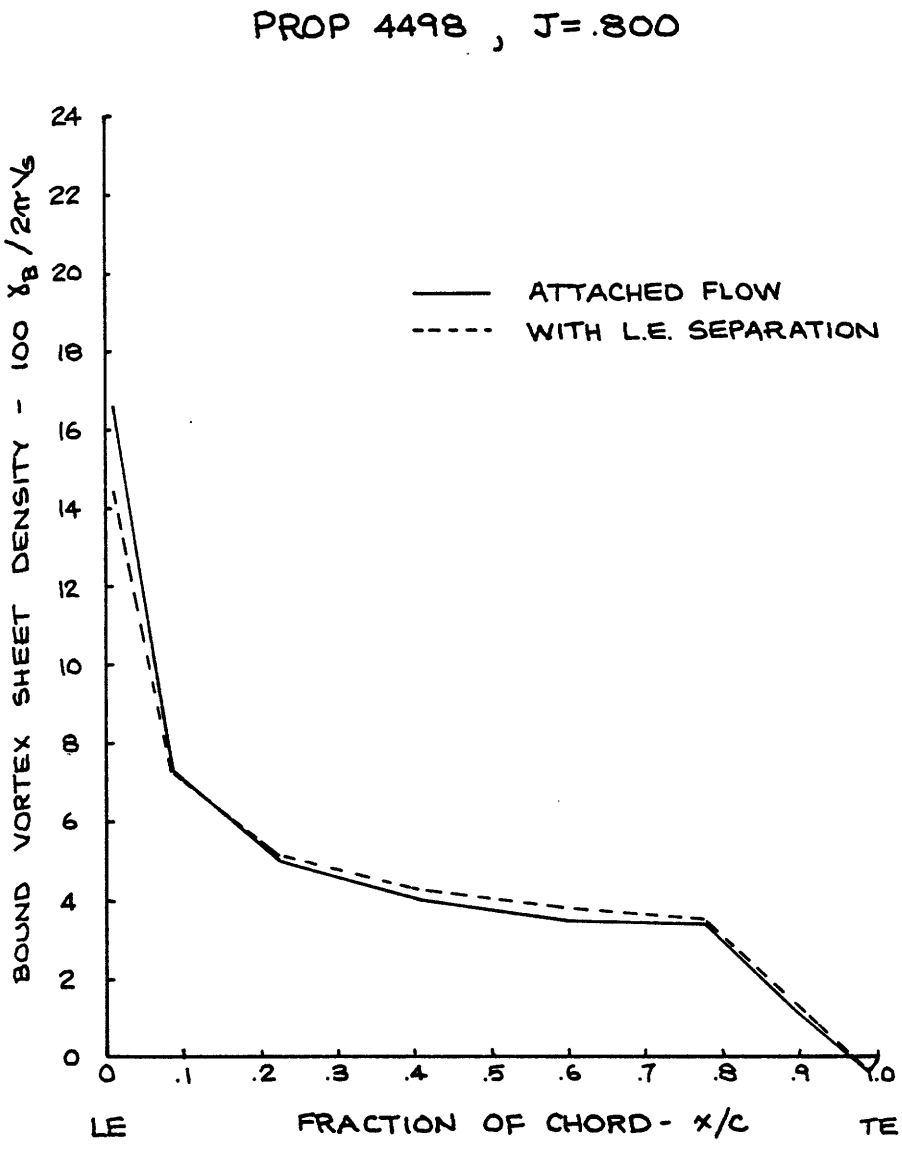

Figure 6.4.8 - Predicted chordwise loading
at r/R = .940

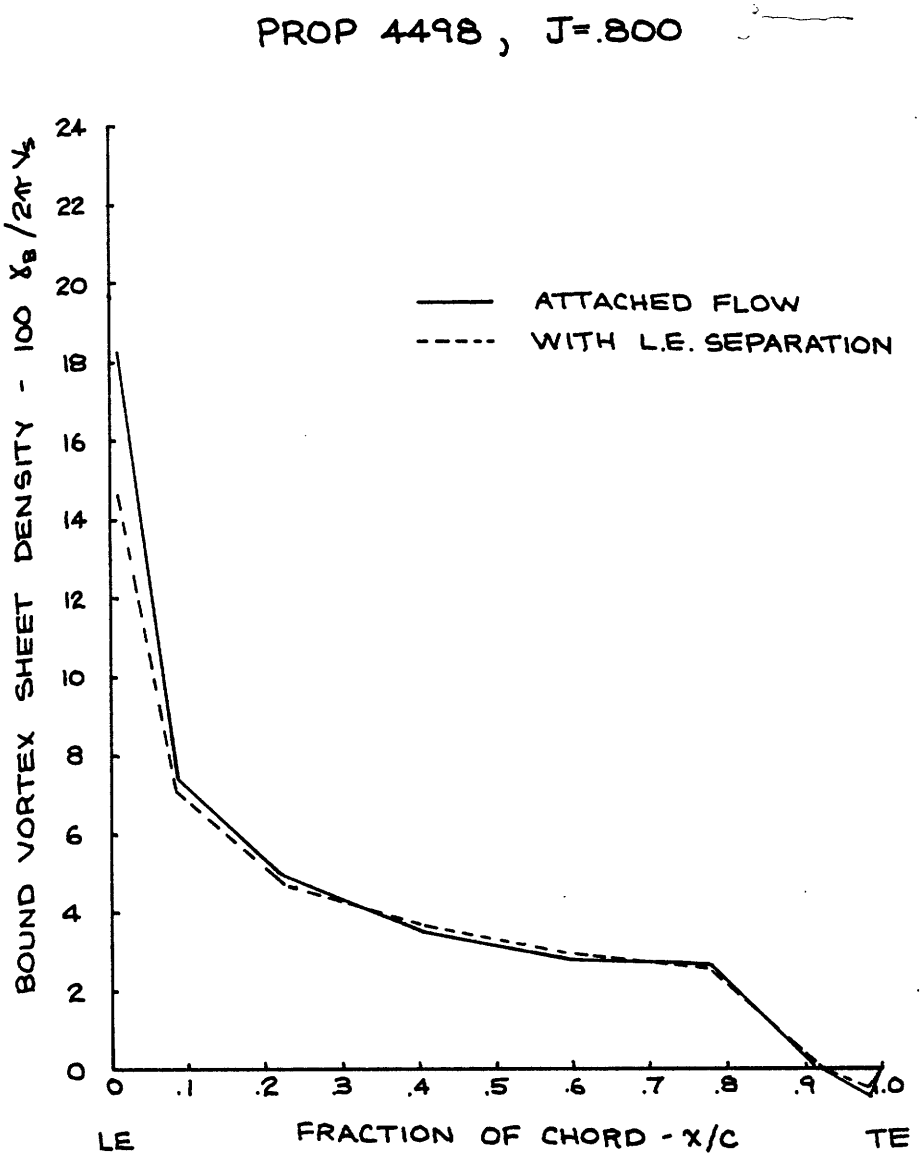

Figure 6.4.9 - Predicted chordwise loading
at r/R - .973

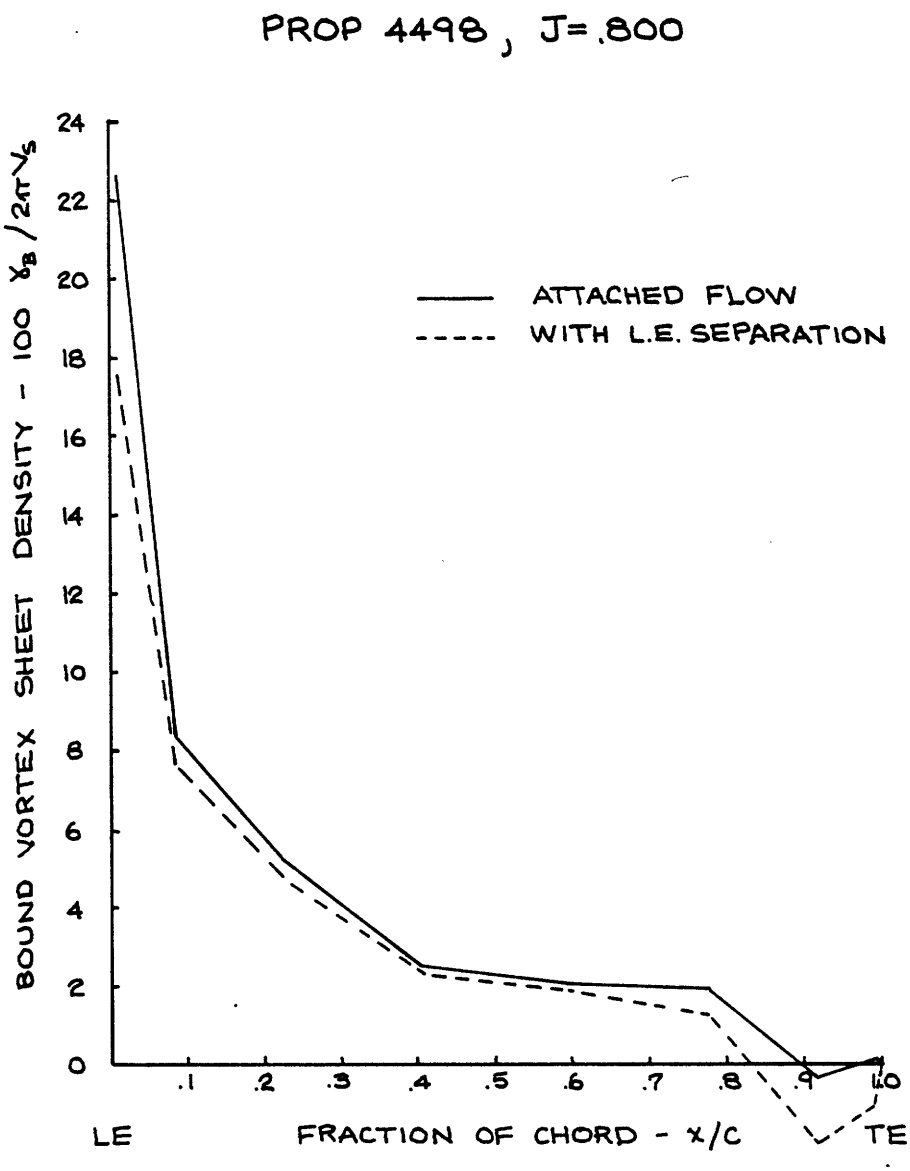

Figure 6.4.10 - Predicted chordwise loading
at r/R = .993

The computed values of thrust and torque on the blade tip are given in Table 6.4.1. The computed thrust is about the same for the three solutions. This is encouraging, since the global analysis does a good job predicting the propeller thrust over a wide range of J values (Fig. 6.1.4). The change in computed torques may reflect the difficulty in computing induced drag with a swept vortex lattice, which was mentioned previously.

Table 6.4.1

Computed Thrust and Torque on Tip of 4498 Blade Outboard of r/R = .600, at J = .800

SOLUTION	K_{F_x} (thrust)	K_{M_x} (torque)
Tip Portion of Global Solution	-.04019	.007444
Attached Flow Tip Solution	-.03996	.007249
Tip Solution with Leading Edge Separation	-.04098	.007100

Unfortunately, there are no experimental data to compare with these computations. At this advance ratio cavitation does not suffice for flow visualization, while at lower J values (heavier propeller loading) the first order representation of the leading edge vortex sheet is inadequate. This may be seen in Fig. 4.1.11 (pg. 66), which shows this propeller (4498) at J = .534. It is obvious that a model of the leading edge vortex sheet which allows for roll-up is required to model the flow at this advance ratio.

VII. Conclusions and Recommendations

7.1 Conclusions

A numerical lifting surface theory is developed for the prediction of the steady non-cavitating flow around marine propeller blade tips.

The global propeller analysis is sufficiently accurate and efficient to be used routinely in propeller design and analysis work. The procedure used to calculate the correct pitch of the trailing vortex wake eliminates the need to estimate this critical parameter for a given propeller and operating condition. Unlike most other "vortex chasing" procedures, the wake alignment algorithm developed here is sufficiently inexpensive to run so that it can be used routinely. All experience to date indicates that it is a very "robust" algorithm.

The decomposition of the tip flow analysis problem into global and local problems allows for the calculation of a high resolution tip solution without an undue penalty in computing time. Numerical results indicate that this procedure is valid if the inclusion of leading edge separation in the tip solution does not greatly alter the load distribution near the separation between global and local domains.

A viscous leading edge flow analysis is developed to predict the point at which leading edge flow separation occurs and to estimate the amount of vorticity shed into the flow at the leading edge. The analysis is semi-empirical, and is based on swept wing and airfoil section data. It appears to work well for the few cases tested. It

is the only theory known to the author which explains the effect of skew in delaying sheet cavitation inception. The analysis also indicates a large Reynolds number ("scale") effect on sheet cavitation inception which is consistent with experience.

For propeller operation not too far from design J, a first order model for the leading edge vortex sheet is developed. Calculations made using this first order model indicate a loss of loading near the leading edge of the blade, a loss of bound circulation at the extreme tip of the blade, and an increase of bound circulation inboard of the leading edge vortex sheet. These features are consistent with those found on swept wings having leading edge separation.

For operation at extreme propeller loadings a discrete vortex representation of the leading edge vortex sheet (such as that shown in Fig. 5.2.2, pg. 93) may be adequate to predict the flow quantities of interest. For operation near design J, it is possible that no potential flow model will correctly represent the leading edge vortex sheet and its interaction with the blade, since the no-slip condition at the blade surface may be significant in determining the interaction of the vortex sheet with the nearby blade. Recent work by Shamroth and Briley (1979) shows great promise in pursuing the goal of analyzing the viscous flowfield around the blade tip using a reasonable amount of computer time.

7.2 Recommendations

1) Regression equations based on experimental data should be developed so that the free parameters in the current wake model (r_w, δ_c) can easily be estimated for a given propeller at a given operating condition. The relevant parameters to regress upon are probably P/D, J, total midchord skew, and number of blades.

2) Refinements to the current wake alignment algorithm can probably be developed from a more extensive correlation of numerical results with experimental data obtained with the Laser Doppler Velocimeter in the MIT Water Tunnel.

3) Possible problems calculating induced drag using swept vortex lattices need to be investigated.

4) Much more data needs to be gathered and plotted on Fig. 4.2.2 (pg. 71) to improve confidence in the viscous leading edge analysis developed in this thesis. In particular, swept wing data on the amount of leading edge suction remaining after flow separation is needed.

5) More data on leading edge separation on propellers is needed at both model and full scale Reynolds numbers. This will probably require new methods of flow visualization.

6) An attempt should be made to develop a quantitative correlation between leading edge suction computed using the current

theory and observed cavitation inception behavior on model propellers.

7) Comparisons should be made between measured blade pressure distributions and those calculated using the current theory.

8) The model of the leading edge vortex sheet needs considerable improvement. Short of a complete viscous analysis of the tip region, a semi-empirical approach to setting the free sheet geometry is probably the best way to proceed.

REFERENCES

Arndt, R. E. A., "Cavitation in Fluid Machinery and Hydraulic Structures," Annual Reviews of Fluid Mechanics, Vol. 13, 1981.

Beasley, J. A., "Calculation of the Laminar Boundary Layer and Prediction of Transition on a Sheared Wing," Aeronautical Research Council R & M No. 3787, Oct. 1973.

Black, J., "Pressure Distribution and Boundary Layer Investigations on 44 degree Swept-Back Tapered Wing," Aeronautical Research Council CP No. 137, 1953.

Boswell, R. J., "Design, Cavitation Performance, and Open Water Performance of a Series of Research Skewed Propellers," NSRDC Report 3339, March 1971.

Brown, N. A. and Norton, J. A., "Thruster Design for Acoustic Positioning Systems," Marine Technology, Vol. 12, No. 2, April 1975.

Chappell, P. D., "Flow Separation and Stall Characteristics of Plane Constant-Section Wings in Subcritical Flow," The Aeronautical Journal of the Royal Aeronautical Society, Vol. 72, Jan. 1968.

Clapworthy, G. J. and Mangler, K. W., "The Behavior of a Conical Vortex Sheet on a Slender Wing near the Leading Edge," Aeronautical Research Council R & M No. 3790, Oct. 1974.

Cummings, D. E., "Vortex Interactions in a Propeller Wake," MIT Department of Naval Architecture and Marine Engineering Report 68-12, June 1968.

Cumpsty, N. A. and Head, M. R., "The Calculation of Three-Dimensional Turbulent Boundary Layers, Part II: Attachment Line Flow on an Infinite Swept Wing," The Aeronautical Quarterly, May 1967.

Curle, N. and Skan, S. W., "Approximate Methods for Predicting Separation Properties of Laminar Boundary Layers," The Aeronautical Quarterly, Vol. 8, Aug. 1957.

Dixon, C. J. and Sampath, S., "Development of a Viscous Vortex/Wing Interaction Program for Thick Wings with Rounded Leading Edge," Lockheed-Georgia Company, ONR-CR215-233-4F, Nov. 1978.

Francis, M. S. and Kennedy, D. A., "Formation of a Trailing Vortex," Journal of Aircraft, Vol. 16, No. 3, March 1979.

Garner, H. C., "Low Speed Theoretical and Experimental Aerodynamic Loading on Highly-Swept Curved-Tip Wings of Two Thickness," Aeronautical Research Council R & M No. 3735, Sept. 1972.

Garner, H. C. and Bryer, D. W., "Experimental Study of Surface Flow and Part-Span Vortex Layers on Cropped Arrowhead Wing," Aeronautical Research Council R & M No. 3107, April 1957.

Garner, H. C. and Cox, D. K., "Surface Oil-Flow Patterns on Wings of Different Leading Edge Radius and Sweepback," Aeronautical Research Council CP No. 583, March 1961.

Garner, H. C. and Walsh, D. E., "Pressure Distribution and Surface Flow on 5% and 9% Thick Wings with Curved Tip and 60 degree Sweepback," Aeronautical Research Council R & M No. 3244, Jan. 1960.

Gaster, M., "The Structure and Behavior of Laminar Separation Bubbles," in Separated Flows, AGARD CP No. 4, 1966.

Gaster, M., "On the Flow Along Swept Leading Edges," The Aeronautical Quarterly, May 1967.

Hall, M. G., "The Structure of Concentrated Vortex Cores," Progress in Aeronautical Sciences (ed. D. Küchemann), Vol. 7, Pergamon Press, Oxford, 1966.

Herring, R. N. and Ely, W., "Laminar Leading Edge Stall Prediction for Thin Airfoils, AIAA Paper 78-1222, 1978.

Kalman, T. P., Giesing, J. P. and Rodden, W. P., "Spanwise Distribution of Induced Drag in Subsonic Flow by the Vortex Lattice Method," Journal of Aircraft, Vol. 7, No. 6, Dec. 1970.

Kandil, O. A., Mook, D. T. and Nayfeh, A. H., "Nonlinear Prediction of Aerodynamic Loads on Lifting Surfaces," Journal of Aircraft, Vol. 13, No. 1, Jan. 1976.

Kandil, O. A., Mook, D. T. and Naybeh, A. H., "New Convergence Criteria for the Vortex Lattice Models of the Leading-Edge Separation," in Vortex Lattice Utilization Workshop, NASA SP-405, 1976.

Kerwin, J. E., "A Deformed Wake Model for Marine Propellers, " MIT Department of Ocean Engineering Report 76-6, Oct. 1966.

Kerwin, J. E., Preliminary Documentation for PBD-10 Computer Program, MIT Department of Ocean Engineering, 1981.

Kerwin, J. E. and Lee, C. S., "Prediction of Steady and Unsteady Marine Propeller Performance by Numerical Lifting Surface Theory," Transactions SNAME, Vol. 86, 1978.

Küchemann, D., "Types of Flow on Swept Wings," Journal of the Royal Aeronautical Society, Vol. 57, Nov. 1953.

Küchemann, D., "Boundary Layers on Swept Wings - Their Effects and Their Measurements," Royal Aircraft Establishment TN Aero No. 2370, April 1955.

Küchemann, D., The Aerodynamic Design of Aircraft, Pergamon Press, Oxford, 1978.

Kuiper, G., "Scale Effects on Cavitation Inception," Twelfth Symposium on Naval Hydrodynamics, Washington, June 1978.

Lan, C. E., "A Quasi-Vortex Lattice Method in Thin Wing Theory," Journal of Aircraft, Vol. 11, No. 9, Sept. 1974.

Launder, B. E. and Jones, W. P., "On the Prediction of Laminarisation," Aeronautical Research Council CP No. 1036, 1969.

Lee, C. S., "Prediction of Steady and Unsteady Performance of Marine Propellers With or Without Cavitation by Numerical Lifting Surface Theory," Ph.D. Thesis, MIT Department of Ocean Engineering, May 1979.

Lighthill, M. J., "A New Approach to Thin Airfoil Theory," The Aeronautical Quarterly, Vol. 3, Nov. 1951.

Lighthill, M. J., "Real and Ideal Fluids," in Laminar Boundary Layers (ed. Rosenhead), Clarendon Press, Oxford, 1963.

Loukakis, T. A., "A New Theory for the Wake of Marine Propellers," MIT Department of Ocean Engineering Report 71-1, May 1971.

McMahon, T. A., "Review of the Vortex Wake Rollup Problem," MIT Aeroelastic and Structures Research Laboratory ASRL TR 145-1, June 1967.

Marsden, D. J., Simpson, R. W. and Rainbird, W. J., "The Flow Over Delta Wings at Low Speeds with Leading Edge Separation," The College of Aeronautics, Cranfield, Report 114, Feb. 1958.

Maskell, E. C., "Flow Separation in Three Dimensions," Royal Aircraft Establishment Report Aero No. 2565, Nov. 1955.

Maskew, B., "A Quadrilateral Vortex Method Applied to Configurations with High Circulation," in Vortex Lattice Utilization Workshop, NASA SP-405, 1976.

Mehrotra, S. C. and Lan, C. E., "A Theoretical Investigation of the Aerodynamics of Low Aspect Ratio Wings with Partial Leading Edge Separation," NASA CR-145304, Jan. 1978.

Min, K. S., "Numerical and Experimental Methods for the Prediction of Field Point Velocities Around Propeller Blades," MIT Department of Ocean Engineering Report 78-12, June 1978.

Nelka, J. J., "Experimental Evaluation of a Series of Skewed Propellers with Forward Rake: Open-Water Performance, Cavitation Performance, Field-Point Pressures, and Unsteady Propeller Loading," NSRDC Report 4113, July 1974.

Pavelka, J. and Tatum, K. E., "Validation of a Wing Leading-Edge Stall Prediction Technique," Journal of Aircraft, Vol. 18, No. 10, October 1981.

Poll, D. I. A., "Leading Edge Transition on Swept Wings," in Laminar-Turbulent Transition, AGARD CP No. 224, 1977.

Ridder, S. O., "Experimental Studies of the Leading Edge Suction Force," International Council of the Aeronautical Sciences Preceedings, Haifa, Israel, 1974.

Sampson, R. G., "An Experimental and Theoretical Investigation of the Structure of a Trailing Vortex Wake," The Aeronautical Quarterly, Vol. 23, Feb. 1977.

Schlicting, H., Boundary Layer Theory, McGraw-Hill, New York, 1968.

Shamroth, S. J. and Briley, W. R., "A Viscous Flow Analysis for the Tip Vortex Generation Process," NASA CR-3184, 1979.

Smith, J. H. B., "A Theory of the Separated Flow from the Curved Leading Edge of a Slender Wing," Aeronautical Research Council R & M No. 3116, Nov. 1957.

Smith, J. H. B., "A Review of Separation in Steady, Three-Dimensional Flow," in Flow Separation, AGARD CP-168, 1975.

Smith, J. H. B., "Inviscid Fluid Models, Based on Rolled-Up Vortex Sheets, For Three-Dimensional Separation at High Reynolds Numbers," in Three-Dimensional and Unsteady Separation at High Reynolds Number, AGARD LS-94, 1978.

Stratford, B. S., "Flow in the Laminar Boundary Layer Near Separation," Aeronautical Research Council R & M 3002, 1954.

Stratford, B. S., "The Prediction of Separation of the Turbulent Boundary Layer," Journal of Fluid Mechanics, Vol. 5, Part I, 1959.

Taylor, G. I., "Note on the Connection Between Lift on an Aerofoil in a Wind Tunnel and the Circulation Round It," Philisophical Transactions of the Royal Society, A, Vol. 225, 1935.

Tobak, M. and Peake, D. J., "Topology of Two-Dimensional and Three-Dimensional Separated Flows," AIAA Paper 79-1480, 1979.

Tulinius, J. et al, "Theoretical Prediction of Airplane Stability Derivatives at Subcritical Speeds," North American Rockwell Report NA-72-803, 1972.

Van Dyke, M. D., "Second Order Subsonic Airfoil Theory Including Edge Effects," NACA Report 1274, 1955.

Young, A. D. and Horton, H. P., "Some Results of Investigations of Separation Bubbles," in Separated Flows, AGARD CP-4, Part II, 1966.

Weber, J. A. et al, "A Three-Dimensional Solution of Flows Over Wings with Leading Edge Vortex Separation," AIAA Journal, Vol. 14, No. 3, 1976.

Woodward, D. S. and Lean, D. E., "The Lift and Stalling Characteristics of a 35 deg. Swept Back Wing Designed to have Identical Chordwise Pressure Distributions at all Spanwise Stations when near Maximum Lift," Aeronautical Research Council R & M No. 3721, March 1971.

Appendix A: Leading Edge Suction Force and its Calculation

A.1 Leading Edge Suction Force in Thin Wing Theory

Thin wing theory is used in the present work to determine the loading on the blades. This theory assumes that the effects of loading and thickness are locally separable (loading is not really independent of thickness in the propeller case because of the non-planar geometry), and that the loading and thickness problems may be solved by placing singularities on the camberline instead of the airfoil surface. These assumptions work quite well everywhere over the foil except for the leading edge, where singularities occur.

Consider the two-dimensional lifting flow over a flat plate as shown in Fig. A.1.1. The vortex distribution $\gamma(x)$ must be such that there is no normal velocity on the plate,

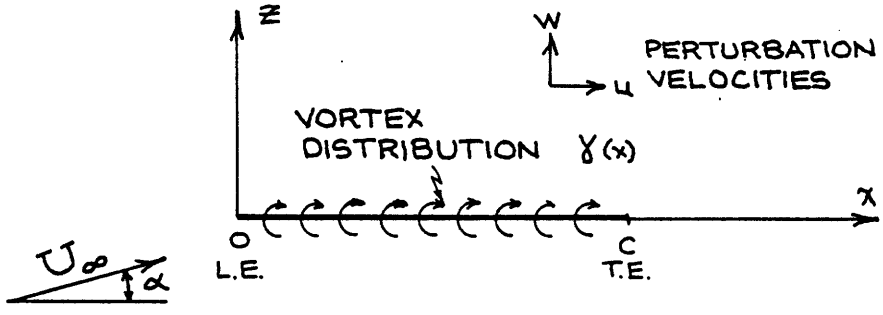

Figure A.1.1 - Two-dimensional flat plate at angle of attack

and $\gamma(x)$ must go to zero at the trailing edge (Kutta condition). The

boundary condition can be written as

$$w(x) = \frac{1}{2\pi} \int_{0}^{c} \frac{\gamma(x')\, dx'}{x-x'} = U_\infty \sin\alpha, \quad 0 < x \leq c \tag{A.1.1}$$

where $w(x)$ is the normal perturbation velocity. The solution for the vortex distribution is

$$\gamma(x) = 2\, U_\infty \sin\alpha \sqrt{\frac{c-x}{x}} \,. \tag{A.1.2}$$

The pressure jump across the foil will yield a force in the z-direction only. Since lift and drag are defined relative to the undisturbed free stream, the integration of normal pressures gives

$$C_{L_N} = 2\pi \sin\alpha \cos\alpha$$

$$C_{D_N} = 2\pi \sin^2\alpha \tag{A.1.3}$$

But in two-dimensional ideal flow, the drag should be zero. The discrepancy lies in the disregard of the leading edge suction force.

From Eq. (A.1.2), the vortex distribution is singular at the leading edge like $(x)^{-1/2}$. Define a leading edge singularity parameter C as

$$C \equiv \lim_{x \to 0} \left\{ \gamma(x) \left(\frac{x}{c}\right)^{1/2} \right\} = 2\, U_\infty \sin\alpha \tag{A.1.4}$$

Then the suction force (in the -x direction) is given by

$$F_s = \pi\rho c \frac{c^2}{4} \tag{A.1.5}$$

Making this non-dimensional in the same way as the lift and drag coefficients and resolving the leading edge force in the lift and drag directions, we obtain

$$C_{L_s} = 2\pi \sin^3 \alpha$$

$$C_{D_s} = -2\pi \sin^2 \alpha \tag{A.1.6}$$

Adding the normal pressure and suction force contributions together and retaining only second-order terms, one obtains

$$C_L = 2\pi \sin \alpha \cos \alpha$$

$$C_D = 0 \tag{A.1.7}$$

as expected.

In thin airfoil theory this finite leading edge suction force is the result of an infinitely low pressure at the leading edge (due to the infinitely high velocity) acting over a zero thickness leading edge. In reality this same force arises on thin foils from very low pressures acting on small leading edge radii. For very thick foils the suction force is actually distributed over a considerable extent of the nose region, so that the term "leading edge suction" is somewhat misleading. However, for the thin sections near the tip of propeller blades, leading edge suction force is a very useful concept.

A.2 Calculation of Leading Edge Suction for Two-Dimensional Foils

In order to determine the leading edge suction force on a 2D foil, it is necessary to compute the parameter C:

$$C \equiv \lim_{x \to o} \left\{ \gamma(x) \left(\frac{x}{c} \right)^{1/2} \right\} \qquad (A.1.3)$$

While this could be estimated from any numerical solution for the vortex distribution $\gamma(x)$, Lan (1974) discovered an alternative method which turns out to be very useful in other parts of the current work.

The development given below is due to Lan (1974). The derivation is given in terms of the vortex density $\gamma(x)$; the conversion to discrete vortices Γ_i will be given subsequently. For convenience we take $U_\infty = 1$ and $c = 1$.

The x-coordinate along the chord is transformed to the θ coordinate by

$$x = (1 - \cos\theta)/2 \ , \ (0 \leq \theta \leq \pi) \qquad (A.2.1)$$

Eq. (A.1.1) for the downwash can then be written

$$w(\theta) = \frac{-1}{2\pi} \int_o^\pi \frac{\gamma(\theta') \sin \theta' \, d\theta'}{\cos \theta - \cos \theta'} \qquad (A.2.2)$$

Define

$$g(\theta) = \gamma(\theta) \sin \theta \qquad (A.2.3)$$

and re-write Eq. (A.2.2) as

$$w(\theta) = \frac{-1}{2\pi} \int_0^{\pi} \frac{g(\theta') - g(\theta)}{\cos\theta - \cos\theta'} \, d\theta'$$

$$- \frac{g(\theta)}{2\pi} \int_0^{\pi} \frac{d\theta'}{\cos\theta - \cos\theta'}$$

$$= \frac{-1}{2\pi} \int_0^{\pi} \frac{g(\theta') - g(\theta)}{\cos\theta - \cos\theta'} \, d\theta' \qquad \text{(A.2.4)}$$

$g(\theta)$ does not have any square-root singularities because of the sin θ factor, and the integrand in Eq. (A.2.4) is finite everywhere. The integral can be approximated as a finite sum by using the midpoint trapezoidal rule:

$$\int_0^{\pi} \frac{g(\theta') - g(\theta)}{\cos\theta - \cos\theta'} \, d\theta'$$

$$\cong \Delta\theta' \sum_{k=1}^{N} \frac{g((2k-1)\Delta\theta 1/2) - g(\theta)}{\cos\theta - \cos((2k-1)\Delta\theta 1/2N)}$$

$$= \frac{\pi}{N} \sum_{k=1}^{N} \left[\frac{g((2k-1)\pi/2N)}{\cos\theta - \cos((2k-1)\pi/2N)} \right.$$

$$\left. - \frac{g(\theta)}{\cos\theta - \cos((2k-1)\pi/2N)} \right] \qquad \text{(A.2.5)}$$

if we assume $\theta \neq \theta'$.

It is desired to eliminate the last term in the above equation.

This can be done by choosing control points (θ values) such that

$$\sum_{k=1}^{N} 1/(\cos\theta - \cos((2k-1)\pi/2N)) = 0 \qquad \text{(A.2.6)}$$

The theory of Chebychev polynomials is useful for determining the correct θ values.

Let $\lambda_1, \lambda_2, \ldots, \lambda_N$ be the zeros of $T_N(\lambda)$, which is the Chebychev polynomial of the first kind. Then for some constant A,

$$T_N(\lambda) = A(\lambda-\lambda_1)(\lambda-\lambda_2)\ldots(\lambda-\lambda_N) \qquad \text{(A.2.7)}$$

and using logarithmic differentiation

$$\sum_{k=1}^{N} \frac{1}{(\lambda-\lambda_k)} = T_N'(\lambda)/T_N(\lambda) \qquad \text{(A.2.8)}$$

Let $\lambda = \cos\theta$, then $T_N(\cos\theta) = \cos N\theta$. The zeros of T_N are then $N\theta_k = (2k-1)\pi/2$, or

$$\lambda_k = \cos\theta_k = \cos((2k-1)\pi/2N), \quad k = 1, 2, \ldots, N \qquad \text{(A.2.9)}$$

which are the values of θ at which $g(\theta)$ is specified (see Eq. A.2.5).

In order to satisfy Eq. (A.2.6), we require

$$T_N'(\lambda) = \frac{d}{d\theta}(\cos N\theta)\frac{d\theta}{d\lambda} = N\frac{\sin N\theta}{\sin\theta} = 0 \qquad \text{(A.2.10)}$$

which occurs when the control points θ_i satisfy

$$\lambda_i = \cos\theta_i = \cos(i\pi/N), \qquad i = 1, 2, \ldots, N-1 \qquad \text{(A.2.11)}$$

For $i=N$, $\theta_i=\pi$, and Eq. (A.2.10) shows that $T_N'(\lambda_i) \to -N^2\cos N\pi$ and $T_N'(\lambda_i)/T_N(\lambda_i) \to -N^2$. But this occurs when $\theta=\pi$ or $x=1$, and $g(\theta)$ is

zero there, so that the control points can be extended to the trailing edge without invalidating Eq. (A.2.6). For i=0 (the leading edge), it can be shown from Eq. (A.2.10) that $T_N'/T_N \to N^2$. This allows the computation of the leading edge suction parameter C, as shown below.

The unknown function $\gamma(\theta)$ may contain a square-root singularity at $\theta=0$. Assume for now that $\gamma(x)$ is actually representing flat plate loading. Then

$$\gamma(x) = C(1-x)^{1/2}\, x^{-1/2} \tag{A.2.12}$$

Note that

$$\sin\theta = 2\, x^{1/2}\, (1-x)^{1/2} \tag{A.2.13}$$

Then

$$\lim_{\theta\to 0} g(\theta) = \lim_{\theta\to 0} \gamma(\theta) \sin\theta$$

$$= \lim_{x\to 0} C(1-x)^{1/2}\, x^{-1/2}\, 2x^{1/2}\, (1-x)^{1/2}$$

$$= 2C \tag{A.2.14}$$

So if $g(\theta)$ can be computed at $\theta=0$, the leading edge suction parameter can be determined directly.

The positions where the vortex density $\gamma(x)$ is determined are given by

$$x_k = [1 - \cos((2k-1)\pi/2N]/2, \qquad k = 1, 2, \ldots, N \tag{A.2.15a}$$

and the control point positions (where the normal velocity is specified)

are given by

$$x_i = [1 - \cos(i\pi/N)]/2, \qquad i = 0, 1, 2, \ldots, N \tag{A.2.15b}$$

Eq. (A.2.4) can now be written as

$$w(x_i) \cong \frac{1}{2N} \sum_{k=1}^{N} \frac{\gamma_k \, x_k^{1/2} (1-x_k)^{1/2}}{x_i - x_k} + \begin{cases} NC, & i = 0 \\ 0, & i \neq 0 \end{cases} \tag{A.2.16}$$

To determine the γ_k for a given foil, (given downwash distribution), Eq. (A.2.16) is written as a matrix equation

$$w_i = \sum_{k=1}^{N} a_{ik} \, \gamma_k \,, \qquad i = 1, 2, \ldots, N \tag{A.2.17a}$$

where

$$a_{ik} = \frac{1}{2N} \frac{x_k^{1/2} (1-x_k)^{1/2}}{x_i - x_k} \tag{A.2.17b}$$

Once the γ_k's are known, the leading edge suction parameter C can be computed using

$$C = \frac{w_0}{N} + \frac{1}{2N^2} \sum_{k=1}^{N} \gamma_k \left\{ \frac{1-x_k}{x_k} \right\}^{1/2} \tag{A.2.18}$$

where w_0 is the component of the inflow velocity normal to the camber-line at the leading edge.

The lift coefficient is given by

$$c_\ell = 2 \int_0^1 \gamma(x) \, dx = \int_0^\pi \gamma(\theta) \, \sin\theta \, d\theta$$

$$\cong \frac{\pi}{N} \sum_{k=1} \gamma_k \sin \theta_k \tag{A.2.19}$$

It may be demonstrated numerically that the formulation presented here gives the exact vorticity distribution, leading edge suction parameter, and lift coefficient for both flat plate and parabolic arc camberlines, for any value of N.

The above formulation is presented in terms of the vortex sheet density γ_k at certain locations x_k, whereas the lifting surface theory for the propeller is developed in terms of discrete vortex strengths Γ_k. If the above theory for two-dimensional airfoils is developed using discrete vortices at the locations x_k, one obtains

$$\Gamma_k = \gamma_k \cdot \frac{\pi}{N} \; x_k^{1/2} \; (1-x_k)^{1/2} \qquad \text{(A.2.20)}$$

relating discrete vortex strengths and vortex sheet density at x_k. One also obtains

$$w_i = \sum_{k=1}^{N} b_{ik} \, \Gamma_k \qquad i = 1, 2, \ldots, N \qquad \text{(A.2.21)}$$

where:

$$b_{ik} = \frac{1}{2\pi} \cdot \frac{1}{x_i - x_k} \qquad \text{(A.2.22)}$$

which is the usual formulation of the vortex lattice method for two-dimensional foils. In this case the vortices and control points are arranged along the chord using cosine spacing identical to that used in the propeller case (Section 3.2), rather than the more commonly used uniform spacing. The leading edge suction parameter C may be calculated from

$$C = \frac{1}{N} \left[w_0 + \frac{1}{2\pi} \sum_{k=1}^{N} \frac{\Gamma_k}{x_k} \right] \qquad \text{(A.2.23)}$$

A.3 Calculation of Leading Edge Suction for Three Dimensional Lifting Surfaces

Lan (1974) showed that the above method for calculating the leading edge suction parameter C is readily extended to three dimensional lifting surfaces. The geometry of a typical swept wing is shown in Fig. A.3.1. The value of C for a particular section of the wing is defined by

$$C \equiv \lim_{x \to x_{l.e.}} \left\{ \gamma(x) \left(\frac{x}{c} \right)^{1/2} \right\} \tag{A.3.1}$$

where now $\gamma(x)$ is the density of the spanwise vorticity on the wing made non-dimensional by U_∞ and c is the local wing chord. Representing the wing loading with a vortex lattice utilizing N cosine-spaced vortices in the chordwise direction, Lan shows that C may be computed from

$$C = \frac{1}{N} \left[\begin{array}{l} \text{total computed upwash (free stream and} \\ \text{induced) at the leading edge control point} \end{array} \right] \tag{A.3.2}$$

and the leading edge thrust coefficient c_t may be computed from

$$c_t \equiv \frac{\text{Thrust/unit span}}{\frac{1}{2} \rho \, c \, U_\infty^2}$$

$$= \frac{\pi C^2}{2 \cos \Lambda_l} \tag{A.3.3}$$

where Λ_l is the leading edge sweep angle relative to the plane normal to U_∞. This approach is used to calculate the leading edge suction in

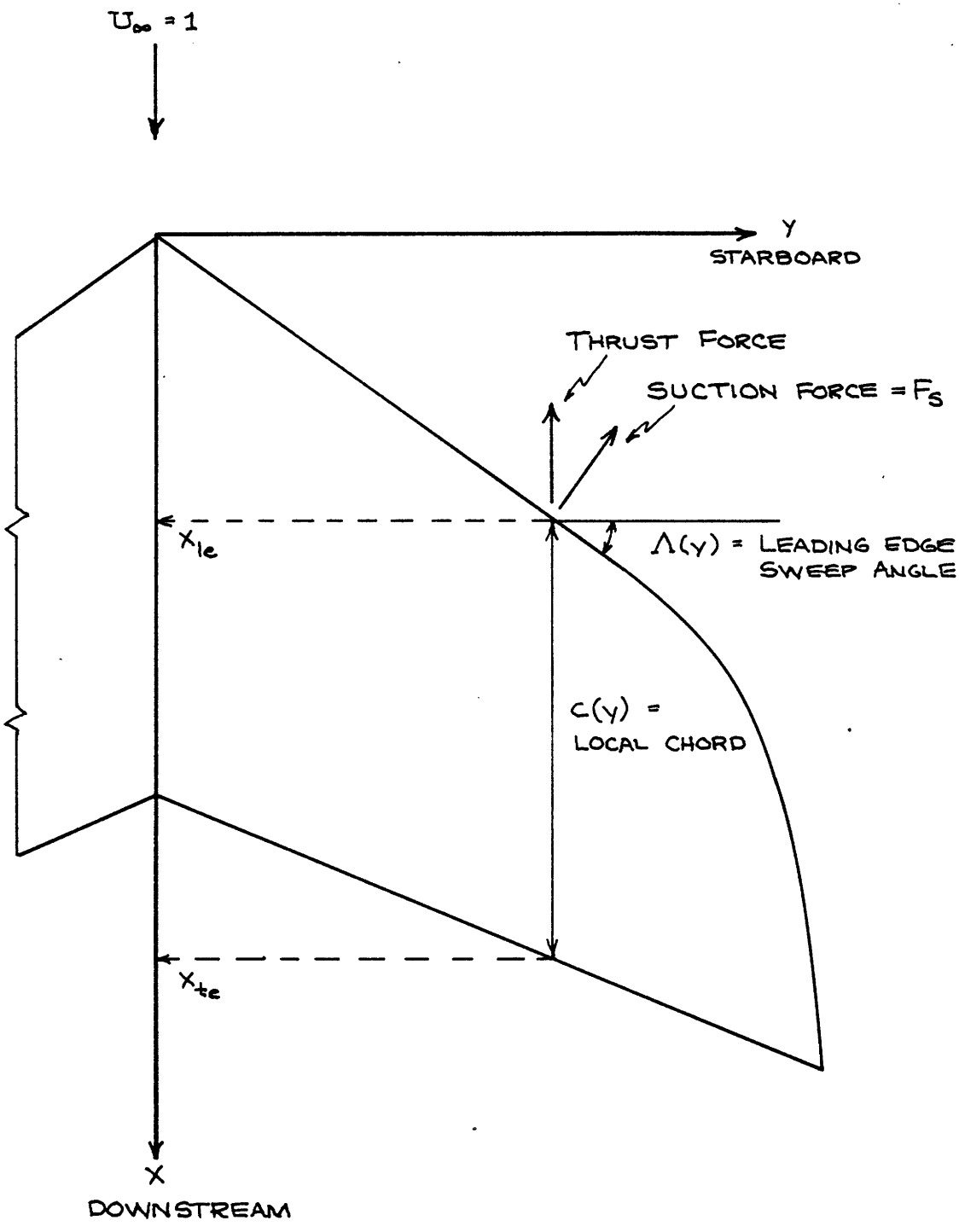

Figure A.3.1 - Plan view of swept wing

the attached flow tip solution (Section 3.9), making use of the relation

Thrust per unit span = Suction Force per unit length of leading edge.

Appendix B: Calculation of Trailing Vortex Wake Pitch

B.1 Calculation of Ultimate Wake Pitch

The ultimate wake is assumed to consist of K equally spaced helical tip vortices of strength Γ_t and radius r_w surrounding a single rolled-up hub vortex of strength $-K\times\Gamma_t$. If we examine a point in the ultimate wake sufficiently far from the propeller, it may be safely assumed that the ultimate wake extends to infinity both fore and aft, thus simplifying the geometry of the problem. In a coordinate system rotating with the propeller, the velocity seen at a point on one of the tip vortices consists of the propeller rotational velocity, the speed of advance, the induced velocities due to the helical vortices, and the induced velocity due to the hub vortex. Since the tip vortices are force-free, the total velocity must be tangent to the tip vortex helix at each point. Using this fact the pitch angle of the ultimate tip vortices may be calculated.

Loukakis (1971) considered this problem in detail and noted that the local self-induced velocity of a helical vortex line is infinite. To remove this singularity it is necessary to recognize the existance of a finite core in the tip vortex, over which the vorticity is distributed. Loukakis performed extensive numerical calculations of the self induced velocities of a set of K symmetrically located, infinitely extended, helical vortex cores, with the ratio (core radius/helix radius) as a parameter. His results, which are utilized in the present work, are listed in Table B.1.1. This table gives the axial and tangential self-induced velocities as a function of K and tan β_w. The ratio

	K=1		K=2		K=3		K=4		K=5		K=6		K=7	
TAN β_w	UA	UT	UA	UT	UA	UT	UA	UT	UA	UT	UA	UT	UA	UT
0.10	0.9800	0.0353	1.7169	0.1261	2.4920	0.2664	3.2513	0.2893	4.0256	0.4223	4.8161	0.5077	5.6083	0.5145
0.15	0.7416	0.0200	1.2162	0.1116	1.7158	0.2114	2.2191	0.2784	2.7277	0.3700	3.2455	0.4573	3.7647	0.5179
0.20	0.6234	0.0009	0.9668	0.0931	1.3326	0.1830	1.7059	0.2622	2.0835	0.3459	2.4663	0.4307	2.8502	0.5066
0.25	0.5503	-0.0185	0.8161	0.0748	1.1029	0.1628	1.3978	0.2457	1.6969	0.3286	1.9996	0.4121	2.3041	0.4923
0.30	0.4980	-0.0370	0.7131	0.0576	0.9479	0.1457	1.1907	0.2302	1.4377	0.3134	1.6875	0.3966	1.9391	0.4781
0.35	0.4564	-0.0539	0.6364	0.0419	0.8347	0.1305	1.0405	0.2158	1.2504	0.2996	1.4628	0.3827	1.6770	0.4647
0.40	0.4210	-0.0690	0.5757	0.0277	0.7470	0.1169	0.9254	0.2028	1.1076	0.2870	1.2923	0.3702	1.4786	0.4525
0.45	0.3896	-0.0820	0.5252	0.0153	0.6760	0.1049	0.8333	0.1912	0.9943	0.2757	1.1575	0.3591	1.3223	0.4415
0.50	0.3611	-0.0930	0.4820	0.0047	0.6166	0.0947	0.7574	0.1812	0.9015	0.2659	1.0477	0.3494	1.1954	0.4319
0.60	0.3103	-0.1092	0.4103	-0.0114	0.5215	0.0789	0.6379	0.1657	0.7571	0.2505	0.8782	0.3340	1.0005	0.4166
0.70	0.2665	-0.1189	0.3523	-0.0214	0.4474	0.0688	0.5468	0.1555	0.6487	0.2403	0.7521	0.3237	0.8566	0.4062
0.80	0.2287	-0.1234	0.3043	-0.0266	0.3877	0.0633	0.4747	0.1498	0.5637	0.2343	0.6541	0.3175	0.7454	0.3998
0.90	0.1962	-0.1141	0.2641	-0.0280	0.3386	0.0613	0.4161	0.1474	0.4954	0.2316	0.5758	0.3145	0.6569	0.3966
1.00	0.1686	-0.1221	0.2304	-0.0269	0.2978	0.0619	0.3678	0.1475	0.4394	0.2313	0.5118	0.3139	0.5850	0.3956

Core Radius/Helix Radius = 0.02
(From Loukakis, 1971)

Table B.1.1 - Self induced velocities of a set of K equally spaced, infinitely extended helical vortex cores

(core radius/helix radius) was selected to be 0.02, as described below. All of the induced velocities shown are computed for $r_w = 1$ and $\Gamma_t = 1$. The actual values of the velocities can be calculated by multiplying the values in the table by Γ_t/r_w.

The velocity diagram at one of the tip vortices is shown in Fig. B.1.1.

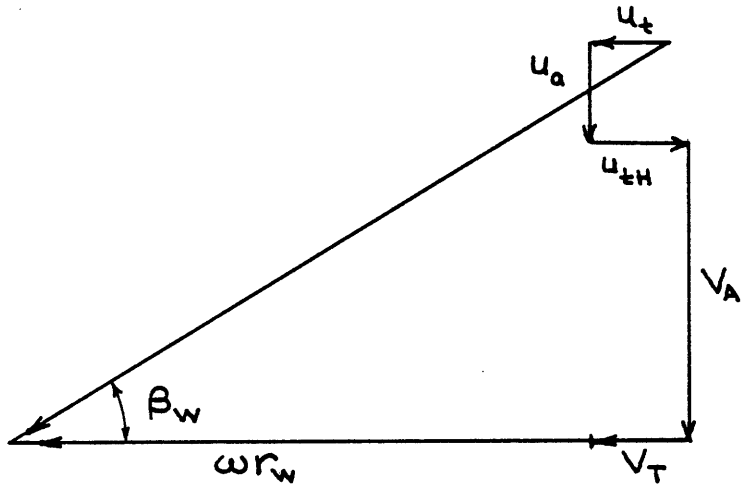

Figure B.1.1 - Velocity diagram at ultimate tip vortex

where: ωr_w = tangential velocity due to propeller rotation

V_A = axial inflow velocity at r_w

V_T = tangential inflow velocity at r_w

$u_{tH} = \frac{-K\Gamma_t}{2\pi r_w}$ is the tangential velocity induced by the hub vortex

$u_a = \frac{\Gamma_t}{r_w}$ · UA is the axial velocity induced by the helical tip vortices

$u_t = \frac{\Gamma_t}{r_w}$ · UT is the tangential velocity induced by the helical tip vortices

and UA, UT are taken from Table B.1.1.

The pitch angle β_w of the ultimate wake can then be found by solving the following equation:

$$\tan \beta_w = \frac{V_A + \frac{\Gamma_t}{r_w} \cdot UA(\tan \beta_w, K)}{\omega r_w + V_T + \frac{\Gamma_t}{r_w} \cdot UT(\tan\beta_w, K) - \frac{K\Gamma_t}{2\pi r_w}} \qquad \text{(B.1.1)}$$

This yields the ultimate wake pitch $\tan \beta_w$ and the induced velocities at the ultimate tip vortex, $u_{a2}(r_w)$ and $u_{t2}(r_w)$, where $u_{a2}(r_w) = u_a$ from above, and $u_{t2}(r_w) = u_t + u_{tH}$.

It is usually assumed that the trailing vortex wake from a wing completely rolls up into two trailing tip vortices, implying that the circulation of each ultimate tip vortex is equal to the maximum bound circulation around the wing. Detailed measurements behind lifting wings by Sampson (1977) show that this is not the case: the circulation of the tip vortices is only 60-80% of the maximum bound circulation. Similarly, laser velocimeter measurements behind an operating propeller show a weak vortex sheet at intermediate radii quite far downstream. It was found from extensive numerical experimentation that a (core radius/helix radius) ratio of 0.02 and an ultimate tip vortex strength of 80% of the maximum circulation on the blade yielded predicted ultimate wake pitches in remarkable agreement with experimentally measured values.

The values of the axial and tangential induced velocities in the ultimate wake at the ultimate-hub vortex radius r_{wH} are determined from

the following relations:

$$u_{a2}(r_{wH}) = \frac{.75\ K\ \Gamma_t}{r_w \tan \beta_w}$$

$$u_{t2}(r_{wH}) = \frac{-.75\ K\ \Gamma_t}{r_{wH}} \qquad \text{(B.1.2)}$$

The factor 0.75 was included after comparing computed wake velocities and the experimental measurements by Min (1978).

B.2 Calculation of Transition Wake Pitch

The calculation of the pitch of the transition wake is complicated by the fact that the pitch is allowed to vary in both the radial and downstream directions. The extensive laser velocimeter measurements of propeller vortex wakes by Min (1978) and ealier visual measurements by Kerwin (1976) indicate that the wake pitch varies smoothly with both radius and axial location. Accordingly, it was considered reasonable to calculate the pitch at a limited number of points in the transition wake and interpolate to obtain the pitch at other locations.

The velocity diagram of any point in the transition wake of the key blade is shown in Fig. B.2.1, in a coordinate system rotating with the propeller.

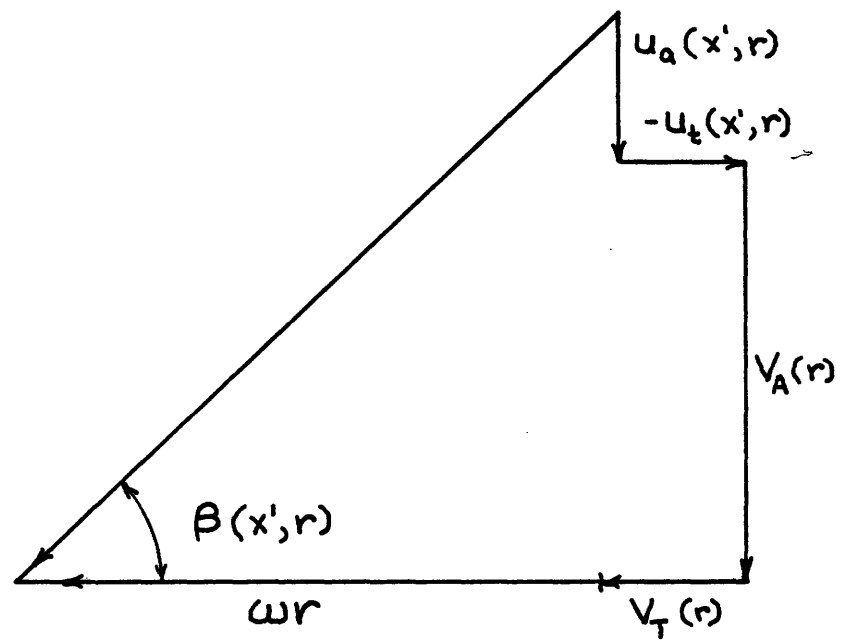

Figure B.2.1 - Velocity diagram in transition wake

where: r = radius

x' = axial position downstream of the blade trailing edge

ωr = propeller rotational velocity at radius r

$V_A(r)$ = axial inflow velocity

$V_T(r)$ = tangential inflow velocity

$u_a(x',r)$, $u_t(x',r)$ = axial and tangential induced velocities due to the propeller and wake singularity system

$\beta(x',r)$ = local pitch angle of the transition wake

In determining the transition wake geometry the axial and tangential induced velocities are calculated at certain points and interpolated at other locations, rather than the pitch angle $\beta(x',r)$ itself.

The transition wake geometry is correct (force-free) when the induced velocities $u_a(x',r)$ and $u_t(x',r)$ calculated using an assumed pitch distribution $\tilde{\beta}(x',r)$ yield a calculated pitch distribution

$$\beta(x',r) = \tan^{-1}\left[\frac{V_A(r) + u_a(x',r)}{\omega r + V_T(r) + u_t(x',r)}\right] \qquad (B.2.1)$$

such that $\beta(x',r) = \tilde{\beta}(x',r)$ everywhere. This requires an iterative procedure, which usually converges quite rapidly.

Fig. B.2.2 shows the assumed downstream variation of induced velocities in the transition wake region. Although the axial extent of the transition wake region is set by x_{tw}, where x_{tw} is typically one propeller radius, the induced velocities are allowed to change in the downstream direction until $x' = x_{final}$, where x_{final} is usually set to 1.5 R based on experimental observations. Expressed algebraically,

$$u_a(x',r)\begin{cases} = u_{a1}(r) + (u_{a2}(r) - u_{a1}(r)) \cdot (3\xi - 3\xi^2 + \xi^3), & \xi \leq 1 \\ = u_{a2}(r), & \xi > 1 \end{cases} \qquad (B.2.2)$$

where: $u_{a1}(r)$ = the axial induced velocity at the blade trailing edge

$u_{a2}(r)$ = the axial induced velocity in the ultimate wake

ξ = x'/x_{final}

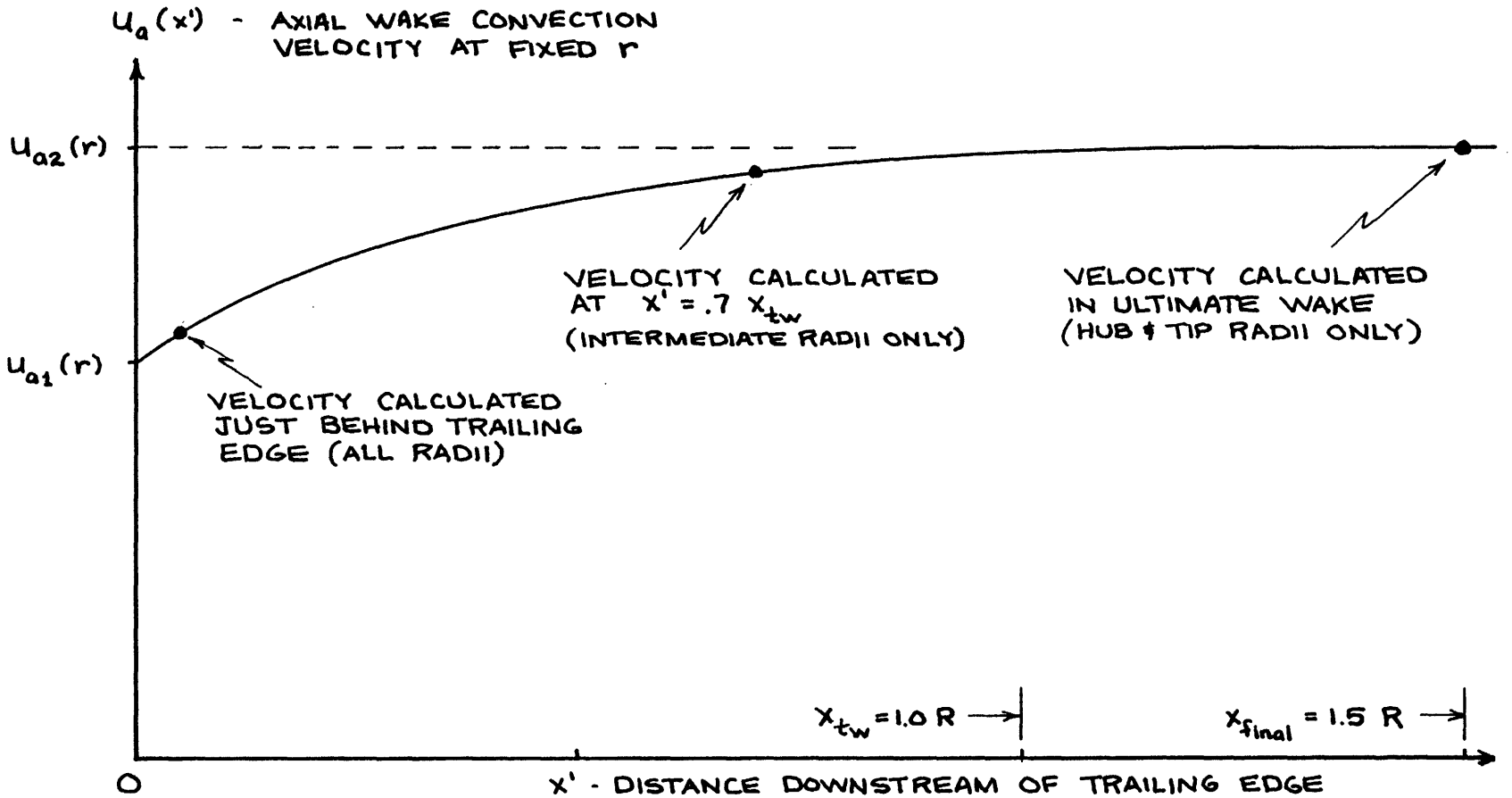

Figure B.2.2 - Assumed variation of wake convection velocities in downstream direction

The same expressions are used for the downstream change in tangential induced velocities. The form of Eq. (B.2.1) was chosen after examining Min's (1978) laser measurements of propeller vortex wakes.

Fig. B.2.3 illustrates the variation of axial induced velocities at the key blade transition wake as a function of x' and r. A similar graph could be drawn for the tangential induced velocities in the transition wake region.

Most of the discrete trailers in the transition wake model are actually representing part of a vortex sheet, and it is reasonable to disregard the local self-induced velocity of the curved vortex line. At the tip of the blade, however, the vortex sheet rolls up considerably even before the trailing edge of the blade is reached, so that the outermost discrete trailer leaving the blade is actually representing a vortex core. In this case it is correct to assume a viscous core size and calculate the local self-induced velocity of the trailer leaving the tip. If a viscous core radius of 0.1% of the propeller radius is assumed, the calculated pitch of the tip vortex just behind the blade tip is in good agreement with Min's (1978) measurements for several propellers over a range of advance coefficients.

The procedure used to align the wake for a given vorticity distribution on the propeller and in the wake is as follows:

a) Calculate the pitch of the ultimate tip vortices. This also yields the quantities $u_{a2}(r_w)$, $u_{a2}(r_{wH})$, $u_{t2}(r_w)$, and $u_{t2}(r_{wH})$.

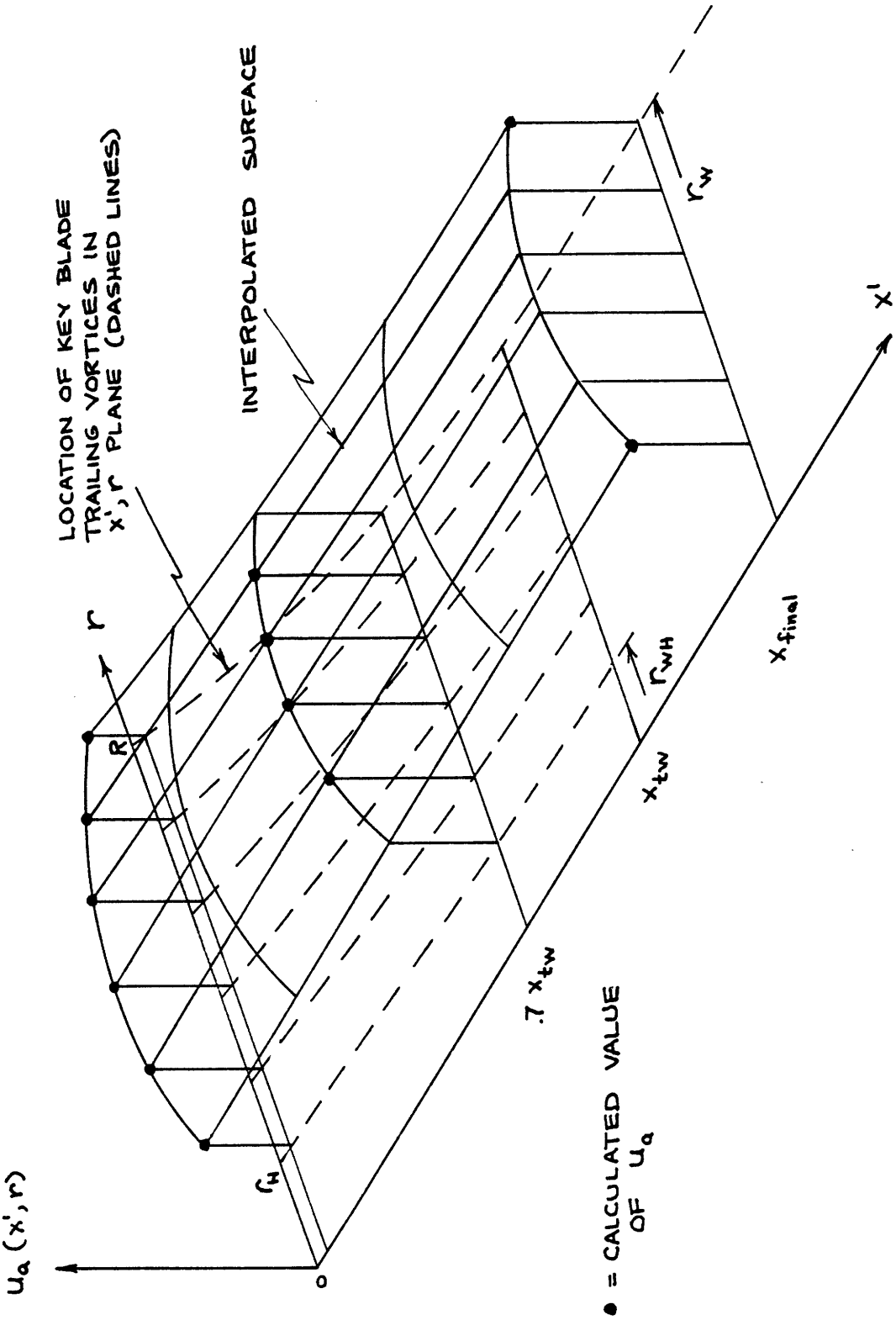

Figure B.2.3 - Variation of axial convection velocities with radius and distance downstream

b) Using a previously assumed transition wake geometry, calculate induced velocities at the key blade transition wake at points just behind the blade and at $x' = 0.7\ x_{tw}$.

c) Using these calculated induced velocities in the transition wake and the induced velocities at the start of the ultimate wake from step a), interpolate to find the induced velocities everywhere in the transition wake and calculate a new transition wake geometry.

d) Repeat steps b) and c) until the transition wake geometry stops changing.

Since the calculated vorticity distribution depends on the wake geometry, the boundary value problem must be solved several times, with the wake re-aligned at each step. Fortunately, this process converges quite rapidly.

It is found that the computed induced velocities in the transition wake near the hub and tip of the blade are sensitive to the number of trailers used to represent the transition wake. Any numerical scheme exhibiting this kind of behavior is usually dismissed as being unreliable. However, if the present scheme is used with eight spanwise panels on the key blade (nine trailing vortices), the computed results are reasonable and in good agreement with the experiments of Min (1978) for a variety of different propellers and advance coefficients. Therefore, the current wake alignment scheme is only used with eight spanwise panels on the blade. Once the induced velocities in the wake are calculated from this analysis

they may be used to specify the wake geometry for use with any desired number of spanwise panels on the key blade.

Appendix C: Two Dimensional Laminar Separation Bubbles

C.1 Introduction

The characteristics of airfoil sections in real fluids depend on the type of flow separation present, which governs the stalling characteristics of sections. Three types of stall behavior are observed for two-dimensional airfoil sections in low Mach number flow, which correspond to different types of behavior possible for the boundary layer on the suction side of the foil:

a) Trailing-edge stall, with the separation point of the turbulent boundary layer moving forward from the trailing edge as the incidence increases. This type of stall usually occurs on rather thick sections ($t_o/c > 0.12$) or those having a large amount of camber. This type of stall is gradual, as shown in Fig. C.1.1a.

b) Leading-edge stall, caused by a sudden failure of the flow to reattach to the airfoil following laminar boundary layer separation near the nose. This behavior is typical of moderately thick airfoils ($0.09 < t_o/c < 0.15$) and is a very abrupt stall (Fig. C.1.1b).

c) Thin airfoil stall, with laminar separation near the leading edge and turbulent reattachment at a point which moves rearward as the incidence is increased. This type of stall is found on thin airfoils ($t_o/c < 0.09$) and is a gentle stall, as shown in Fig. C.1.1c.

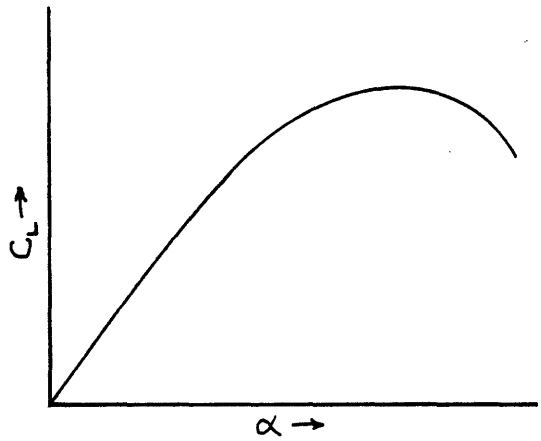

a) Trailing edge stall (thick or highly cambered sections)

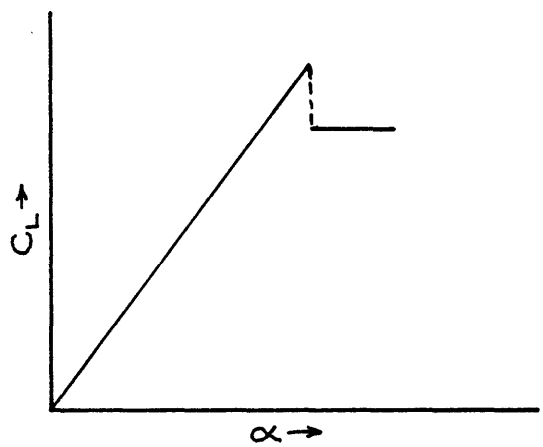

b) Leading edge stall (moderately thick sections)

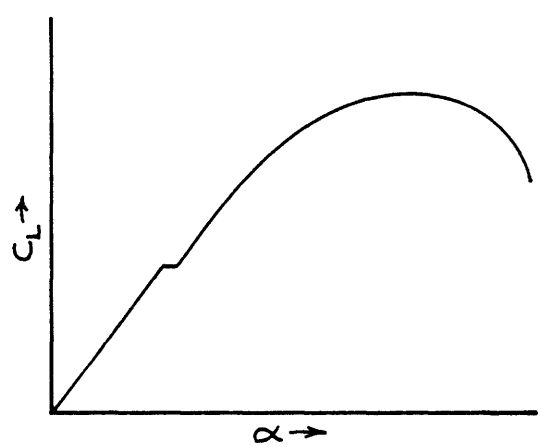

c) Thin airfoil stall (thin sections)

(From Chappell, 1967)

Figure C.1.1 - C_L vs. α curves for three types of stall

Further discussion will be restricted to the types of flow found in b) and c) above, as both of these involve the presence of laminar separation bubbles near the leading edge of the airfoil. The behavior of the leading edge separation bubble greatly influences the nature of the flow along swept leading edges, as shown in Chapter IV.

C.2 The Nature of Separation Bubbles

Laminar separation bubbles occur on two-dimensional airfoil sections operating above their ideal angle of attack because the laminar boundary layer on the suction side is unable to negotiate the adverse pressure gradient following the suction peak near the nose. The boundary layer separates and forms a thin free shear layer above the airfoil surface. This shear layer is highly unstable to disturbances and usually undergoes transition to turbulence, which may enable the flow to reattach to the foil as a turbulent boundary layer downstream of the separation point. The shear layer then encloses a mostly stagnant region of fluid known as a separation bubble, in which the pressure is sensibly constant.

Some understanding of separation bubbles can be gained by examining the distribution of vorticity around an airfoil section. In inviscid flow the foil section can be represented as a distribution of vorticity on the surface of the foil. The strength and distribution of the surface vorticity is determined by requiring the airfoil surface to be a streamline, and imposing a Kutta condition at the trailing edge.

In the real flow past an airfoil the vorticity is nonzero everywhere, although at high Reynolds numbers the vorticity is concentrated near the foil surface (boundary layer approximation). If the boundary layer is thin compared to the dimensions of the foil, we may consider the vorticity to be concentrated into a thin vortex sheet at the foil surface. The vorticity distribution must be such that the foil surface is a streamline and the local vorticity represents the drop in velocity from outside the boundary layer to zero at the wall. In viscous flow the airfoil surface is a distributed source of vorticity which sheds vorticity into the wake behind the foil. The net vorticity behind the foil must be zero, since a non-zero value of circulation is obtained only for a path enclosing the foil. Thus the vorticity shed from the upper surface is equal to, but of opposite sign, from that that shed from the lower surface, as pointed out by Taylor (1935).

Separation bubbles may be thought of as regions of mostly stagnant fluid adjacent to the airfoil surface, separated from the main potential flow by a thin vortex sheet. Fig. C.2.1 shows the flow near the leading edge of a foil with a "short" bubble present. The height of this bubble is very small (< 0.0001 × chord), so that the vortex distribution on bubble surface is not very different from the distribution on the airfoil surface in the absence of the bubble, and the bubble has only a small influence on the surface pressures. Fig. C.2.2 illustrates the kind of flow with a "long" bubble present, which occurs when the flow fails to reattach just behind the laminar

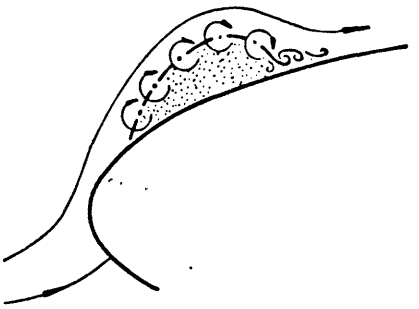

Figure C.2.1 - Flow with short bubble near leading edge
(Height of bubble exaggerated)

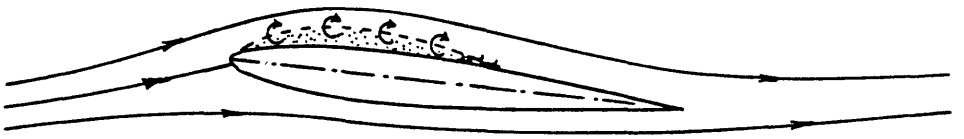

Figure C.2.2 - Flow with long bubble
(Height of bubble exaggerated)

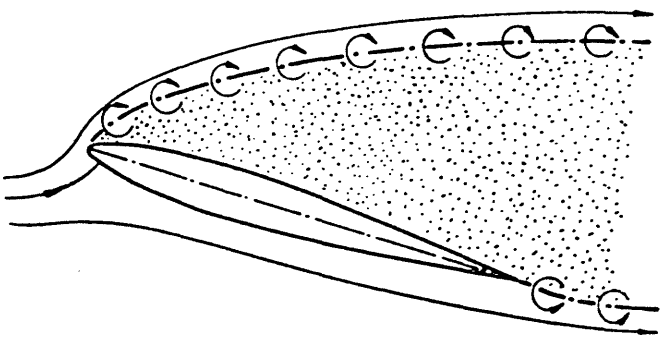

Figure C.2.3 - Completely stalled flow with dead-air region

(FROM KÜCHEMANN, 1953)

separation point and instead attaches much further downstream. This type of bubble involves a considerable re-arrangement of the vorticity on the foil, with an associated large change in the pressure distribution on the foil. Typically, the pressure inside the bubble is fairly constant except near the trailing edge of the bubble. Fig. C.2.3 shows the situation which occurs when the flow fails to reattach to the foil at all after laminar separation. A large dead-air region exists over the upper surface of the airfoil, with the pressure inside only slightly below the free stream value.

The pressure distribution on the surface of an airfoil with a short bubble is shown in Fig. C.2.4a. The laminar boundary layer separates at point S in the adverse pressure gradient following the suction peak. The separated shear layer encloses a region of quiescent fluid until point T is reached, where the shear layer undergoes transition to turbulence. Aft of this point, turbulent mixing between the free stream and the shear layer enables the pressure rise to point R to be negotiated, whereupon the flow reattaches to the foil surface as a turbulent boundary layer. As shown in Fig. C.2.4b a short bubble typically affects the pressure on the foil surface only in the immediate vicinity of the bubble. For this reason the presence of short bubbles usually does not influence the lift, drag, or pitching moment.

A long bubble may extend over a large fraction of the airfoil chord and drastically alter the pressure distribution. Typically the suction peak (and thus the leading edge suction force) is greatly

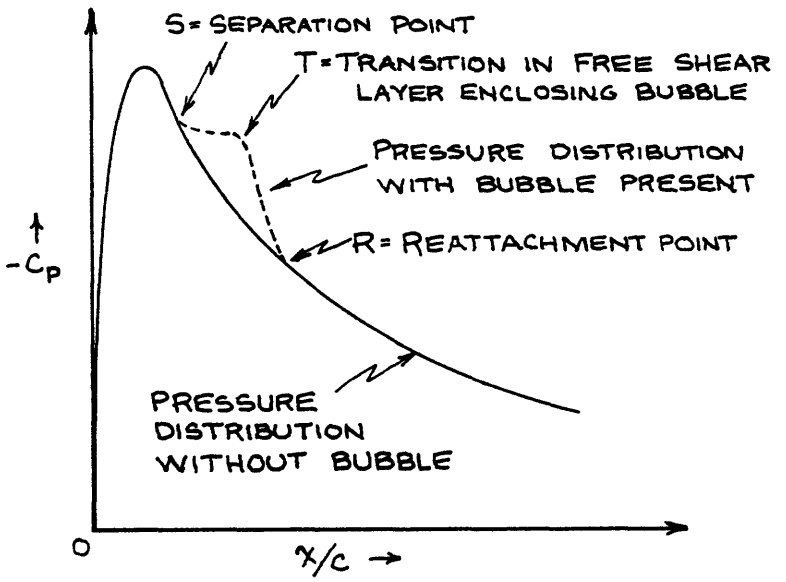

FIG. C.2.4a SCHEMATIC OF UPPER SURFACE PRESSURE DISTRIBUTION ON FOIL WITH SHORT BUBBLE

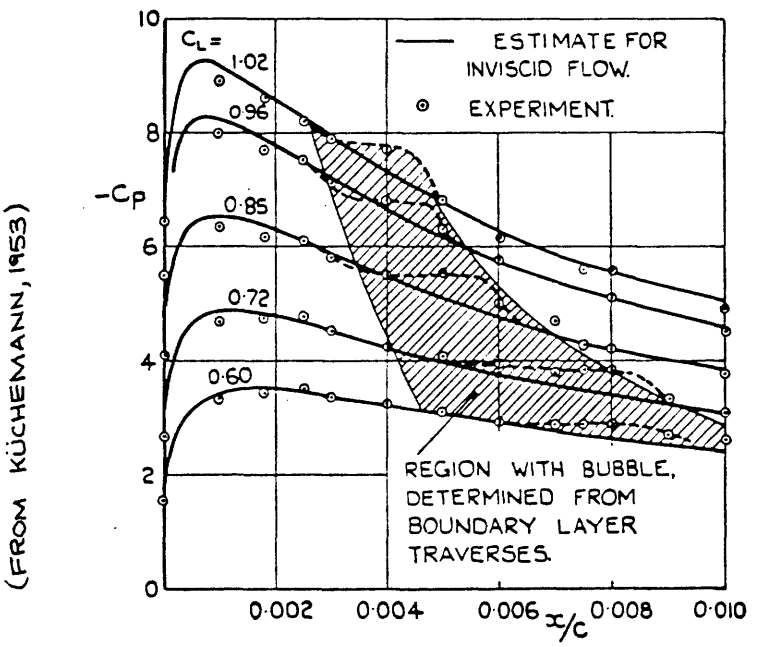

FIG. C.2.4b PRESSURE DISTRIBUTION NEAR NOSE OF NACA 63-009 SECTION

Figure C.2.4 - Pressure distribution on foil with short separation bubble

reduced, so that the drag is increased. However, the low pressure in the bubble is extended over a large part of the chord, so that the lift does not necessarily suffer (Fig. C.2.5). This is responsible for the gentle stall of thin airfoils, where a long bubble grows in length as the incidence is increased (Fig. C.1.1c).

C.3 Separation Bubble Behavior and Stall

Most two dimensional airfoil sections will have a short laminar separation bubble present near the nose when operating slightly above ideal angle of attack. The length of this bubble decreases as the Reynolds number is increases at a fixed incidence, since the free shear layer undergoes transition sooner.

As the incidence is increased at a fixed Reynolds number both the separation point S and the reattachment point R (Fig. C.2.4) move forward, and the bubble contracts in length. At some point the short bubble "bursts", due either to the bubble being unable to negotiate the required pressure rise in so short a distance, or because the "reattached" turbulent boundary layer undergoes turbulent separation immediately downstream of R.

At this point there are two possibilities. If the shear layer fails to reattach to the foil at any point the flow breaks down completely and leading edge stall is said to have occurred, with a loss of lift and a large increase in drag (Figs. C.1.1b, C.2.3). If the shear layer reattaches much further downstream a long bubble forms (Fig. C.2.2)

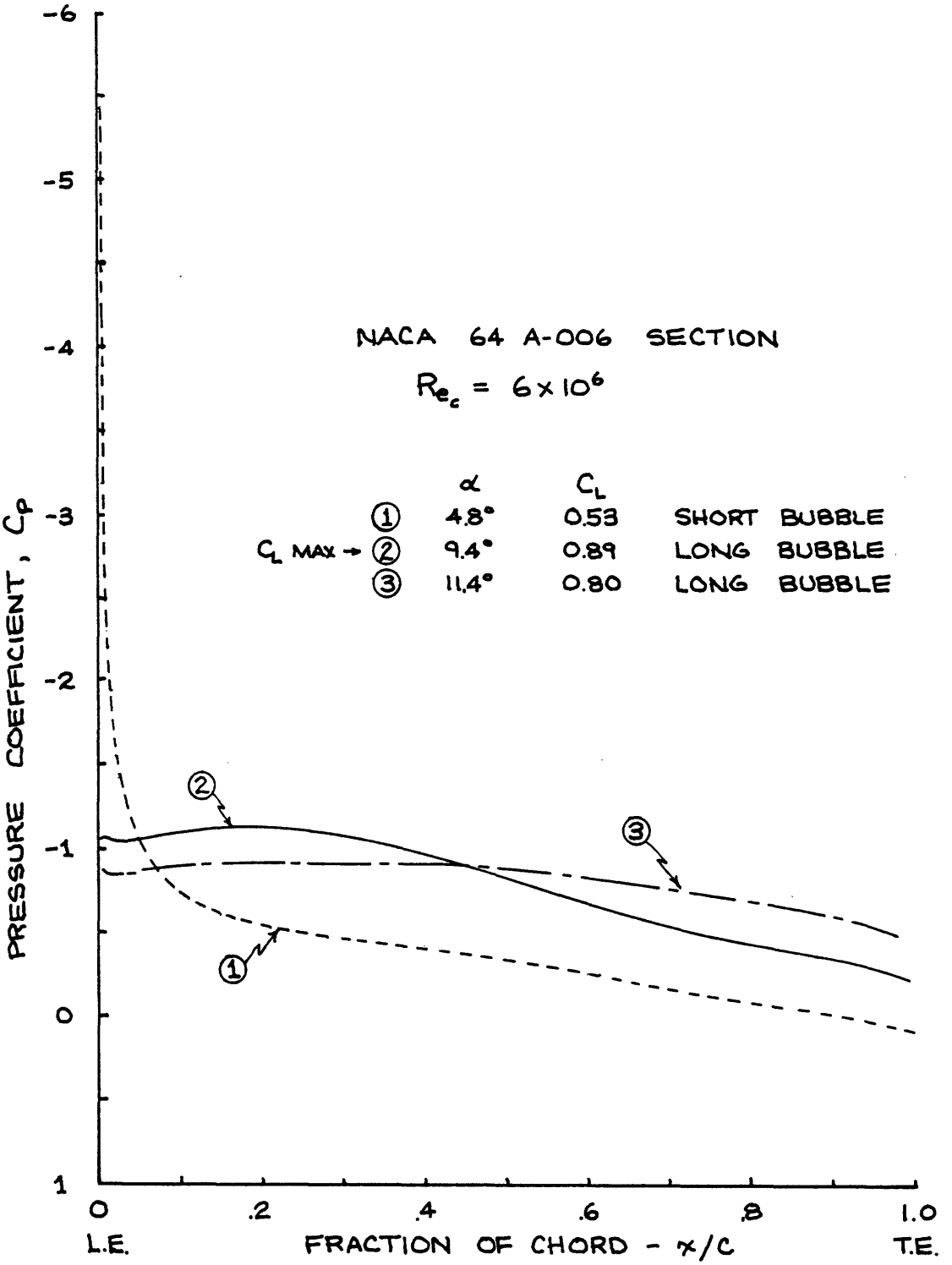

(From Küchemann, 1953)

Figure C.2.5 - Upper surface pressure distribution on foil with long separation bubble

and alters the pressure distribution over the airfoil upper surface. This jump between short and long bubbles is the start of thin-airfoil stall, and is responsible for the kink in the C_L vs. α curve for thin airfoils (Fig. C.1.1c). As incidence is increased further the reattachment point of the long bubble moves aft and the slope of the C_L vs. α curve falls off slowly.

C.4 Environmental Effects on Two-Dimensional Separation Bubbles

The critical issue in two dimensional laminar separation bubbles is how quickly the free shear layer undergoes transition to turbulence. Thus Reynolds number, free stream turbulence, and surface roughness all influence separation bubble behavior. It is beyond the current state of the art to account for these factors in a rational fashion, so recourse is made to experimental data. The most important quantity to determine is the operating condition at which the bursting of a short bubble takes place. Gaster (1966) reasoned that for low inflow turbulence flow over smooth two dimensional foils, bursting should depend on the following quantities:

- u_s - the velocity at the separation point S (surface velocity in attached, inviscid flow)
- θ_s - the momentum thickness of the laminar boundary layer at S
- ν - the kinematic viscosity
- $\Delta u/\Delta x$ - the change in surface velocity Δu over the length of the bubble Δx

Gaster formed a Reynolds number

$$R_{\theta_s} = \frac{u_s \theta_s}{\nu} \qquad (C.4.1)$$

and a pressure gradient parameter

$$P = \frac{\theta_s^2}{\nu} \frac{\Delta u}{\Delta x} \qquad (C.4.2)$$

and achieved an excellent correlation between R_{θ_s} and P at bursting, shown in Fig. C.4.1. For short bubbles, $\Delta u/\Delta x$ over the length of the bubble is very close to du/dx at the separation point. If we momentarily consider P to be given by $P = (\theta_s^2/\nu)\ (dU/dx)$, then Stratford's (1957a) laminar separation theory, as modified by Curle and Skan (1957), shows that laminar separation will not take place near the leading edge for $P > -.09$, as shown in Fig. C.4.1. Also, for $R_{\theta_s} < 125$, the free shear layer will usually not undergo transition to turbulence soon enough to form a short bubble.

Fig. C.4.1 presents measured values of P and R_{θ_s} for short bubbles on the verge of bursting. This same type of figure forms the basis of bubble behavior prediction schemes (Herring and Ely (1978), Pavelka and Tatum (1981), where experimental data for bubble breakdown is plotted as a computed pressure gradient parameter at separation versus some relevant computed Reynolds number. Although these prediction schemes seem to work fairly well, no account is taken of surface roughness or inflow turbulence, which are sure to have a significant impact.

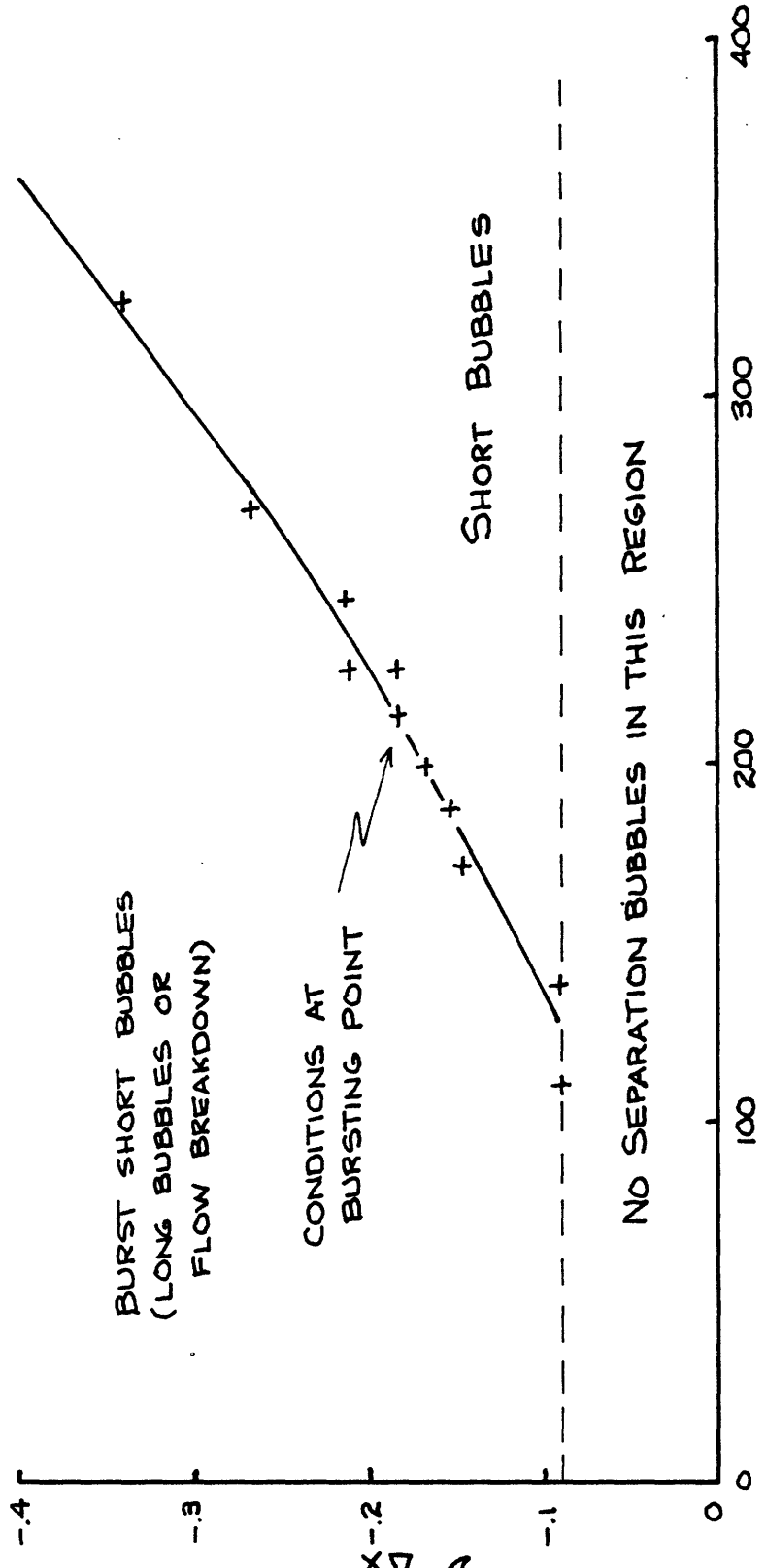

Figure C.4.1 - Relationship between R_{θ_s} and P at bubble burst

Appendix D: Three Dimensional Flow Separation and Attachment

Flow separation in steady two-dimensional flow is relatively easy to define: it is where the skin friction vanishes and the flow breaks away from the surface. Separation in three-dimensional flow is far more complicated. Many three dimensional flow separations occur where the skin friction is non-zero and the external streamlines are not significantly affected.

Maskell (1955) clarified the matter considerably by considering the behavior of the limiting streamlines on the surface of a body or wing. Of course there is no flow at the surface of a body moving in a viscous fluid, but there is at a distance ε above the body. The limiting streamlines are determined by letting $\varepsilon \to 0$.

Ordinary separation and attachment occurs along a line on a smooth body where the limiting streamlines gradually merge, as shown in Fig. D.1. Limiting streamlines may also collide head on at singular separation and attachment points S, shown in Fig. D.2.

These types of limiting streamline behavior are usually associated with distinct forms of separation. The surface of separation above an ordinary separation line is actually a shear layer or vortex sheet, shown in Fig. D.3. This is the most common type of three dimensional separation. Singular separation and attachment occurs only at isolated points and is usually associated with the presence of a bubble of trapped fluid, as shown in Fig. D.4. Singular attachment points also occur at the forward stagnation points of bodies of revolution at zero angle of attack.

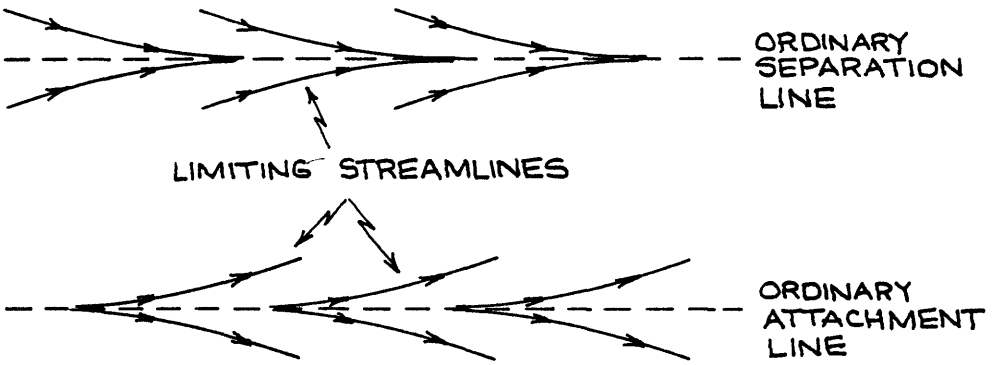

Figure D.1 - Limiting Streamlines for ordinary separation and reattachment

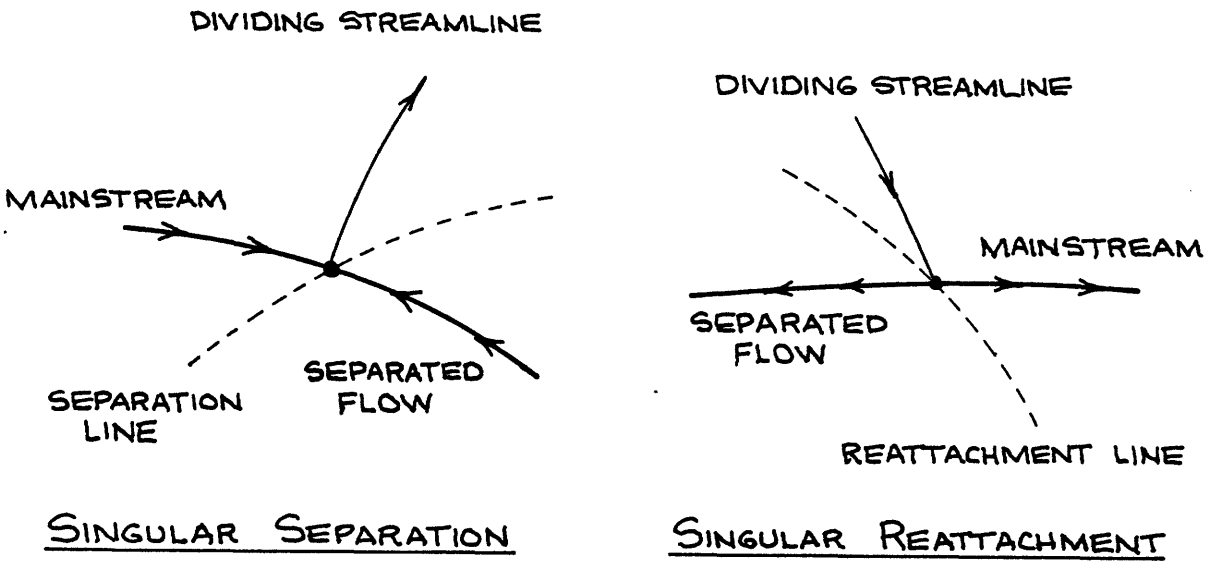

Figure D.2 - Limiting Streamlines for singular separation and reattachment

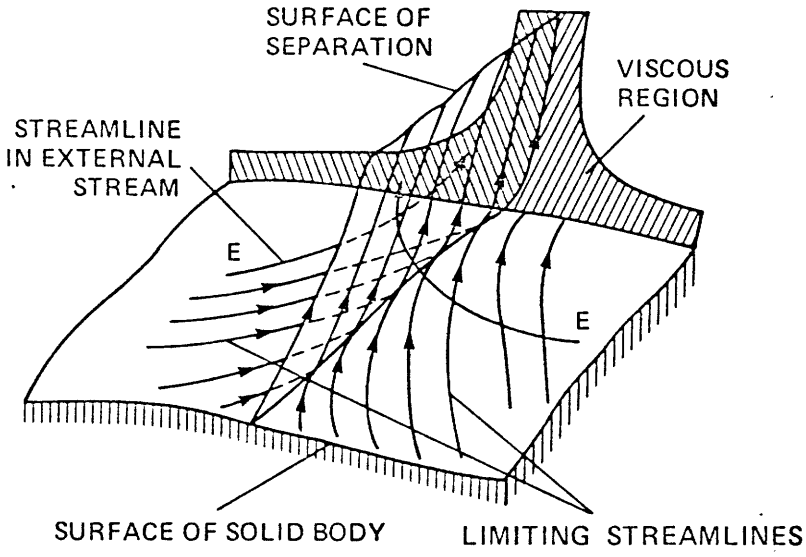

Figure D.3 - Vortex separation

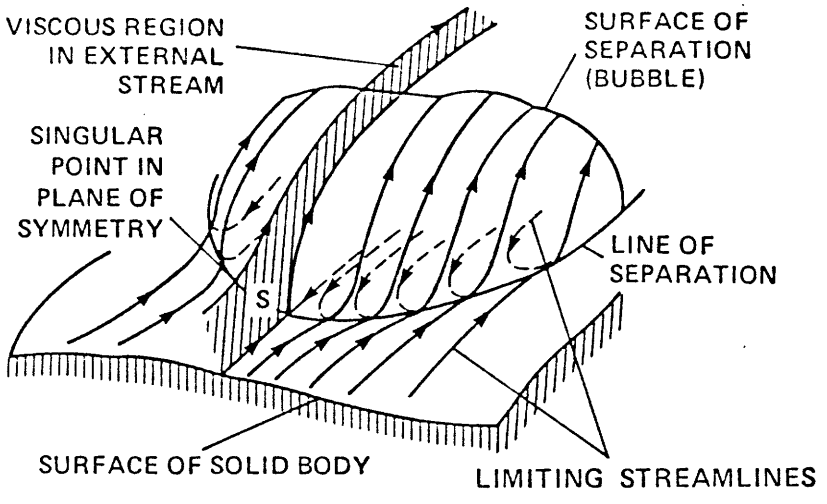

(FROM TOBAK & PEAKE, 1979)

Figure D.4 - Bubble separation

In the steady viscous flow past a solid body the paths of the individual fluid particles are of two distinct types. Open streamlines begin at infinity upstream and end at infinity downstream. Particles following closed streamlines circulate continuously along closed paths, which are necessarily associated with separation bubbles.

Separation bubbles on two dimensional airfoil sections are truly bubbles according to the above definition, since they contain fluid particles which circulate slowly along closed streamlines (ignoring the turbulence at the end of the bubble). However, a separation "bubble" at the leading edge of a swept wing is not really a bubble, since the spanwise flow along the leading edge prevents closed streamlines from forming and the separation and reattachment will be of the ordinary type. Nevertheless, it is called a bubble because of its similarity to a two dimensional bubble.

A thorough discussion of three dimensional separation and reattachment may be found in Maskell (1955), Lighthill (1963), and Tobak and Peake (1979).

Appendix E: Flow Around Infinite Sheared Wings

An infinite sheared wing is a swept wing of infinite aspect ratio, obtained by shearing backward every section of an unswept wing, leaving its shape and lateral position of each section unchanged.

For the position of a sheared wing shown in Fig. E.1, introduce a coordinate system (ξ, η, ζ) defined by

$$\xi = x\cos\Lambda - y\sin\Lambda$$

$$\eta = x\sin\Lambda + y\cos\Lambda$$

$$\zeta = z \qquad \text{(E.1)}$$

where Λ = leading edge sweep angle.

Two different airfoil sections can be considered when discussing sheared wings. The streamwise section (suffix s) is the original section from which the sheared wing was formed. We may also consider the airfoil section in a plane normal to the η axis (suffix n), as shown in Fig. E.1. From simple geometry we have

$$c_n = c_s\cos\Lambda$$

$$(t_o)_n = (t_o)_s$$

$$\left(\frac{t_o}{c}\right)_n = \left(\frac{t_o}{c}\right)/\cos\Lambda$$

$$r_n = r_s/\cos\Lambda \qquad \text{(E.2)}$$

where

c = chord length

t_o = maximum thickness

r = leading edge radius

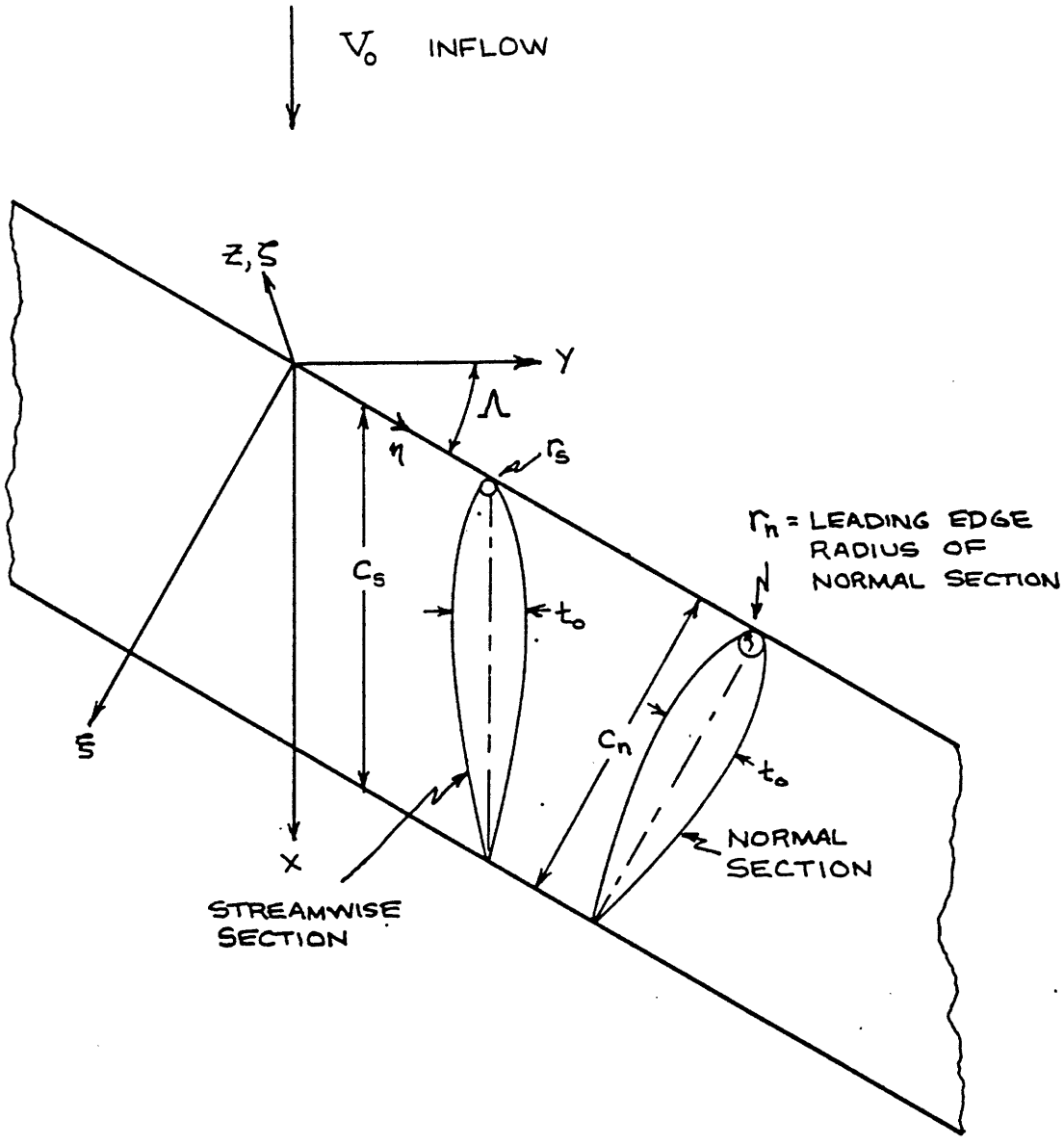

Figure E.1 - Portion of an infinite sheared wing

The flow over the sheared wing is equivalent to the two-dimensional flow around the normal section, with inflow components

$$V_{\xi_0} = V_0 \cos \Lambda \cos \alpha$$

$$V_{\zeta_0} = V_0 \sin \alpha \qquad \text{(E.3)}$$

where α is measured in a vertical streamwise plane, plus the spanwise flow component

$$V_{\eta_0} = V_0 \sin \Lambda \cos \alpha \qquad \text{(E.4)}$$

which leads to a non-zero velocity along the attachment line of the sheared wing (where the normal section has its stagnation point). This stagnation line flow can have a significant influence on the behavior of sheared wings, as described in Chapter IV.

Perturbation velocities due to thickness and lift are generated only in the ξ and ζ directions: there are no perturbation velocities in the η direction. Because the potential flow around a sheared wing is independent of the velocity in the η direction, the flow follows what is know as the 'independence principle'. The perturbation velocities u_ξ and u_ζ are those due to the two dimensional flow around the normal section, with the inflow velocities to the section given by (Eq. E.3). Since the streamwise inflow velocity V_{ξ_0} is reduced from the streamwise inflow V_0 by the factor cos Λ, the perturbation velocities due to lift (in linear theory) will be reduced by the same factor. The same conclusion can be reached by looking at the vorticity distribution when the wing is at an angle of attack. The normal inflow velocity $V_{\zeta_0} = V_0 \sin \alpha$ is

independent of sweep, so the strength of the bound vortices parallel to the leading edge, $\gamma(\xi)$, is also independent of sweep. The vortices are inclined at an angle $\frac{\pi}{2} - \Lambda$ to the mainstream V_0, so the pressure jump across the wing is

$$\Delta p(\xi) = \rho V_o \gamma(\xi) \cos\Lambda \qquad (E.5)$$

from the Kutta-Joukowski law. Thus the lift slope of the sheared wing is

$$\frac{dC_l}{d\alpha} = 2\pi \cos\Lambda \qquad (E.6)$$

The thickness to-chord ratio of the normal section is greater than that of the streamwise section, as given by (Eq. E.2), and the leading edge radius is also increased. This means that the high velocities near the leading edge caused by angle of attack loading are reduced by the presence of leading edge sweep. Brown and Norton (1976) made use of this fact in designing a novel thruster blade having increased tolerance to angle of attack fluctuations without causing leading edge cavitation.

If we consider the laminar boundary layer on an infinite sheared wing, we arrive at the conclusion that the flow in the ξ, ζ plane around the normal section is independent of the spanwise flow in the η direction (see, for example, Schlicting (1968)). Hence the independence principle also holds for laminar boundary layers. However, once the flow separates or becomes turbulent the independence principle no longer applies: the flow must be considered as being completely three dimensional, even though the potential flow is independent of the η direction.

Appendix F: Parabolic Leading Edges

Thin airfoil theory, such as that described in Appendix A, leads to solutions having infinite velocities at the leading edge when the section or wing is operating above its design angle of attack. In practice, infinite velocities do not occur because the leading edge has a finite radius of curvature. Lighthill (1951) and Van Dyke (1955) formulated leading edge corrections to thin airfoil theory so that surface velocites may be accurately calculated near the nose of a foil. However, these corrections are formulated in terms of angle of attack of the section, which is a somewhat nebulous concept for a propeller blade section. The derivation below expresses the leading edge flow in terms of the leading edge suction force (see Appendix A). Only two dimensional flows are considered here, since the flow near a swept leading edge can be approximately decomposed into the flow normal to the leading edge and a flow along the leading edge, as shown in Appendix E.

The surface velocity distribution for a zero thickness flat plate at small incidence α is

$$\frac{V}{V_\infty} = 1 \pm \alpha\sqrt{\frac{c-x}{x}}$$

$$= 1 \pm \frac{1}{\sqrt{x/c}} \cdot \alpha\sqrt{1-x/c} \qquad \text{(F.1)}$$

where x = distance from leading edge

c = chord length

V = surface velocity

V_∞ = free stream velocity

The velocity is infinite at the leading edge, as expected. The position of the stagnation point, x_{st}, is where V/V_∞ is zero, and can be found from Eq. F.1:

$$\alpha^2 = \frac{x_{st}/c}{1 - x_{st}/c} \quad , \tag{F.2}$$

$$x_{st} = c\,\alpha^2 \quad \text{for} \quad x_{st}/c \ll 1.$$

The surface velocity may be expanded in a series

$$\frac{V}{V_\infty} = 1 \pm \frac{\alpha}{\sqrt{x/c}} \left[1 - \frac{1}{2}\,\frac{x}{c} + \ldots\right]$$

$$\cong 1 \pm \frac{\alpha}{\sqrt{x/c}} \qquad \text{for } \frac{x}{c} \ll 1 \tag{F.3}$$

Inserting Eq. F.2 we get

$$\frac{V}{V_\infty} \cong 1 \pm \sqrt{\frac{x_{st}}{x}} \quad , \quad \begin{matrix} x_{st} \ll c \\ x \ll c \end{matrix} \tag{F.4}$$

The leading edge suction force F_s for a flat two-dimensional foil is given by the zero drag condition (see Appendix A):

$$F_s = 2\pi\,\alpha \cdot (\tfrac{1}{2}\,\rho\,V_\infty^2\,c)\alpha$$

$$= 2\pi\,\alpha^2 c\,(\tfrac{1}{2}\,\rho\,V_\infty^2) \tag{F.5}$$

Inserting Eq. (F.2) we obtain

$$F_s = 2\pi\,x_{st}\,(\tfrac{1}{2}\,\rho\,V_\infty^2) \quad , \quad x_{st} \ll c \tag{F.6}$$

which now specifies the stagnation point x_{st} in terms of the suction force F_s.

The leading edge corrections by Lighthill and Van Dyke involve multiplying the thin airfoil surface velocities by the factor $[x/(x+r/2]^{1/2}$, where r is the leading edge radius. Applying this to Eq. F.4, we get

$$\frac{V}{V_\infty} = \left(1 \pm \sqrt{\frac{x_{st}}{x}}\right)\left(\frac{x}{x+\frac{r}{2}}\right)^{1/2}$$

$$= \frac{\sqrt{2x/r} \pm \sqrt{2x_{st}/r}}{\sqrt{1 + 2x/r}} \qquad \text{(F.7)}$$

This is exactly equivalent to considering the flow around an infinite parabola, as shown in Fig. F.1.

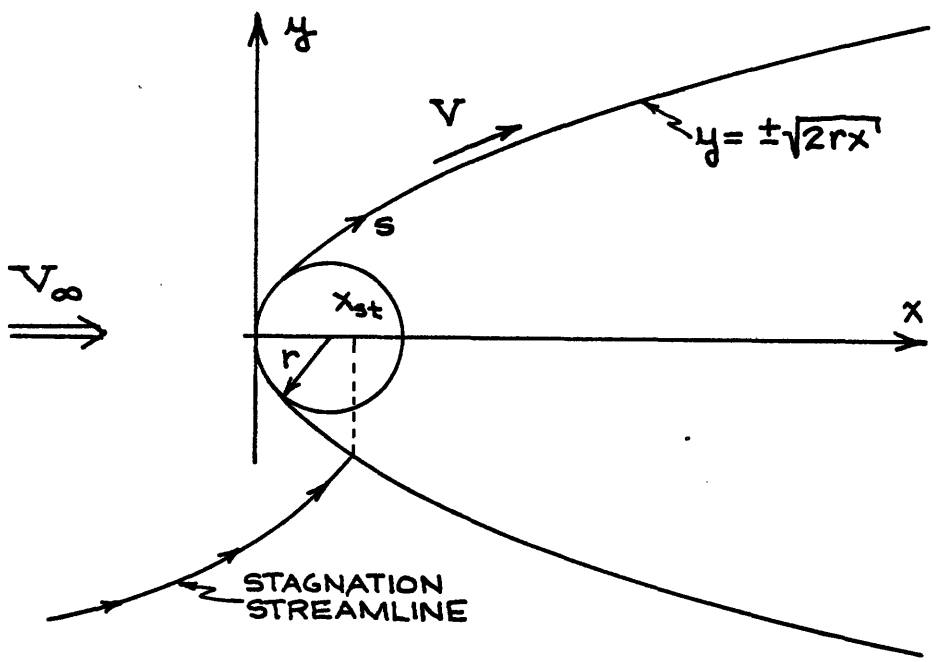

Figure F.1 - Parabolic leading edge

In order to perform boundary layer computations, the surface velocity V as a function of arc length s must be known. To do this it is convenient to non-dimensionalize all lengths by the leading edge radius r, and introduce the parameter t. Then we have

$$\frac{x}{r} = t^2$$

$$\frac{y}{r} = \sqrt{2}\, t \qquad \text{(F.8)}$$

To find the arc length s along the surface we note that $ds^2 = dx^2 + dy^2$, which leads to

$$\frac{s(t)}{r} = 2 \int_0^t \sqrt{\tau^2 + 1/2}\; d\tau$$

$$= t\sqrt{t^2 + 1/2} + \frac{1}{2} \ln\left[\frac{t + \sqrt{t^2 + 1/2}}{\sqrt{2}/2}\right] \qquad \text{(F.9)}$$

The velocity on the surface can be found by expressing Eq. F.7 in terms of t and t_{st}, where t_{st} is given by

$$t_{st} = -\sqrt{\frac{x_{st}}{r}} \qquad \text{(F.10)}$$

and the minus sign causes the stagnation point to be on the lower surface. Eq. (F.6) can be re-written as

$$\frac{x_{st}}{r} = \frac{1}{2\pi} \frac{F_s}{\frac{1}{2}\rho r V_\infty^2} \qquad \text{(F.11)}$$

The second term is precisely the leading edge suction force coefficient defined in Eq. 4.3.1

$$C_s = \frac{F_s}{\frac{1}{2} \rho \, r_n \, U_n^2} \qquad (4.3.1)$$

which is applied to both 2^D and 3^D wings. Thus

$$\frac{x_{st}}{r} = \frac{C_s}{2\pi} \qquad (F.12)$$

Velocity gradients on the surface can be obtained by straightforward application of the chain rule.

Appendix G: Calculation of Lateral Vorticity Movement in Leading Edge Vortex Sheet

G.1 Single Node Calculation

Section 5.1 notes that the proper boundary condition for a free vortex sheet in steady inviscid flow is that there is no pressure jump across it. This condition is satisfied if the local vorticity vector in the vortex sheet is parallel to the local velocity vector at all points on the free sheet. In most vortex lattice techniques this condition is approximately satisfied by making each discrete vortex segment parallel to the velocity vector at its upstream end or mid-point.

In the current work the vortex sheet is rendered approximately force free by determining how the vorticity entering each node in the discretized sheet leaves the node; that is, how much leaves in the downstream chordwise vortex and how much leaves in the spanwise vortex in the direction of the spanwise velocity at that node. This process is best illustrated by showing the computations done at a typical node in the discretized free vortex sheet.

Figure G.1.1 shows a typical node in the discretized free sheet. The relevant quantities are defined as follows:

V_c - chordwise velocity at node

V_s - spanwise velocity at node

Γ_c - strength of chordwise vortex

Γ_s - strength of spanwise vortex

The (m, n)'th node is under consideration. V_c and V_s have been cal-

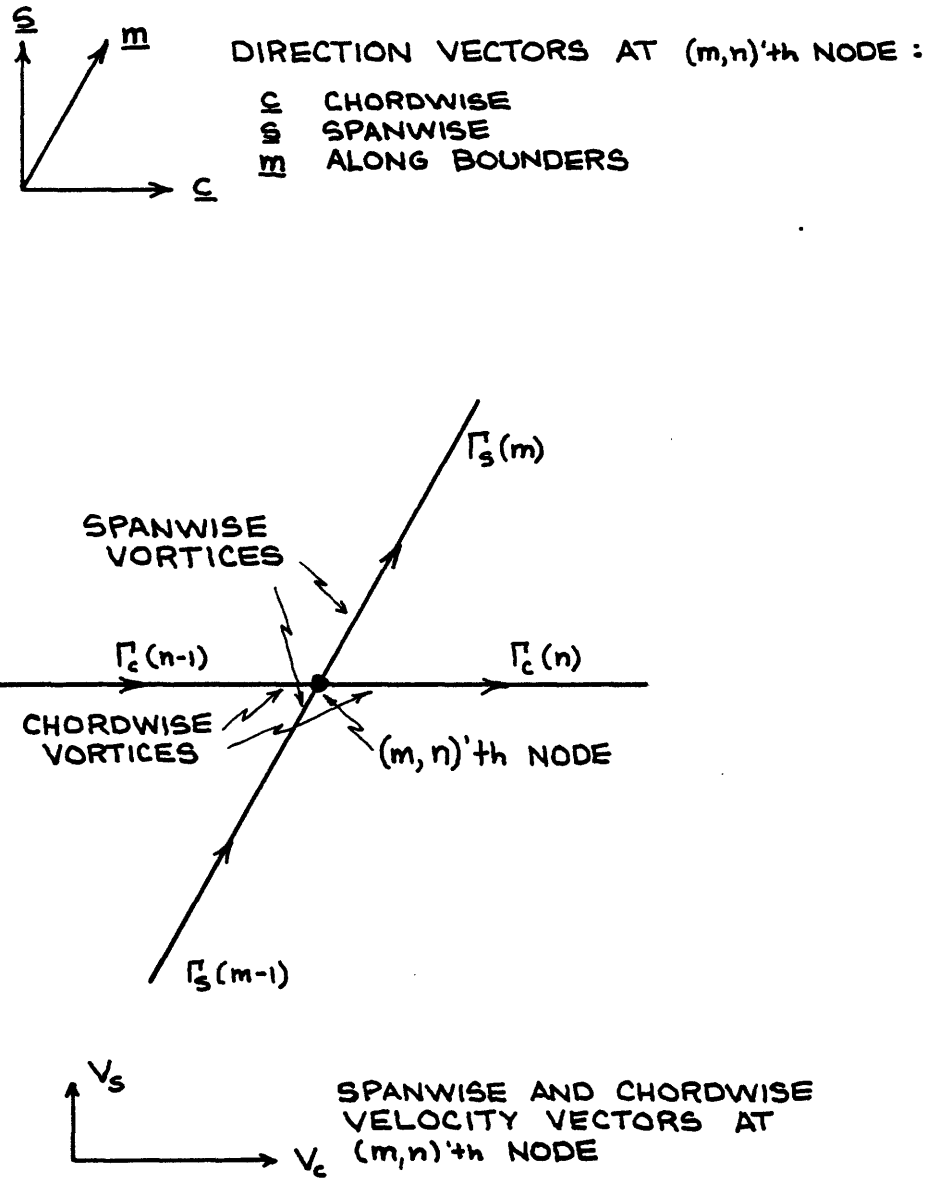

Figure G.1.1 - Typical node in discretized free vortex sheet

culated previously, and $\Gamma_c(n-1)$ and $\Gamma_s(m-1)$ are known from prior nodal calculations. The problem is to determine $\Gamma_c(n)$ and $\Gamma_s(m)$. Note that the "spanwise" vortices actually have components in both the spanwise and chordwise directions. The spanwise vortices point in the "m" direction, which varies over the blade.

The total vorticity entering the node is

$$\Gamma_t = \Gamma_c(n-1) + \Gamma_s(m-1) \tag{G.1.1}$$

By Kelvin's theorem, this must also be the total vorticity leaving the node

$$\Gamma_t = \Gamma_c(n) + \Gamma_s(m) \tag{G.1.2}$$

The total chordwise vorticity vector at the node is

$$\Gamma_{ct} = \left(\Gamma_c(n-1) + \Gamma_c(n)\right) + (\underline{c} \cdot \underline{m}) \left(\Gamma_s(m-1) + \Gamma_s(m)\right) \tag{G.1.3}$$

and the total spanwise vorticity vector at the node is

$$\Gamma_{st} = \left(\Gamma_s(m-1) + \Gamma_s(m)\right)(\underline{s} \cdot \underline{m}) \tag{G.1.4}$$

The local vorticity vector is parallel to the local velocity vector if the following equation is satisfied

$$\frac{\Gamma_{st}}{\Gamma_{ct}} = \frac{V_s}{V_c} = Q \tag{G.1.5}$$

By simple algebra,

$$\Gamma_s(m) = \frac{Q\left[\Gamma_c(n-1) + \Gamma_t + (\underline{c} \cdot \underline{m})\,\Gamma_s(m-1)\right] - (\underline{s} \cdot \underline{m})\,\Gamma_s(m-1)}{(\underline{s} \cdot \underline{m}) + Q\,(1 - (\underline{c} \cdot \underline{m}))} \qquad \text{(G.1.6)}$$

and

$$\Gamma_c(n) = \Gamma_t - \Gamma_s(m) \qquad \text{(G.1.7)}$$

However, this calculation must be constrained somewhat. If we take the arrows on the vortex segments in Fig. G.1.1 to point in the direction of positive vorticity (using the right-hand rule), then we expect on physical grounds that $\Gamma_c \geq 0$ at every node. That is, the sense of rotation of the shed vorticity should not change sign in the middle of the sheet. Thus at each node we must insure that

$$\Gamma_c(n) \geq 0 \qquad \text{(G.1.8)}$$

G.2 Node Marching Procedure

Since there is an inequality constraint to be satisfied at each node, a set of simultaneous equations cannot be generated to solve all of the node calculations at once. There appear to be two alternative solution procedures:

a) March through the nodes one by one, satisfying the constraint at each node in turn; or

b) Formulate an optimization problem with inequality constraints to do all of the node calculations at once.

Since the former approach appears to be far simpler it has been chosen here. The remaining problem is to determine the marching direction.

From physical arguments we expect that marching through the nodes should progress basically in the chordwise (downstream) direction. However, since the spanwise vortices and chordwise vortices are not orthogonal, ambiguities arise in determining which nodes to do first if the marching is in the chordwise direction. The resolution to this problem is to march through the nodes in order of increasing θ (see Fig. 3.1.1, pg. 28). This eliminates all arbitrariness in determining marching order.

All of the node calculations are done using the values of the leading edge horseshoe strengths from the most recent iteration. The leading edge horseshoe strengths determine the amount of vorticity entering the free sheet at the n=1 row of nodes, and all of the node calculations described in Section G.1 depend on the actual values of the vorticity being directed through the discretized free sheet. Once the node calculations are completed using the actual vorticity values, the ratio $\Gamma_c(n)/\Gamma_t$ (see Eq. G.1.1 - G.1.7) is computed at each node and saved for use in assigning leading edge horseshoe element weights, as described below.

G.3 Determination of Leading Edge Horseshoe Element Weights

As discussed in Section 5.3 and illustrated in Fig. 5.3.2, the free sheet portion of a leading edge horseshoe vortex actually consists of quite a few spanwise and chordwise vortex elements in the free sheet, with appropriate weighting factors. These weights are

determined by considering vorticity of unit amplitude entering the leading edge of the free sheet at the proper location for the leading edge horseshoe under consideration. All of the nodes in the free sheet are then marched through in precisely the same order as that determined during the lateral vorticity movement described in Sections G.1 and G.2 above. At each node the value of $\Gamma_c(n)/\Gamma_t$ computed previously is used to establish the strengths of the spanwise and chordwise vortex segments adjacent to that node. Since the node marching procedure does in fact satisfy Kelvin's theorem everywhere on the free sheet, and since a unit amplitude of vorticity entered the free sheet at the leading edge, the strengths of the spanwise and chordwise vortex segments determined by this procedure are precisely the weighting factors for the leading edge horseshoe under consideration. This procedure is repeated for each of the leading edge horseshoe vortices.